PHOTOPHYSICOCHEMICAL STUDIES AND PHOTODYNAMIC THERAPY ACTIVITY OF INDIUM AND GALLIUM PHTHALOCYANINES

A thesis submitted in fulfilment of the requirements for the degree of

MASTER OF SCIENCE

Of

RHODES UNIVERSITY

By

CHARMAINE SESETHU TSHANGANA

January 2015

Acknowledgments

“A great teacher is one who shows you where to look, but not what to see”

The knowledge gained and ultimately the completion of this program would not have been possible without the help of my supervisor; **Distinguished Professor Tebello Nyokong**. Her time, enthusiasm, guidance, patience and interest in the topic served as great motivation. Thank you for teaching me to work and think independently while also allowing me to find myself in the process. The amount of grooming that I have received from you in the last two years cannot be quantified.

Thank you Prof. for allowing me to do part of my research at Charité University- Berlin, Germany. I would also like to thank **Dr EugenyErmilov and Dr Micheal Höpfner** for their supervision as host supervisors at Charité University- Berlin, Germany- appreciation to their research group as well for the support while I was there.

Also grateful for having had another opportunity to visit University of East Anglia- Norwich, United Kingdom, my gratitude goes to **Prof. Andy Cambridge** and **Dr Stephen Ashworth** my host supervisors- many thanks to their research group for the support while I was there.

I would like to thank **Dr OluwasesanAdegoke** who guided me through the initial and pivotal part of this project. My gratitude also goes to **Ms Gail Cobus**, for organizing and arranging all my trips and her kind assistance throughout the years. To my family; my mother and sisters thank you for the LOVE and support.

Thank you to everyone in **S22 research group** for making the last few years very pleasant, you guys made the lab feel like home away from home, I will forever carry you guys in my heart.

Thanks to the Department of Science and Technology (DST) and National Research Foundation (NRF) South Africa through DST/NRF South African Research Chairs Initiative for Professor of Medicinal Chemistry and Nanotechnology and Rhodes University for the financial support. I would also like to thank the Pearson Young Memorial Trust Foundation (United Kingdom).

Finally I would like to thank Rhodes University, Chemistry department as a whole and the technical staff for their help throughout this program.

Abstract

The potential toxicity of seven different types of quantum dots without shell (L-cysteine-CdTe, TGA-CdTe, MPA-CdTe, TGA-CdSe) and with the shell (GSH-CdSe@ZnS, GSH-CdTe@ZnS,) with different capping agents were evaluated. The growth inhibitory effects of the various quantum dots on human pancreatic BON cancerous cells were determined. The least cytotoxic of the various quantum dots synthesized and the one displaying the lowest growth inhibitory potential and no embryotoxicity was determined to be the GSH-CdSe@ZnS quantum dots. The GSH-CdSe@ZnS quantum dots were then conjugated to gallium, aluminium and indium octacarboxy phthalocyanine and the photophysical behaviour of the conjugates studied for potential use in photodynamic therapy and imaging applications. The sizes, morphology, thermal stability and confirmation of successful conjugation was determined using X-ray diffraction (XRD), transmission electron microscopy (TEM), thermogravimetric analysis (TGA) and Fourier transform infrared spectroscopy (FTIR), respectively. The study was extended by conjugating amino functionalized magnetic nanoparticles (Fe_3O_4) to indium octacarboxy phthalocyanine to study the photophysical behaviour of the conjugate as a potential bi-functional anti-cancer agent (hyperthermia and photodynamic therapy applications). A three-in-one multifunctional nanocomposite comprising of the quantum dots, magnetic nanoparticles and indium octacarboxy phthalocyanine was developed with the aim of developing a multifunctional composite that is able detect, monitor and treat cancer. All conjugates showed improved and enhanced photophysical behaviour. Finally, GSH-CdSe@ZnS conjugated to aluminium octacarboxy phthalocyanine was applied in human pancreatic carcinoid BON cells. The conjugates induced cell death dose-dependently.

Table of contents

List of abbreviations

a	**Absorption**
A	**Acceptor**
AC	**Alternating current**
ADMA	**Tetrasodium α,α-(anthracene-9,10-diyl) dimethylmalonate**
ADME	**Absorption, Distribution, Metabolism and Excretion**
AE	**Acceptor excitation**
APTES	**3-aminopropyltriethoxysilane**
ASE	**Acceptor sensitized emission**
CdSe	**Cadmium selenide**
CdTe	**Cadmium telluride**
CT	**Charge transfer**
CTTs	**Charge transfer transitions**
D	**Donor**
DBU	**1,8-diazabicyclo[5.4.0]undec-7-ene**
DDS	**Drug delivery system**
DHLA	**Dihydrolipoic acid**
DOS	**Density of energy states**
e	**Emission**
EBR	**Exciton Bohr radius**
FRET	**Förster resonance energy transfer**
GSH	**$_{L}$-glutathione**
HPT	**Hyperthemia**
IVD	**Intravenously delivered**
MCF-7	**Human breast cells**

MI	**Magneto impedance**
MNPs	**Magnetic nanoparticles**
MPA	**3-mercaptopropionic acid**
MRI	**Magnetic resonance imaging**
MTT	**3-(4, 5 dimethylthiazol-2-yl),2,5 dimethyl tetrazolium bromide**
MUA	**Mercaptoundecanoic acid**
NIR	**Near infrared region**
PEG	**Polyethylene glycol**
PDT	**Photodynamic therapy**
PC12	**Pheochromocytoma cells**
QDs	**Quantum dots**
ROS	**Reactive oxygen species**
SSA	**Sheep serum albumin**
TET	**Triplet energy transfer**
TGA	**Thioglycolic acid**
TOPO	**Trioctylphosphine oxide**
UV	**Ultraviolet**
ZnS	**Zinc sulphide**

List of symbols

α	**Non-peripheral position/linear absorption**
β	**Peripheral position/full width at half maximum**
Δ	**Change**
E	**Molar extinction coefficient**
N	**Refractive index**
T	**Lifetime**
Φ_{Δ}	**Singlet oxygen quantum yield**
Φ_{F}	**Fluorescence quantum yield**
τ_{T}	**Triplet state lifetime**
τ_{F}	**Fluorescence lifetime**
Φ_{T}	**Triplet state quantum yield**
D	**Mean particle size**
T_1	**Triplet excited state**
T	**Transmittance**
F	**Area under fluorescence emission curve**

S_0	**Singlet ground state**
S_1	**Singlet excited state**
T	**Time**
λ_{exc}	**Excitation wavelength of phthalocyanines**
λ_{max}	**Wavelength maximum**
r	**Centre to centre separation distance between donor and acceptor**
R_0	**Critical distance at which efficiency of energy transfer is 50%**
Eff	**Efficiency of energy transfer**
J	**Degree of spectral overlap of donor emission and acceptor absorption spectra**
k^2	**Dipole orientation factor**
$^1O_2$	**Singlet state oxygen**
$^3O_2$	**Triplet molecular state oxygen**

List of Figures

List of Tables

List of Schemes

CHAPTER 1

In this work phthalocyanines are combined with quantum dots and magnetic nanoparticles for possible applications in photodynamic therapy (PDT) or hyperthermia. Quantum dots are discussed first followed by magnetic nanoparticles and phthalocyanines. Finally the possibility of combining all three nanoparticles to form a multifunctional three-in-one nanocomposite to be used to detect, monitor and treat cancer is presented.

1. Introduction

1.1 Basics of Quantum dots

Quantum dots (QDs) are semiconductor nanoparticles that range from 1 to 10 nm in size. The size of the QD is smaller than the Exciton Bohr radius (EBR), thus allowing confinement of the excitons in all three dimensions of space [1-5]. QDs have properties that are intermediate between bulk materials and individual atoms and molecules. As semiconductors, QDs have unique electronic and optical properties [6-11]. They are highly fluorescent with small quantum dots emitting at a higher energy than larger quantum dots **(Figure 1.1)**, this makes the wavelength of light emitted by the particles tunable.

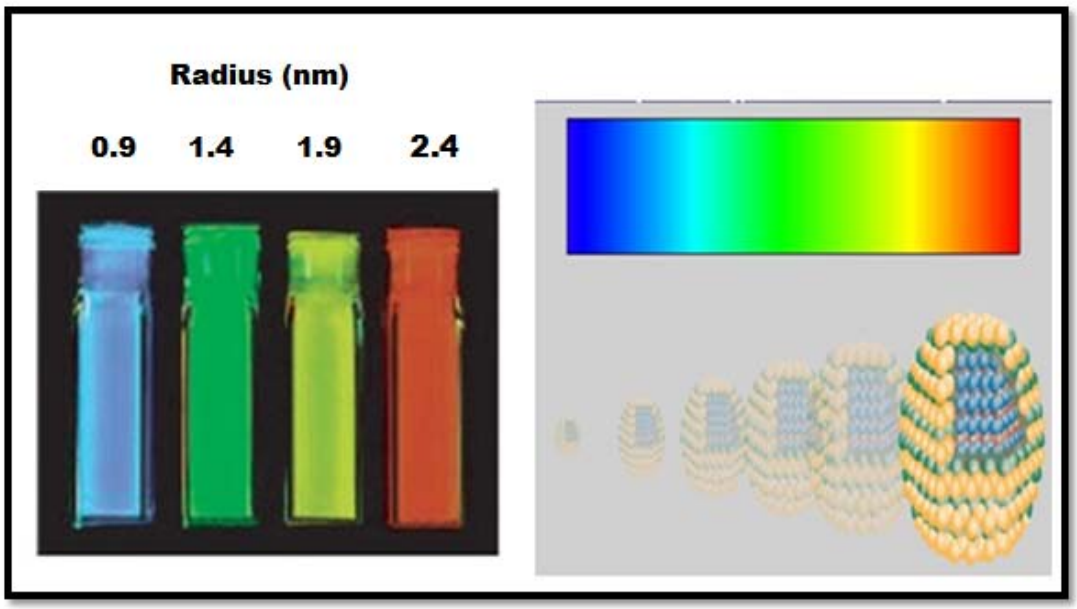

Figure 1.1: Size dependant fluorescence of quantum dots in aqueous solution [12].

This size tunable absorption and emission property of QDs is extremely useful for biological applications; as they can be tuned from the ultraviolet (UV) to the near infrared region (NIR) of the spectrum [13-19]. QDs have a characteristic broad absorption and narrow emission spectra as shown in **Figure 1.2**.

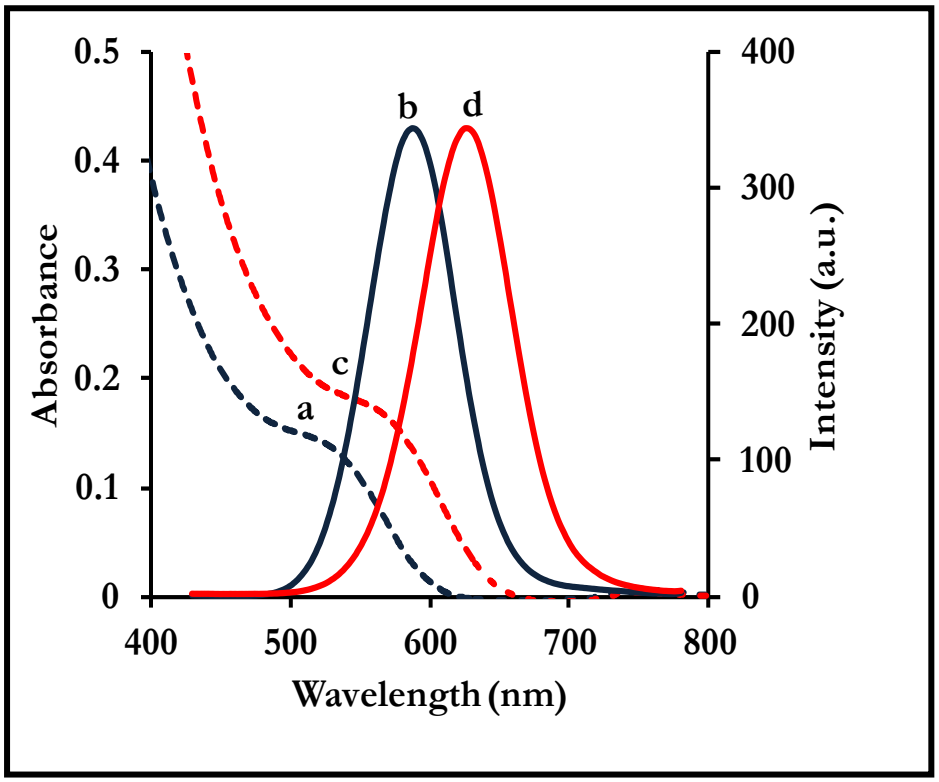

Figure 1.2: Typical absorbance (a and c) and fluorescence emission (b and d) spectra of different sized QDs. Spectra c and d are the larger QDs (unpublished work).

1.1.1 Structure of QDs

QDs are formed from atoms in groups II-VI or III-V of the periodic table. They are made up of a metalloid crystalline core, which, depending on its composition and size, will determine the fluorescence properties [20]. A bare crystalline core is highly reactive and toxic resulting in it being very unstable and also prone to photochemical degradation. The core crystalline structure also has surface defects/irregularities which will result in emission irregularities such as blinking [21]. The core is composed of materials such as cadmium-sellenide (CdSe) and cadmium-telluride (CdTe) **(Figure 1.3)**. Semiconductor shells or coatings are not only introduced to stabilize the core, but to further improve optical, physical properties and bioavailability of the material and also reduce the toxicity of the core by shielding reactive $Cd^{2+}$and Te^{2+} ions from being exposed to photo-oxidative environments. Typically, zinc sulphide (ZnS) is used as a shell [21]. Additional cappings or coatings with biocompatible materials have been introduced to make the QDs soluble in aqueous media and to be non-toxic. Examples of such coatings include; $_{L}$-glutathione (GSH), thioglycolic acid (TGA), 3-mercaptopropionic acid (MPA), polyethylene glycol (PEG) and L-cysteine [22, 23]. The coating ligands on the surface of the QDs will also allow coordination to bio-molecules **(Figure 1. 3)**.

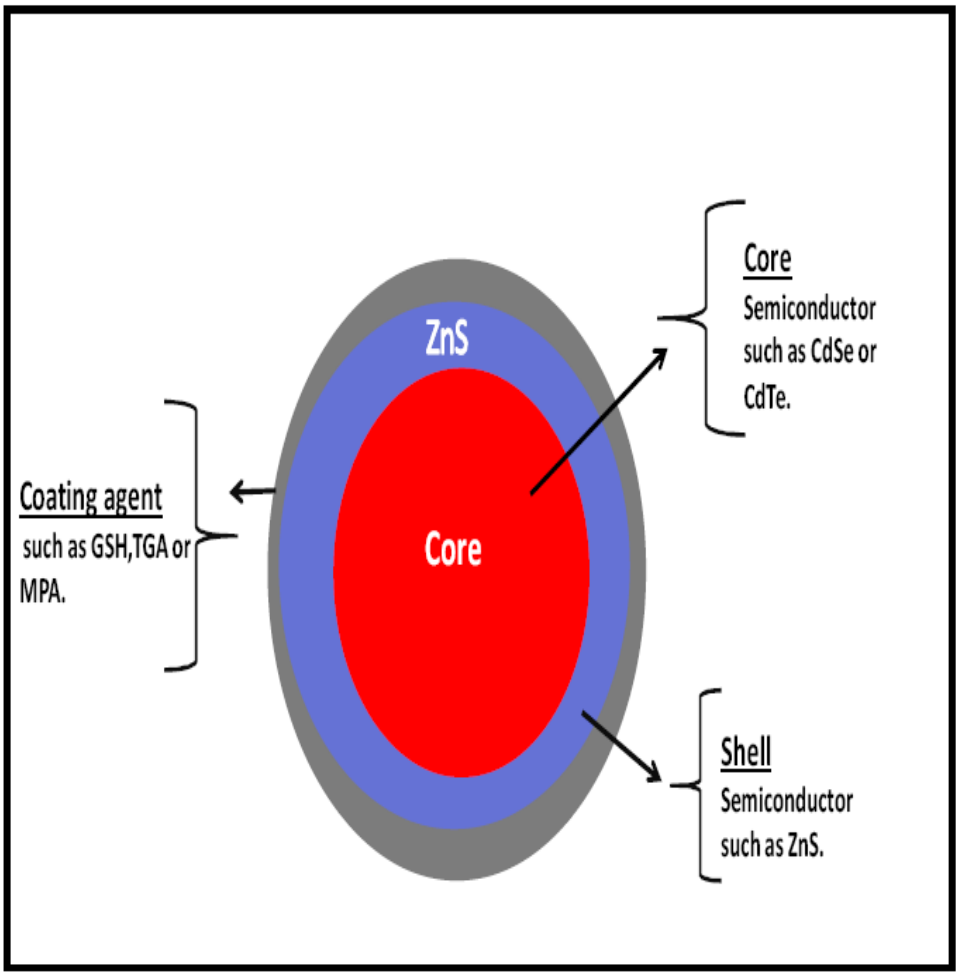

Figure 1.3: Illustration of a core quantum dot encapsulated with ZnS shell and coated with a biocompatible material.

1.1.2 Synthesis of water soluble QDs

QDs can be synthesized by either the top-down or bottom-up approach; in this work we used the bottom-up approach [24]. For the core (CdSe), this process, known as nucleation involves combining cadmium and selenium ions under inert atmosphere. The reaction is allowed to reach high temperatures (Oswald ripening) and the core is allowed to grow to a desired size. In this work zinc sulphide (ZnS) was used as a shell to coat the core QDs [25]. Application of QDs in biological systems is dependent on their solubility. In this work, to render the QDs water soluble, GSH was used as a capping agent. This ensured that the photophysical properties of the QDs were not altered while providing ($-NH_2$) groups on the surface of the QDs that would allow coordination to other biomolecules. In **Figure 1.4** the structures of the core and core shell QDs capped with water soluble GSH are shown.

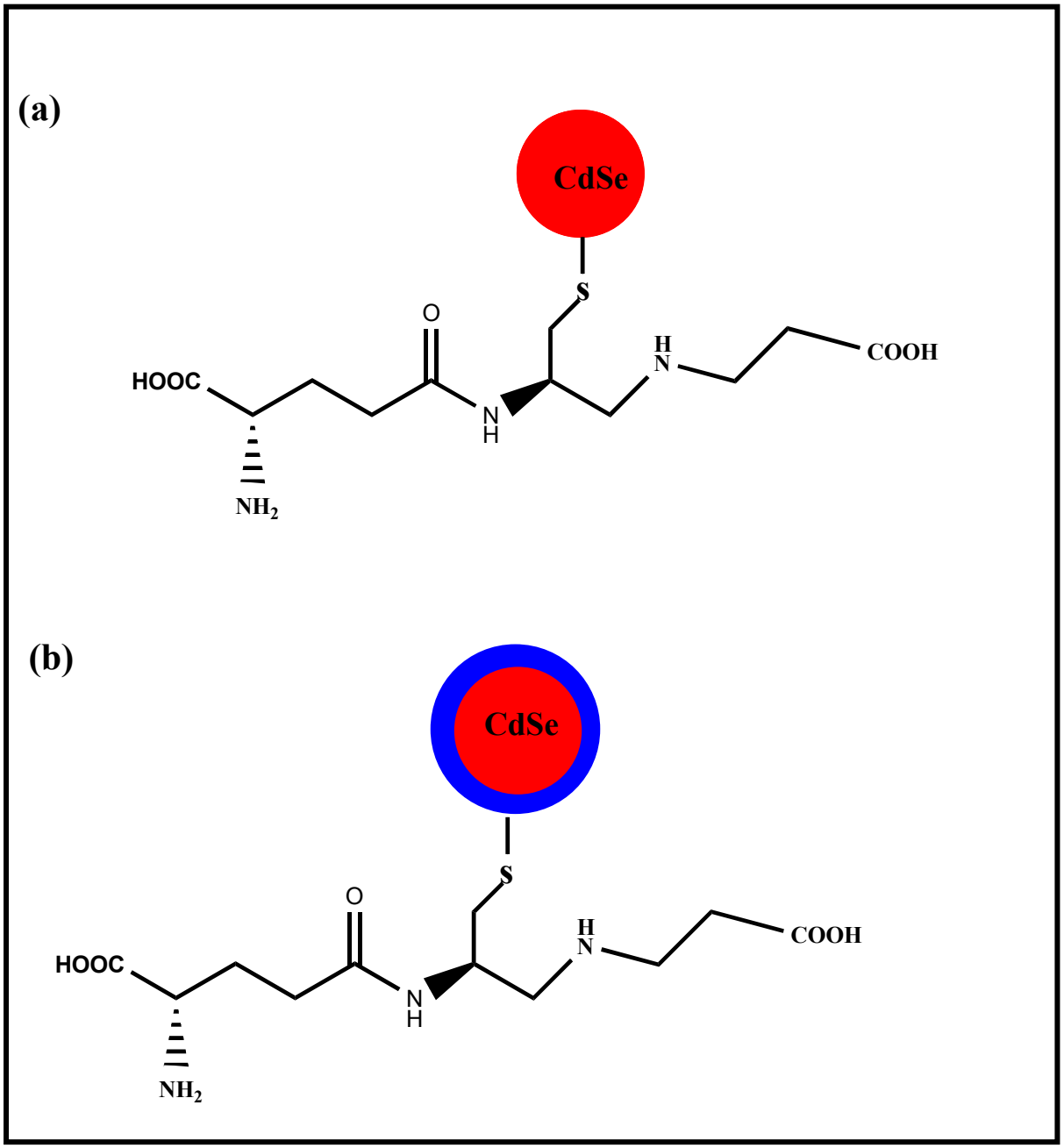

Figure 1.4: Structures of (a) core CdSe QDs and (b) core shell CdSe@ZnS QDs capped with GSH.

1.1.3 Quantum dot toxicity

The use of QDs in clinical applications has been limited by their potential toxicity. When introducing QDs in a biological system one needs to take into account the composition, toxicity, immunogenicity as well as ADME (absorption, distribution, metabolism and excretion) characteristics. The toxicity of the QDs varies, depending on core composition, surface coating, surface charge and the size of the QDs [26-28]. There have been very few studies designed primarily for toxicological assessment of QDs (i.e dose, duration, frequency of exposure and mechanism of action) and as a result there has not been any systematic data in literature regarding QDs toxicity [29]. The core of the QDs may contain cadmium (e.g in CdSe or CdTe) which is the toxic component. Studies revealed that uncoated QDs were toxic at 1μg/ml level concentration in rat pheochromocytoma cells (PC12), which was the same toxicity level as cadmium ions (Cd^{2+}) on their own [26]. The study suggests that cadmium is released via surface oxidation and that the toxicity is from the core. Studies on human breast cancer MCF-7 cells have showed that CdTe@ZnS core shell or core CdTe capped with mercaptopropionicacid, cysteamine or n-acetylcysteine significantly reduced the toxicity, compared to the bare CdTe core. The presence of ZnS shell eliminated release of cadmium ions [30].

Tables 1.1 and 1.2 summarize recent work on QD toxicity *in vitro* and *in vivo* respectively [31-44]. In this work, we determined possible cytotoxic effects of a set of QDs by systematic photophysical evaluation *in vitro* as well as *in vivo*. QDs were synthesized by the hydrothermal aqueous route with sizes in the range of 2.0– 3.5 nm. Cytotoxic effects of QDs were studied in the human pancreatic carcinoid BON cell line. As **Tables 1.1 and 1.2** show, there has been no systematic study where the core or core shell with different coatings have been studied using the same cell line. Hence this is the aim of the work.

Table 1.1: Summary of QDs toxicity studies *in vitro* that have been reported in literature.

QD type	Shell	Coating agent	Biological model tested	Reference
CdSe	ZnS	DHLA	Dictyostelium discoideum and HeLa cells	**[31]**
CdSe	ZnS	None	HeLa cells	**[32]**
CdSe	ZnS	COOH,OH/COOH,OH, H_2/OH,NH_2, CdSe MAA,TOPO	WTK1 cells Primary cultures of rat hepatocytes	**[33]**
CdSe	ZnS	MUA	Vero and HeLa cell culture,primary cultures of human hepatocytes	**[28]**
CdSe	ZnS	SSA	EL-4 cells (mouse lymphocytes)	**[28]**
CdSe	ZnS	PEG Silanized	Human HSF-42 (skin fibroblast) & INR-90 (lung fibroblast) cell culture	**[36]**
CdSe	ZnS	Peptide	HEK 239T/17 &COS-1 (Africangreen Monkey) cell lines	**[35]**
CdSe	ZnS	Cysteine	MCF-7 (human breast cancer)	**[36]**

CdSe	None	None	Primary rat cell culture (hippocampal neuron)	**[37]**
CdSe	ZnS	PEG	CaCo-2 (human colon carcinoma) cell	**[38]**
CdTe	None	None	Rat pheochromocyto ma &murine microglial cell line	**[27]**
CdTe	ZnS	MPA, N-acetyl Cysteine	MCF-7 (human breast cancer) cell culture	**[39]**
CdTe	CdS,CdS/ZnS	None	K562 & HEK 293T human cell lines	**[40]**

DHLA = dihyrolipoic acid, CdSe = Cadmium selenide, CdTe = Cadmium telluride, TOPO = Trioctylphosphine oxide, MUA = Mercaptoundecanoic acid, SSA = Sheep serum albumin, PEG = polyethylene glycol, MTT = 3-(4, 5 dimethylthiazol-2-yl), 2, 5 dimethyl tetrazolium bromide, IVD = intravenously delivered, ZnS = Zinc sulphide, MPA = 3-mercaptopropionic acid

Table 1.2: Summary of QDs toxicity studies *in vivo* reported in literature.

QD type	Shell	Coating agent	Biological model tested	Reference
InAs	ZnS	DHLA/PEG	Subcutaneously & IV injected into rats & mice.	**[41]**
CdSe	ZnS	MUA/targeting Peptides, PEG	IVD into the tail of mouse.	**[41]**
CdSe	ZnS	LM, BSA	Intravenously injected into the rat.	**[42]**
CdSe	CdS	PEG	Intradermal injection into the mouse.	**[43]**
CdTe	ZnS	Monoclonal antibody for lung	IVD into the mouse.	**[44]**

DHLA = dihyrolipoic acid, CdSe = Cadmium sellenide, CdTe = Cadmium telluride, TOPO = Trioctylphosphine oxide, MUA = Mercaptoundecanoic acid, PEG = polyethylene glycol, IVD = intravenously delivered, ZnS = Zinc sulfide

1.1.4 Applications

The unique properties of QDs have allowed them to be used in various fields especially in fluorescence imaging. **Table 1.3** summarizes the properties of QDs that make them superior to traditional organic dyes in imaging [45-47]. It is as a result of these properties that QDs have been used in industrial and biological applications. Some examples of QDs being used in industrial applications include; in opto-electronics, electronics, data storage devices, photovoltaics and as photodetectors [48-54]. In biological applications, QDs are used as drug carriers, in bio-imaging (*in vivo* and *in vitro*), labeling, drug delivery, and photodynamic therapy (PDT) and pathogen toxin detection [48, 55, 56].

In this work we use QDs in photodynamic therapy (PDT) applications. PDT is a form of therapy that involves administrating a tumor localizing photosensitizing agent e.g a phthalocyanine, (Pc) followed by irradiation with light of appropriate wavelength (**Figure 1.5**) [57]. This results in the generation of cytotoxic singlet oxygen ($^1O_2$) by the photoexcited photosensitizer [58-61]. The use of QDs-Pc conjugates for PDT applications was first reported in 2003 [62]. QDs can be used in PDT either indirectly by transferring energy to a photosensitizer through Förster resonance energy transfer (FRET) mechanism (discussed below) **(Figure 1.6**), or directly as they react with molecular oxygen to generate reactive oxygen species (ROS) through triplet energy transfer (TET) (**Figure 1.7**). QDs generate singlet oxygen ($^1O_2$) with yields of 5% for CdSe [61] and 28% for coreshells [63].QDs can also enhance PDT activity of Pcs via the heavy atom effect, which is the enhancement of the rate of a spin-forbidden process by the presence of an atom of high atomic number.

In addition they can be used for imaging in PDT. Their photostability, high molar extinction coefficient, tunability of emission spectra and high photoluminescence quantum yields have made them ideal donors for FRET. In addition, the functionalization of the surface of QDs

also allows solubility, biocompatibility and localization of the QDs-Pc conjugate to a specific target site [63].

Table 1. 3: Table summarizing the advantages QDs have over traditional dyes.

Properties	**Traditional organic dyes**	**Quantum dots**
Emission spectrum	Asymmetrical and broad	Symmetrical and narrow
Excitation spectrum	Narrow	Broad
Photobleaching threshold	Low	High
Absorbance cross section	Low	High
Saturation intensity	Low	High
Quantum yield	Low	High
Decay lifetime	Fast (<5 ns)	Slow (30- 100 ns)

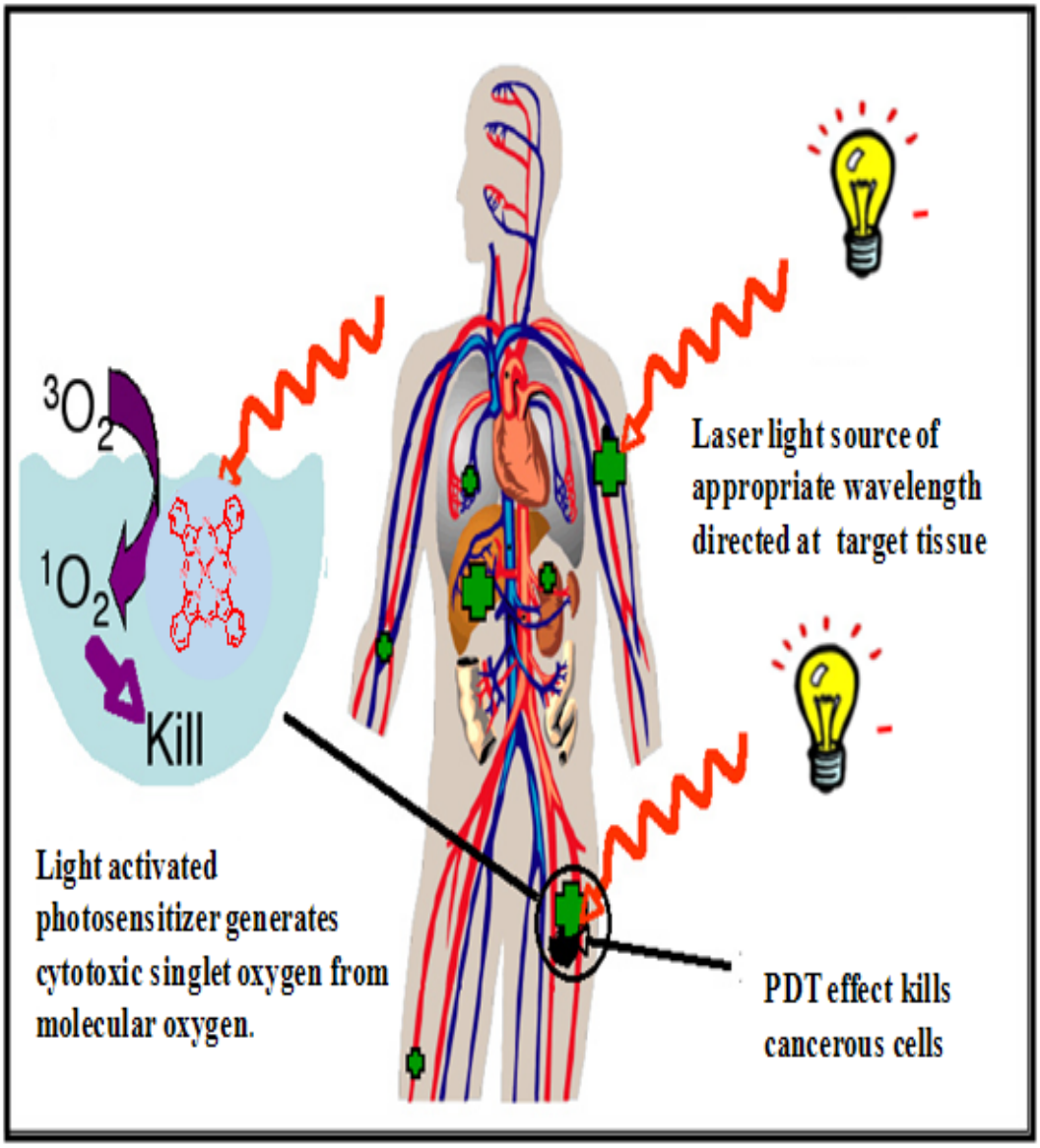

Figure 1.5: Schematic representation of Photodynamic therapy (PDT) using photosensitizer at specific wavelength, adapted from reference [57].

1.1.5 Förster resonance energy transfer

Förster resonance energy transfer (FRET) is a photophysical process where an electronically excited fluorescent donor molecule transfers its excitation energy non-radiatively to an acceptor molecule in a way that the excited state lifetime of the donor decreases and the acceptor is raised to higher energy states as illustrated in **Figure 1.6** [13, 64-66]. For efficient FRET to occur a few criteria should be satisfied, these include: (i) the fluorescence emission spectrum of the donor molecule must overlap the excitation or absorption spectrum of the acceptor chromophore, the degree of this overlap is referred to as spectral overlap integral (J),(ii) the donor and the acceptor should be in close proximity (1-10 nm) and (iii) the fluorescence lifetime of the donor should be long enough to allow FRET to occur [67-70].

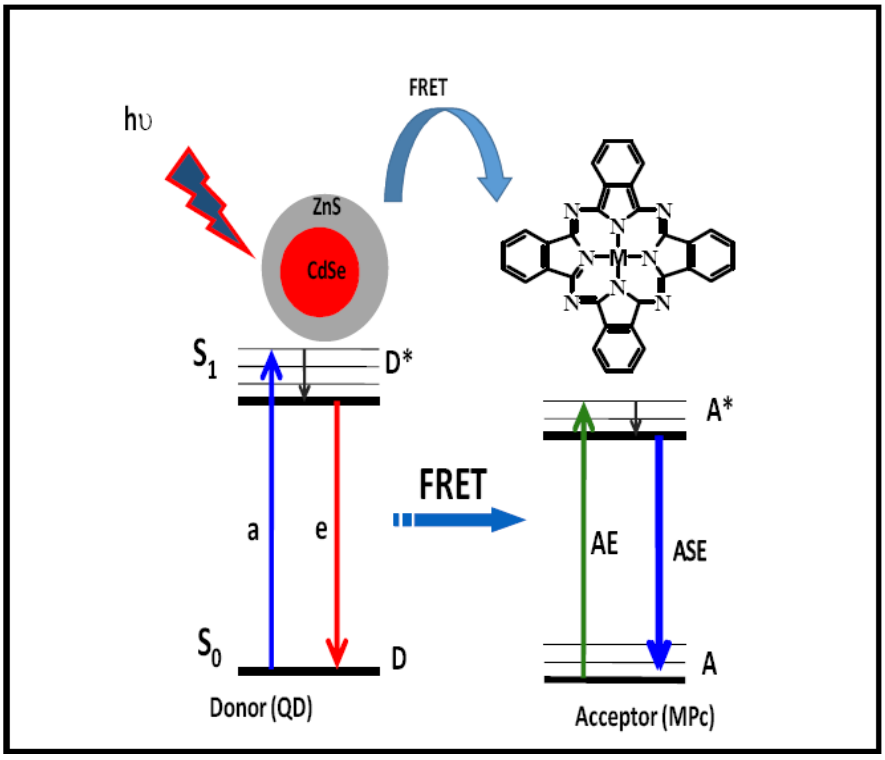

Figure 1.6: Schematic representation of Förster resonance energy transfer from donor molecules (QDs) to acceptor molecules (MPc). D = donor, A = acceptor, a = absorption, e = emission, AE= non-radiative acceptor excitation and ASE= acceptor sensitized emission [46].

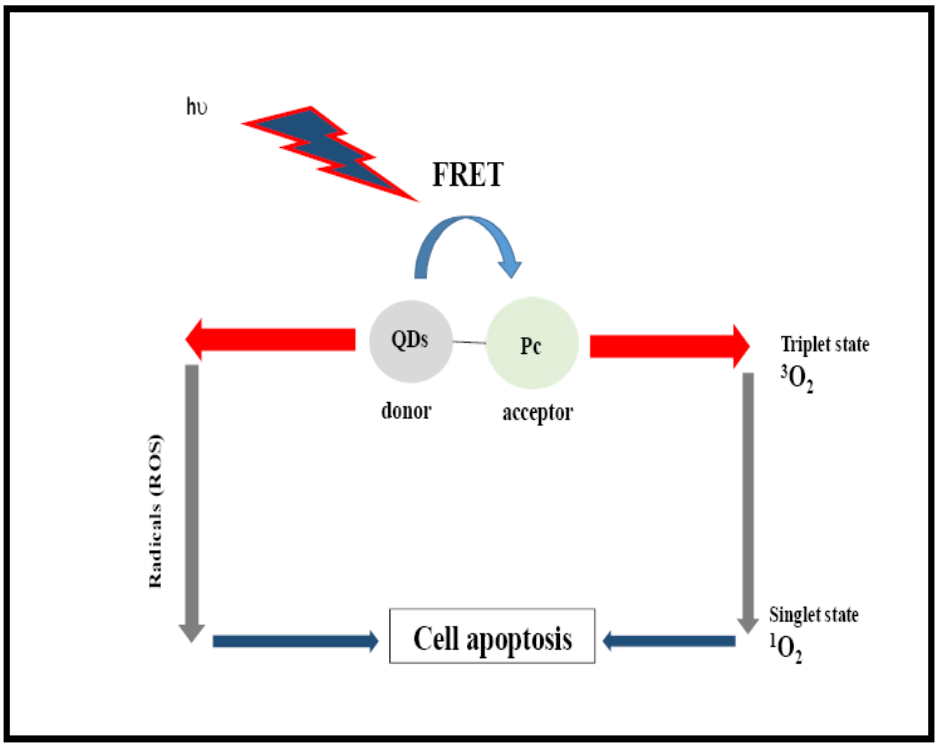

Figure 1.7: Photodynamic therapy mechanism using QDs-Pc conjugate. Light of specific wavelength in the presence of molecular oxygen will generate cytotoxic singlet oxygen; alternatively radicals could result in destruction of cancer cells.

Energy transfer from QDs to different phthalocyanines have been reported before [14, 15, 63, 71-78], but most researchers simply mixed the two together. Only a few studies have been reported for Pc covalently linked to QDs. **Table 1.4** summarizes known QDs-Pc conjugates that are covalently linked together found in literature [75-84]. Linking Pc to QDs is preferred as this allows the formation of controlled conjugates. The Pcs used in **Table 1.4** were not soluble in water, (with the exception of ZnTCPc and ZnOCPc), hence are not useful for biological applications. The central metal used for the water soluble Pcs was Zn. In this work the central metals used include the heavier Ga or In, which will encourage intersystem crossing (ISC) to the triplet state and hence improve the photophysical properties of the Pcs. Octacarboxyphthalocyanines are also used in this work since they are monomeric, because in solution aggregates are photoinactive.

Table 1.4: Examples of known pthalocyanines-quantum dot conjugates (linked) that have been reported in literature.

Quantum dots and capping	Phthalocyanine complex	Reference
CdTe MPA	ZnTAPc	**[75]**
	TmMTAAZnPc	**[78]**
	OmMTAAZnPc	**[78]**
	ZnAPPc	**[77]**
	ZnMAPPc	**[78]**
	ZnttbIPc	**[79]**
CdTe TGA	NiTAPc	**[75]**
	ZnAPPc	**[77]**
	ClInTAPc	**[75]**
	ZnMAPPc	**[78]**
CdTe L-cysteine	ZnAPPc	**[77]**
	ZnMAPPc	**[79]**
CdTe@Zns-CALNN	ZnMCsPc	**[82]**
	ZnMPCPc	**[82]**
	$(OH)_2$GeMCPc	**[82]**
CdTe@Zns-GSH	ZnOCPc	**[76]**
	ZnTCPc	**[76]**
	NiTAPc	**[83]**
CdSe@ZnS GSH	(Cl)AlMAPPc	**[84]**
	NiMMSA Pc	**[84]**

TmMTAAZnPc = [2, 3-[tetra- (mercaptopropanoic acid phthalocyaninto) zinc (II), OmMTAAZnPc = 2, 3-[octa-(2- mercapto-4-methyl-5-thiazoleaceticacid phthalocyaninto) zinc (II), ZnAPPc = zinc aminophenoxy Pc, ZnMAPPc = zinc mono amino Pc, ZnttbIPc = tris [9 (10),16 (17),23 (24)-tertbutyl] imidopthalocyanito zinc (II), ZnTAPc = zinc tetra amino Pc, NiTAPc = nickel tetra amino Pc, ClInTAPc = chloro indium tetra amino Pc,ZnMCsPc = zinc monocysteinyl Pc, ZnMPCPc = zinc mono phenoxy carboxy Pc, ZnOCPc = zinc octacarboxy pthalocyanine, ZnTCPc = zinc tetracarboxy pthalocyanine, CoTAPc = cobalt tetra amino Pc, NiMMSA Pc = nickel monomercaptosuccinic acid phthalocyanine

1.2 Magnetic nanoparticles

Magnetite is mainly composed of iron oxide (Fe_3O_4) and maghemite (γ-Fe_3O_4). Magnetite has a cubic inverse spinel structure [85]. It has a face-centered cubic closed packing formed by the oxygen molecules and the Fe cations occupying interstitial tetrahedral or octahedral sites [86], as shown in **Figure 1.8.** Magnetic iron oxide nanoparticles compared to other magnetic materials have good chemical stability, magnetic responsiveness and biocompatibility [87]. The important properties of magnetic nanoparticles (MNPs) relevant for medical applications are: low toxicity, water solubility, injectability and high-level of accumulation in target tissue [88-90].

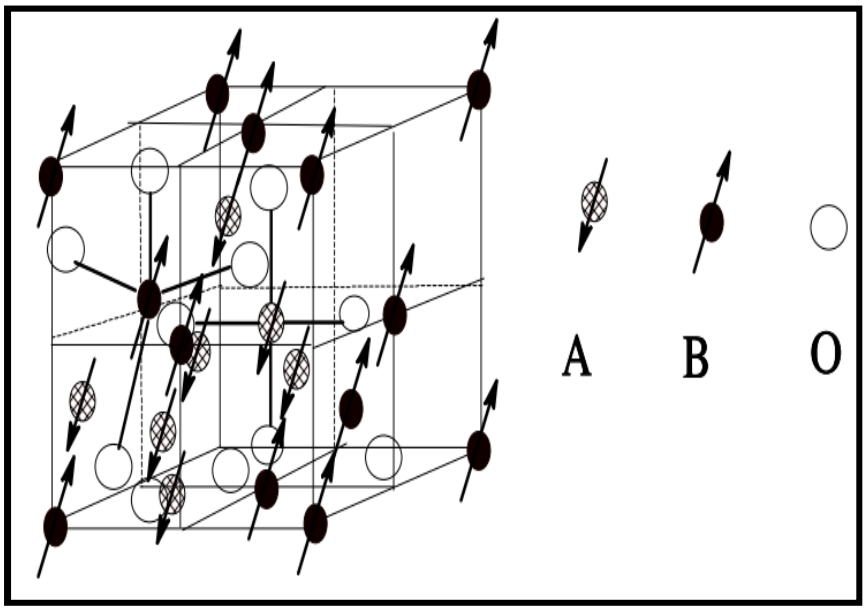

Figure 1.8: Schematic of a partial unit cell and magnetic ordering of spinel ferrite structure [85]. A and B are the two cationic sites in the spinel structure through which coordination occurs with oxygen. Fe_3O_4 as spinel ferrite is $FeFe_2O_4$ (AB_2O_4).

1.2.1 Synthesis and stabilization

Magnetic iron oxide nanoparticles (MNPs) can be prepared either in the aqueous or organic phase. Typically iron oxide nanoparticles are prepared through bottom-up strategies, such as co-precipitation, micro-emulsion, hydrothermal processing and thermal decomposition [85, 87, 91]. The co-precipitation method is the most commonly used approach due to its simplicity and efficiency; hence we make use of the method in this work. The stability of MNPs can be improved by grafting of polymers or surfactants on the surface of the nanoparticles, forming a layer that will generate an effective repulsive force between the nanoparticles and prevent flocculation [92]. The coating on the surface of the nanoparticles also prevents aggregation [93]. In this work we use 3-aminopropyltriethoxysilane (APTES) as a coating material for MNPs and also take advantage of the $-NH_2$ group on APTES, which will form an amide bond with the carboxy substituted phthalocyanine.

1.2.2 Applications

MNPs have attracted a lot of attention in various research fields and have great potential in magnetic resonance imaging (MRI), drug delivery [93, 94] and hyperthermia (HPT) [46]. In hyperthermia, superparamagnetic biocompatible nanoparticles in solution (magnetite) are injected into the tumour tissue where they are stimulated by an alternating current (AC) to produce heat between 41 ^{0}C and 46 ^{0}C, leading to tumour cell death [95,96]. Cancer cells are hypoxic (poorly oxygenated), compared normal cells which are anoxic (well oxygenated), this property makes cancer cells more sensitive to temperatures exceeding 41^{0}C compared to normal cells [88].

The combination of PDT and hyperthermia has advantages including the fact that hyperthermia increases the effectiveness of PDT, as higher temperatures will improve blood flow to tumors and better blood flow can deliver the drugs to the cancer cells. Also in HPT cellular uptake of oxygen in its ground state (heat results in the dilation of cells which allows free flow of oxygenated blood to the cells) will increase, which is essential to produce cytotoxic derivatives of oxygen in PDT [97, 98].

In this work, we synthesized MNPs and covalently link them to Pc to form a bi-functional anticancer agent, with the intention of combining hyperthermia with PDT **(Figure 1.9)**. Pcs have been linked to MNPs using ZnPc derivatives in literature [99-101]. This work used heavier central metals, Ga and In as central metals. Later in the work we also develop a three-in-one multifunctional nanocomposite, combining PDT (Pc), hyperthermia (MNPs) and fluorescence imaging (QDs).

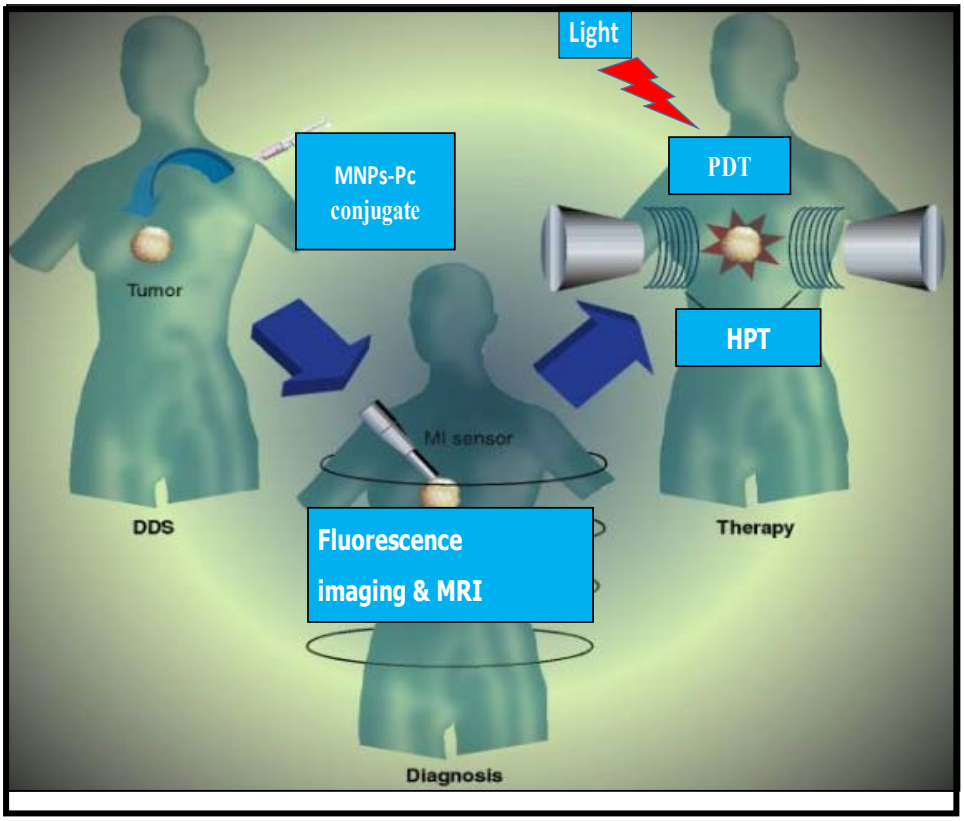

Figure 1.9: Schematic representation of therapeutic strategy using combined hyperthermia and photodynamic therapy. DDS = Drug delivery system, MI = Magneto impedance, MRI = Magnetic resonance imaging, HPT = hyperthermia and PDT = photodynamic therapy [98].

1.3 Phthalocyanines

Phthalocyanines are symmetrical, aromatic, macrocyclic compounds which have a conjugated system of 18π electrons [102-104]. These molecules have four isoindole groups that are linked by four nitrogen atoms, resulting in a closed ring [105], as shown in **Figure 1.10**.

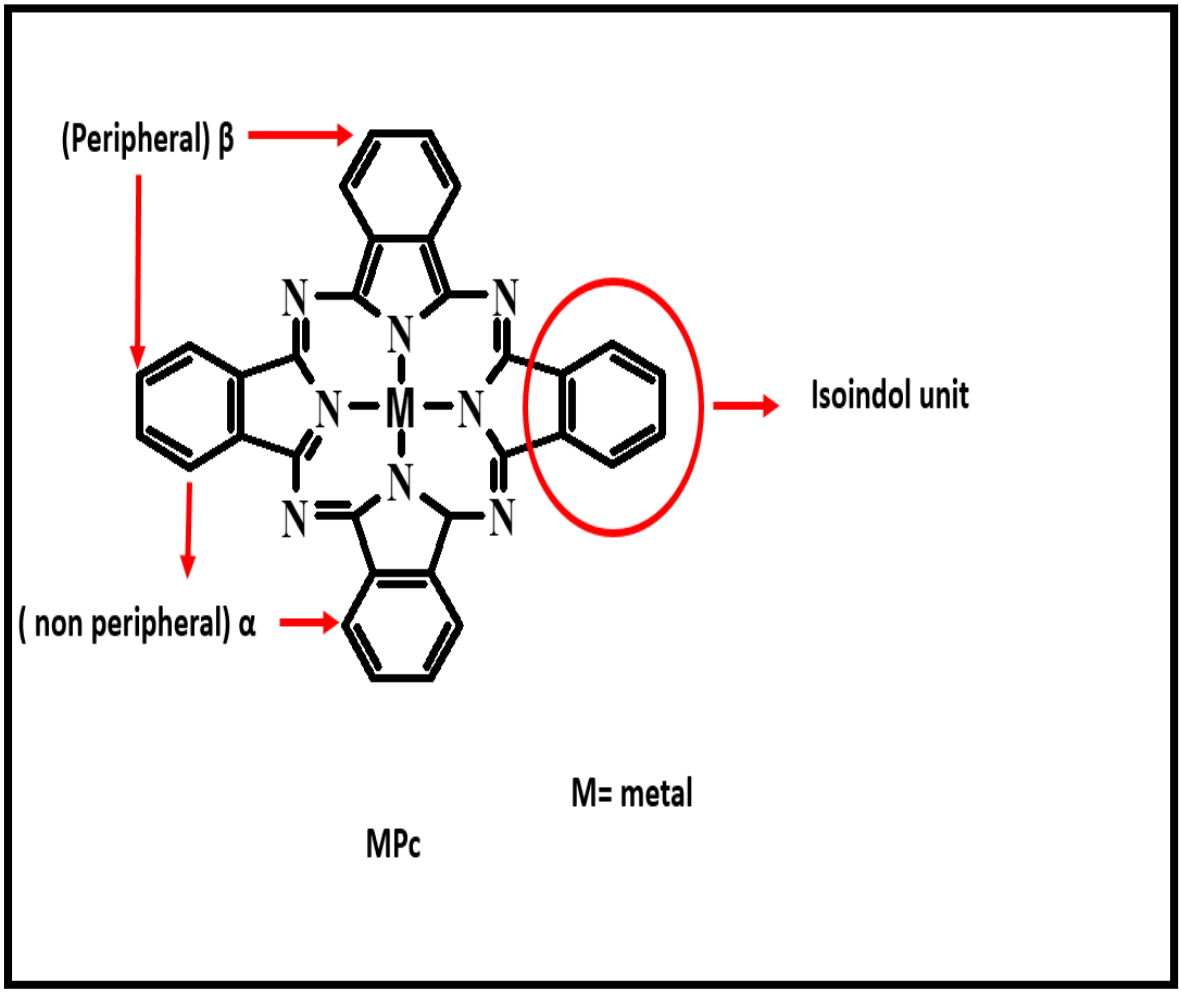

Figure 1.10: Molecular structure of metallopthalocyanine showing α, β positions and isoindol units.

Phthalocyanines form stable complexes with many metal ions (over 70 have been reported), and many metallophthalocyanines have been prepared by directly chelating metal cations with the four central nitrogens of the macrocycle, thus replacing the two central hydrogen atoms [102]. Metallating the Pc results in a move from an unmetallated D_{2h} symmetry to a metallated D_{4h} symmetry **Figure 1.11** [106]. Substituents can be placed on the peripheral and non-peripheral positions. The addition of substituents on the ring enhances the solubility and also alters the properties of the Pc [106,107]. Properties such as strong absorption in the red region of the spectrum, high thermal and chemical stability, and extinction coefficients of the order of 10^5 M^{-1} cm^{-1} [102-108], have led to the use of phthalocyanines in a variety of applications.

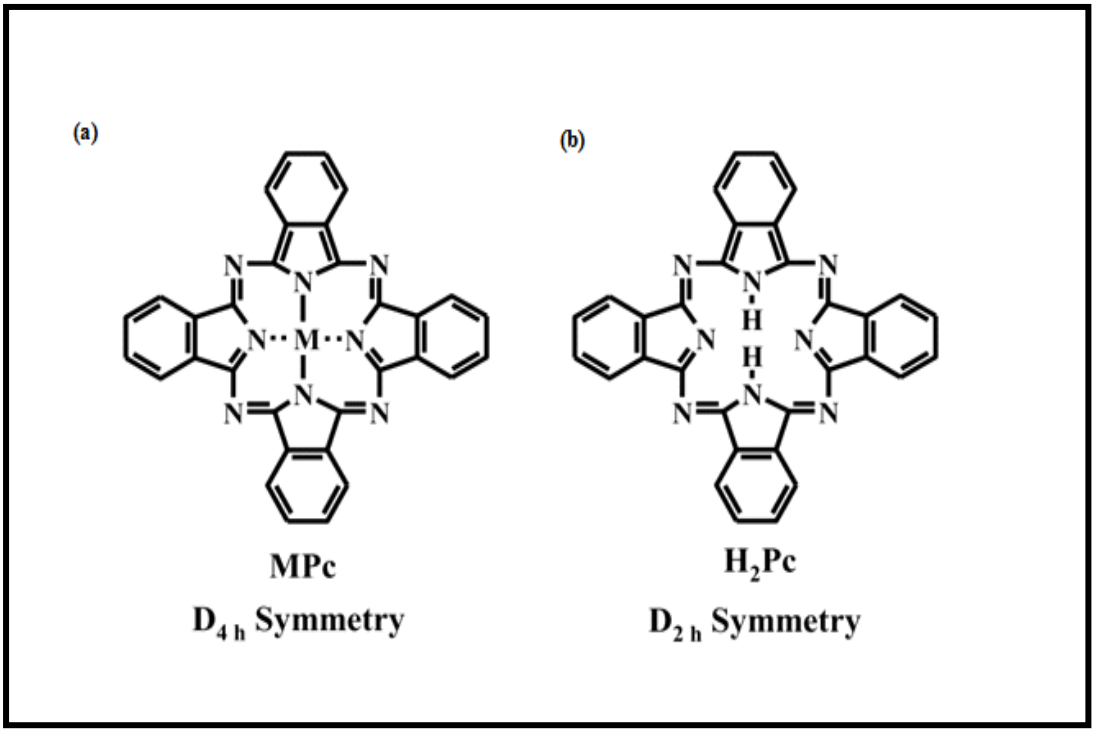

Figure 1.11: Difference between (a) metallated MPc with D_{4h} symmetry and (b) unmetallated MPc with D_{2h} symmetry.

1.3.1 Synthesis of octacarboxy phthalocyanines

Various octacarboxy metallophthalocyanines were employed in this study. They are synthesized by reacting benzene,1,2,4,5-tetracarboxylic dianhydride (pyromellitic dianhydride), urea (solvent and source of nitrogen) and 1,8-diazabicyclo [5.4.0]undec-7-ene (DBU- catalyst) with an appropriate amount of metal salt to form an intermediate product; an octa-amide, **Scheme 1.1** [109]. Hydrolysis of the intermediate by reacting it with sulphuric acid results in conversion of the amido groups into carboxylic groups, thus forming a water-soluble octacarboxy metallophthalocyanine (MOCPc) [109].

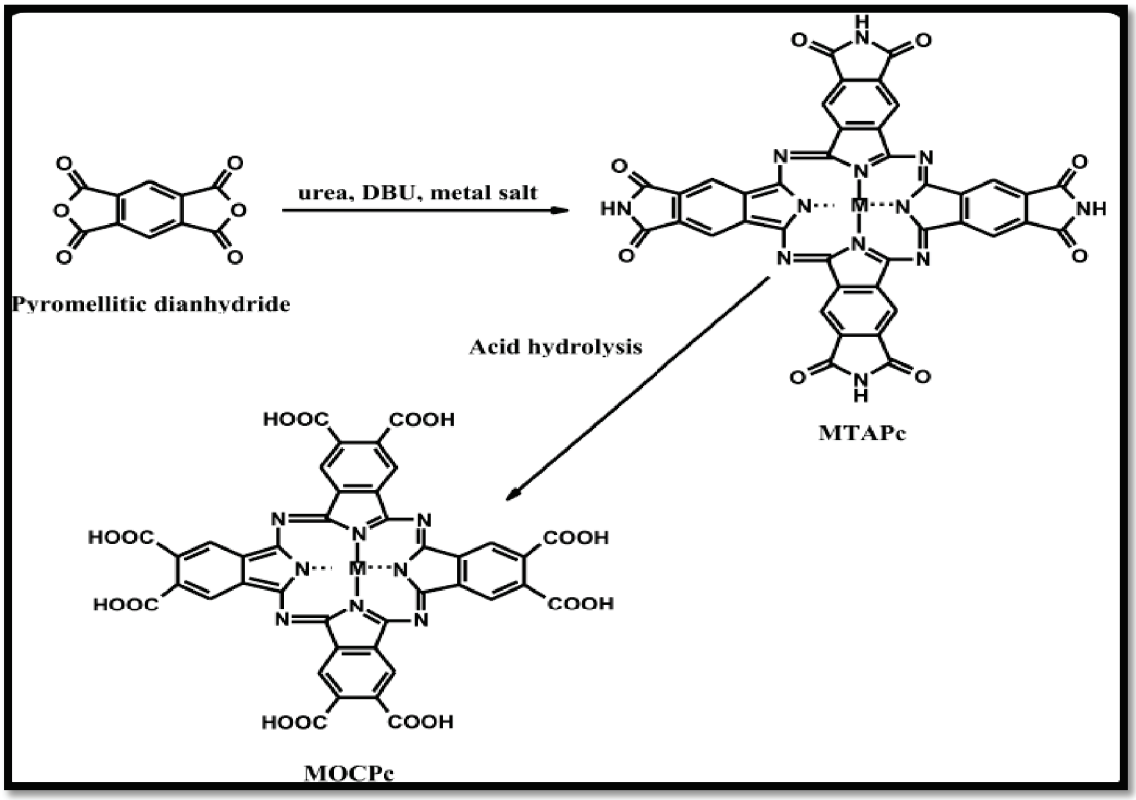

Scheme 1.1: Synthesis of water-soluble octacarboxymetallophthalocyanine (MOCPc) [109].

1.3.2 Electronic and absorption properties of Pcs

Typical absorption spectra of a monomeric Pcs consist of two very distinct bands: a narrow Q band around 670 nm and a weaker Soret band (B band) in the UV region around 350 nm, **Figure 1.12** [99]. The bands are a result of π-π* transitions within the delocalized 18π electron system of the ring. The B band is a result of superimposition of the B_1 and B_2 bands. When using transparent solvents, the N, L, C bands can be observed at high energy [102]. A charge transfer (CT) band may also be observed for diamagnetic Pcs such as Zn and Mg phthalocyanines [107].

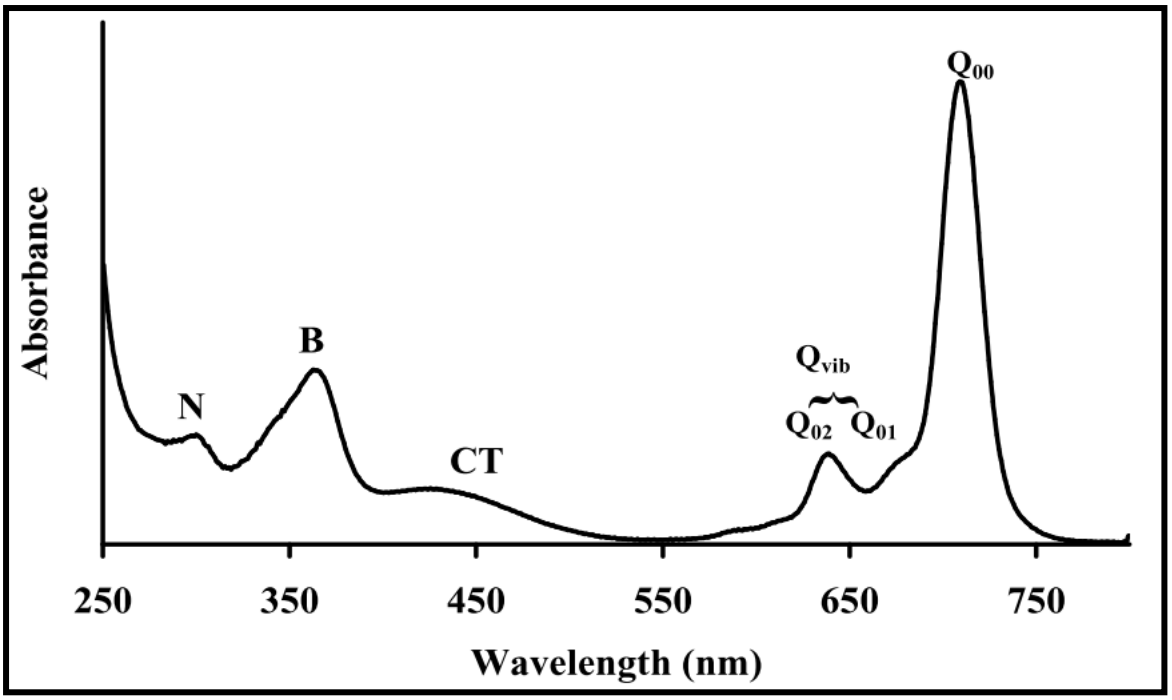

Figure 1.12: Typical ground state absorption spectra of phthalocyanine [99].

1.3.3 Applications

Phthalocyanines have found applications in many areas, including their use in molecular electronics, semiconductors and photonics [110], as electrocatalysts, in electrochemical sensor development [111, 112] and in medicine as photosensitisers in photodynamic therapy (PDT) [102]. Of interest in this study is using phthalocyanines in PDT applications. Phthalocyanines are used due to the fact that they are able to accumulate in the cancerous tissue for a long time and can be engineered to possess necessary energy requirements to produce singlet oxygen.

1.4 Combining multiple nanoparticles into a single nanosystem

The incorporation of diagnostic and therapeutic functions into a single nanoscale system for more effective and improved treatment has been of interest recently. Nanoparticles have potential as they are able to achieve dual functions if more than one type of nanostructure can be incorporated into a nano-assembly, which Sailor and Park [113] referred to as a "hybrid nanoparticle". The hybrid nanoparticle is made up of two or more nanoparticles assembled in a functional structure that itself is in nanoscale dimensions [114, 115]. The idea behind the development of hybrid nanoparticles is developing nanosystems that have biomedical properties that are superior to the individual components of the nanosystem. Another advantage is the ability to monitor the distribution of the drugs in the body which allows the efficacy and the progress of the therapy to be monitored.

There have been a few nanosystems developed for the cancer treatment that integrate two or more nanocomponents into single nanodevices [116,117]. These systems follow on the concept of a "theranostic" device, where both diagnostic and therapeutic functions are administered in a single dose [118]. Quantum dots and magnetic nanoparticles have been combined with other nanoparticles for possible medical applications [119-122].

Other nanoparticles such silica and gold have been used as drug carriers and are also designed to photothermally destroy the malignant tumour, respectively. **Table 1.5** summarizes examples of nanoparticles used for simultaneous therapeutic detection and diagnosis and treatment reported in literature [123-128].

Table 1.5 shows that apart from the work reported in reference [128] (in the absence of silica encapsulation), there have been no other reports on the type of multi-functional nanocomposites presented in this work.

Table 1.5: Nanoparticles used for simultaneous diagnostic and therapeutic detection and treatment of cancer

Structural component (therapeutic)	Functional component (diagnostic)	Target	Function	Reference
Multi walled carbon nanotubes	Magnetic nanocrystals	Murine renal carcinoma cells	Photothermal therapy and MRI	**[123]**
Single walled carbon nanotubes	Quantum dots	Head and neck squamous carcinoma cells and xenografts	Incorporating therapeutic molecule cisplatin and optical imaging	**[115]**
Multi walled carbon nanotubes	Magnetic nanocrystals	B_xPC-3 human pancreatic cancer cells	Incorporating therapeutic molecule gemcitabine and magnetic targetting	**[125]**
Gold nanorods	Magnetic nanocrystals	SK-BR-3breast cancer cells	Photothermal therapy, fluorescence imaging and MRI	**[126]**
Gold nanoshells	Magnetic nanocrystals	SK-BR-3breast cancer cells	Photothermal therapy and MRI	**[127]**
Phthalocyanine	Magnetic nanoparticles& Quantum dots	_	PDT, imaging and hyperthermia	**[128]**

In this work we develop a hybrid nanoparticle that will be used to detect, monitor and treat cancer. The hybrid nanoparticle is made up of $_{L}$-glutathione capped quantum dots (GSH-CdSe@ZnS), amino functionalized Fe_3O_4 magnetic nanoparticles (MNPs) and indium octacarboxy phthalocyanine ($ClInPc(COOH)_8$).

1.5 Photophysical and photochemical parameters

1.5.1 Fluorescence quantum yields and lifetimes

The amount of fluorescence emission from the singlet state is quantified by the fluorescence quantum yield (Φ_F). Quantum yields are defined as the number of photons taking part in an event for every photon absorbed. Therefore the fluorescence quantum yield (Φ_F) is defined by the number of molecules fluorescing per number of photons absorbed. The fluorescence quantum yield is determined by a comparative method [129]. In this work, AlPcSmix (a mixture of differently sulfonated AlPcs) in aqueous media, $\Phi_F = 0.44$ [130] was employed as a standard for Pcs, using **Equation 1.1** [129].

$$\Phi_F = \Phi_{F(std)} \frac{F.A_{std}.n^2}{F_{std}.A.n_{std}^2} \qquad \textbf{(1.1)}$$

where F and F_{std} are the areas under the fluorescence curves for sample and the standard, respectively, while n and n_{std} are the refractive indices of solvents in which the sample and the reference were dissolved, respectively. A and A_{std} are the absorbances of the sample and reference at the excitation wavelength respectively. Rhodamine 6G standard, dissolved in ethanol, $\Phi_F = 0.95$ [13], was employed for the determination of Φ_F value for the QDs. The fluorescence quantum yield values of the GSH-CdSe@ZnS after conjugation to the Pc ($\Phi_{F_{QD}}^{conjugate}$) were obtained using **Equation 1.2**

$$\Phi_{F(QD)}^{conjugate} = \Phi_{F(QD)} \frac{F_{QD}^{conjugate}}{F_{QD}} \qquad \textbf{(1.2)}$$

where Φ_F is the fluorescence quantum yield of the QDs alone and used as standard, $F_{QD}^{conjugate}$ is the fluorescence intensity of the QDs in the conjugate with the Pc when the excitation wavelength is that of the QDs (480 nm), F_{QDs} is the fluorescence intensity of the QD alone at the same excitation wavelength, both the QDs and conjugates were in the same solvent.

1.5.2 Triplet quantum yields and lifetimes

The ability of a molecule to populate the triplet excited state and be long lived is essential in photodynamic therapy applications. The comparative method was employed for the determination of triplet quantum yields using $AlPcS_{mix}$ as standard. Laser flash photolysis is a technique used to measure triplet absorbance and this is directly related to the triplet quantum yields of photosensitizers [130,131]. The triplet state parameters determined include the triplet quantum yields (Φ_T) and triplet lifetimes (τ_T). The triplet lifetimes are determined from the triplet decay curve **(Fig 1.13)** using the OriginPro 8 software. The triplet quantum yield (Φ_T) is used to determine the population of the phthalocyanine in the triplet state. The phthalocyanines usually have triplet absorption spectra in the region of ~ 500 nm.

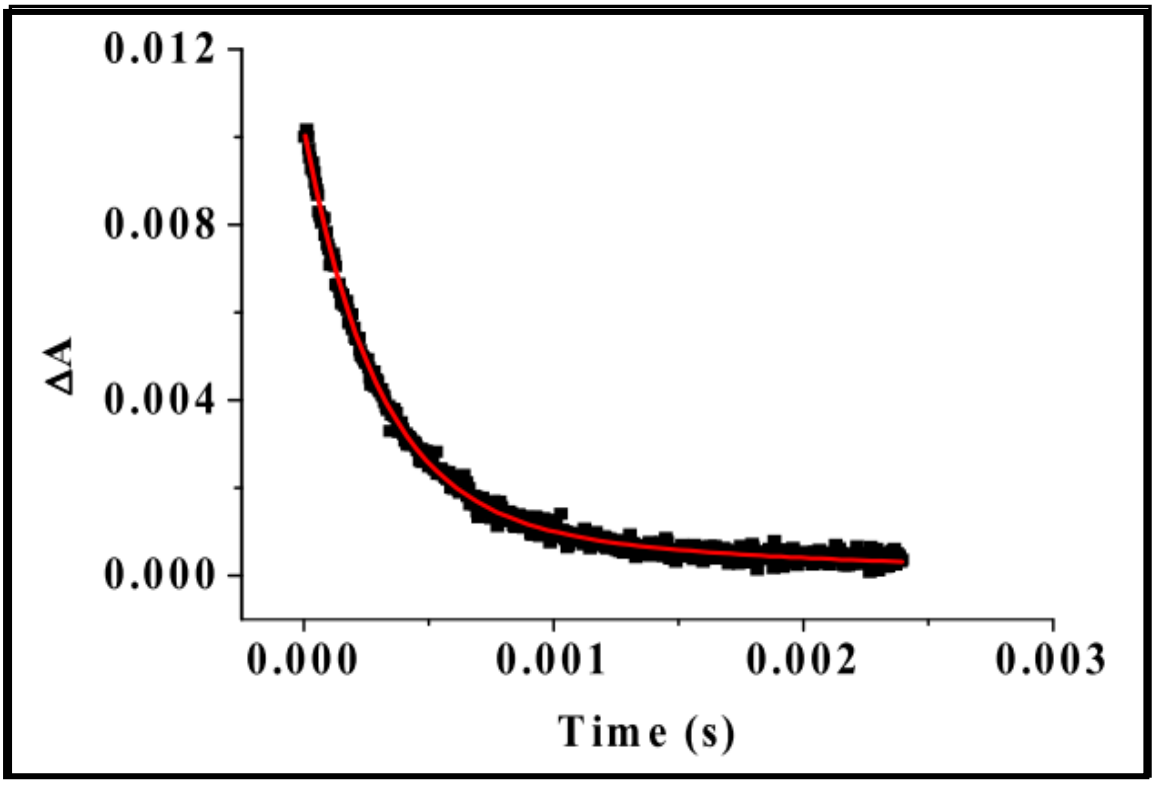

Figure 1.13: Typical triplet decay curve of a water soluble Pc (unpublished work).

The triplet quantum yields (Φ_T^{Sample}) may be determined using a comparative method which is based on the decay of the triplet state using **Equation 1.3**

$$\Phi_T^{Sample} = \Phi_T^{Std} \frac{\Delta A^{Sample} \varepsilon^{Std}}{\Delta A^{Std} \varepsilon^{Sample}} \textbf{(1.3)}$$

where ΔA^{sample} and ΔA^{std} are the changes in the triplet state absorbance of the Pc derivative and the standard, respectively. ε^{Sample} and ε^{std} are the triplet state extinction coefficients for

the sample and standard, respectively. Φ_T^{Std} is the triplet state quantum yield for the standard, where $\Phi_T^{Std} = 0.44$ for AlPcSmix in water [130].

The photophysical parameters i.e. triplet quantum yield (Φ_T) and the fluorescence quantum yields (Φ_F), complement each other and should add up to 1, if there is no energy lost through internal conversion. This means that if the triplet quantum yield (Φ_T) value is high, a corresponding low fluorescence quantum yield (Φ_F) will be obtained and vice versa.

1.5.3 Singlet oxygen quantum yield (Φ_Δ)

The excited triplet state molecule (^{3}**MPc***) may transfer its energy to ground state triplet molecular oxygen ($^3\mathbf{O_2}$), since the energy of the triplet state molecule (^{3}**MPc***), (**Scheme 1.2**) is higher (~110 – 126 kJ mol^{-1}) than the energy required (~94 kJ mol^{-1}) for the excitation of ground state molecular oxygen [132], to form excited singlet oxygen ($^1\mathbf{O_2}$), through the Type II mechanism.

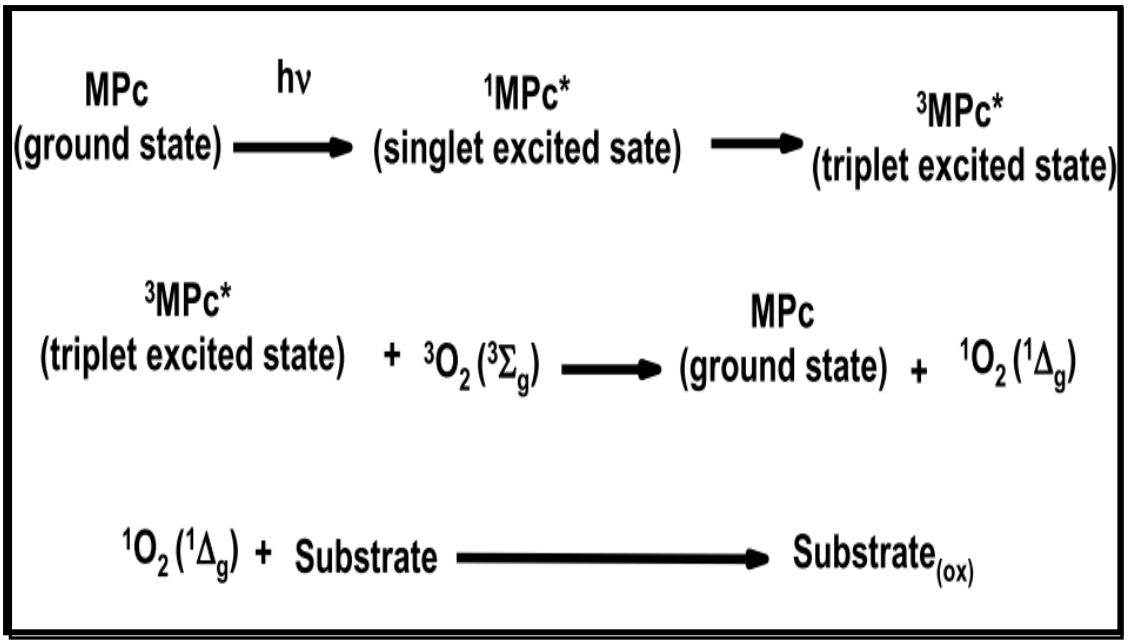

Scheme 1.2: Type II mechanism for the photoreaction of MPc leading to the production of singlet oxygen.

There are other mechanisms (Type I or Type III) through which the photosensitization process could occur. Type I mechanism involves free radicals [132]. While in Type III, electron transfer from the substrate to the excited state sensitizer may occur [133]. The involvement of Type II mechanism is widespread in oxygen-rich and air saturated environments where the oxygen concentration is very high and it is believed that Type II mechanism is dominant in photosensitization reactions. The singlet oxygen quantum yields (Φ_Δ) can then be calculated **Equation 1.4**

$$\Phi_\Delta = \Phi_\Delta^{Std} \frac{R \,.\, I_{abs}^{Std}}{R^{Std} \,.\, I_{abs}} \quad \textbf{(1.4)}$$

where Φ_{Δ}^{Std} is the singlet oxygen quantum yield for the standard, R and R_{Std} are the singlet oxygen quenchers (e.g tetrasodium α,α-(anthracene-9,10-diyl) dimethylmalonate (ADMA) in aqueous media) photobleaching rates in the presence of the respective MPcs under investigation and of the standard (such as AlPcSmix) respectively. I_{abs} and I_{abs}^{std} are the rates of light absorption by the MPcs and the standard, respectively. In this method of calculating the singlet oxygen, the quencher is normally mixed with the photosensitizer solution and the mixture is irradiated typically where the MPc absorbs. The decrease of the quencher absorption maximum is monitored spectroscopically and serves as a monitor for singlet oxygen generation.

1.5.4 FRET Parameters

FRET efficiency (*Eff*) can be determined from the fluorescence quantum yields of the donor in the absence ($\Phi_{F\,(QDs)}$) and presence ($\Phi_{F\,(QDs)}^{conjugate}$) of the acceptor using **Eq. 1. 5** [134]:

$$Eff = 1 - \frac{\Phi_{F(QD)}^{conjugate}}{\Phi_{F(QD)}} \qquad \textbf{(1.5)}$$

FRET efficiency (*Eff)* is related to r (Å) by **Eq. 1.6** [134]

$$Eff = \frac{R_0^6}{R_0^6 + r^6} \textbf{(1.6)}$$

where r represents the centre-to-centre separation distance (in Å) between the donor and the acceptor, R_0 (the Förster distance, Å) is the critical distance between the donor and the acceptor molecules at which the efficiency of energy transfer is 50 % and depends on the quantum yield of the donor **Eq. 1.7** [134]:

$$R_0^6 = 8.8 \text{ x} 10^{23}\, k^2 n^{-4} \Phi_{F(QDs)} J \qquad \textbf{(1.7)}$$

where k is the dipole orientation factor, n is the refractive index of the medium, $\Phi_{F\,(QDs)}$ is the fluorescence quantum yield of the donor and J is Förster overlap integral, given by **Eq. 1.8**

$$J = \int f_{(QDs)}\,(\lambda)\varepsilon_{MPc}\,(\lambda)\lambda^4\,\partial\lambda \qquad \textbf{(1.8)}$$

Where $f_{(QDs)}$ is the normalized QD emission spectrum. ε_{MPc} and λ are respectively, the molar extinction coefficient and the wavelength at the Q band maxima for Pc. It is assumed that k^2 is 2/3.This assumption is normally made for donor-acceptor pairs in a liquid medium, which are considered to be isotropically oriented during their lifetime. FRET parameters were computed using the program PhotochemCAD [134].

1.6 Summary of aims

1. Determine possible cytotoxic effects of a set of quantum dots (different cores, coreshells and capping agents) by systematic photophysical evaluation *in vivo* and *in vitro*.
2. Use the quantum dots determined to be the least cytotoxic (GSH-CdSe@ZnS) to conjugate to the ClGaPc$(COOH)_8$ to form a bi-functional anti-cancer agent by incorporating the properties of the quantum dots and phthalocyanine. Also evaluating the photophysical parameters of the core (GSH-CdSe) QDs and different sized coreshell (GSH-CdSe@ZnS) QDs when conjugated to the ClGaPc$(COOH)_8$.
3. Conjugate the ClInPc$(COOH)_8$ separately to magnetic nanoparticles to form a bi-functional anti-cancer with the intention of combing hyperthermia and PDT. In addition, GSH-CdSe@ZnS QDs were also conjugated separately to ClInPc$(COOH)_8$ to form a bi-functional anti-cancer agent (PDT and imaging). Evaluate the photophysical parameters of the conjugates.
4. Develop a multifunctional nanocomposite composed of GSH-CdSe@ZnS, magnetic nanoparticles and ClInPc$(COOH)_8$, which has potential to detect, monitor and treat cancer. The photophysical parameters of the nanocomposite were evaluated.
5. Application and testing some of the conjugates in PDT studies using human carcinoma BON cells and *in vivo* using chicken chorioallantoic membrane assay (CAM).

CHAPTER 2

This chapter provides information on the materials, instrumentation and synthetic procedures used in this work.

2. Experimental

2.1 Materials

For synthesis and characterization: Benzene-1,2,4,5-tetracarboxylic dianhydride (pyromellitic dianhydride), 1,8-diazabicyclo [5.4.0]undec-7-ene (DBU), indium chloride, 1-ethyl-3-(3-dimethyl aminopropyl) carbodiimide hydrochloride (EDC), N-hydroxysuccinimide (NHS), CdO, sulphur powder, zinc powder, glutathione (GSH), oleic acid, tetraethoxysilane (TEOS), 1-octadecene, trioctylphosphine oxide (TOPO) and sellinium powder. Aluminium oxide 90 (0.04 – 0.200 mm) and sodium and potassium hydroxide pellets (98%) were purchased from Sigma–Aldrich. AlPcSMix (containing a mixture of sulfonated derivatives), used as a standard was synthesized according to literature methods [135].

Solvents: Methanol, chloroform, acetone, ethanol, dimethylsulfoxide (DMSO), toluene, hydrochloric acid (32%) were purchased from Fluka, while dimethyl formamide (DMF) was purchased from SAARCHEM.

All solvents were dried as described by Perrin and Armarego [136] before use. All the other reagents used were of analytical grade and used without prior purification.

Aqueous solutions were prepared using Millipore water Milli-Q Water Systems (Millipore Corp., Bedford, MA, USA). Phosphate-buffered solutions (PBS) of pH 7.4 were prepared using appropriate amounts of Na_2HPO_4, KH_2PO_4 and the respective chloride salts, and dissolved in ultra-pure water.

Cell work

Human pancreatic carcinoid BON cells, Ham's F-12/Dulbecco's Modified Eagle's medium (DMEM) (1:1) medium supplemented with 10% fetal calf serum (FCS, Biochrom), L-glutamine, penicillin and 100 µg/ml streptomycin, 1% glutaraldehyde, 0.1% crystal violet, 2% Triton X-100, 1 % Trypsin/Ethylenediaminetetraacetic acid (EDTA) were purchased from Biochrom AG, Berlin, Germany.

2.2 Instrumentation and Equipment

i. Ultra violet –visible spectra (UV-Vis) were recorded on a Shimadzu UV 2550 spectrophotometer. All spectral measurements were performed in a quartz cell of 1 cm path length.

ii. Infrared spectra (KBr pellets) were recorded on a Perkin–Elmer Spectrum 100 ATR FT-IR and Perkin–Elmer Spectrum 400FT-IR spectrometers.

iii. Elemental analyses were carried out on a Vario EL III MicroCube CHNS Analyzer.

iv. Fluorescence excitation and emission spectra were recorded on a Varian Eclipse spectroflourimeter.

v. Mass spectral data were collected with a Bruker AutoFLEX III Smartbeam TOF/TOF Mass spectrometer. The instrument was operated in positive ion mode using a mass range of 400-3000 amu. The voltage of the ion sources were set at 19 and 16.7 kV for ion sources 1 and 2, respectively, while the lens was set at 8.50 kV. The reflector 1 and 2 voltages were set at 21 and 9.7 kV, respectively. The spectra were acquired using dithranol as the MALDI matrix, using a 354 nm nitrogen laser as the ionising source.

vi. X-ray powder diffraction (XRD) patterns were recorded on a Bruker D8, Discover equipped with a proportional counter, Using Cu-K radiation (= 1.5405 Å, nickel filter). Data were collected in the range $2\theta = 15^{o}$ to 60^{o}, scanning at 1 min^{-1}. The filter time-constant and the slit width were 2.5 s per step and 6.0 mm respectively. Samples were placed on a silicon wafer slide. The X-ray diffraction data were processed using Eva (evaluation curve fitting) software. Baseline correction was performed on each diffraction

pattern by subtracting a spline fitted to the curved background and the full width at half maximum values used in this work were obtained from the fitted curves.

vii. Transmission electron microscopy (TEM) images were obtained using ZESISS LIBRA® 120 transmission electron microscope which operates at 90 kV, Formvar / carbon coated 300 copper mesh grids.

viii. ^{1}H-Nuclear magnetic resonance spectra (^{1}H-NMR) were recorded using a deuterated solvent using a Bruker AMX 400 MHz NMR spectrometer.

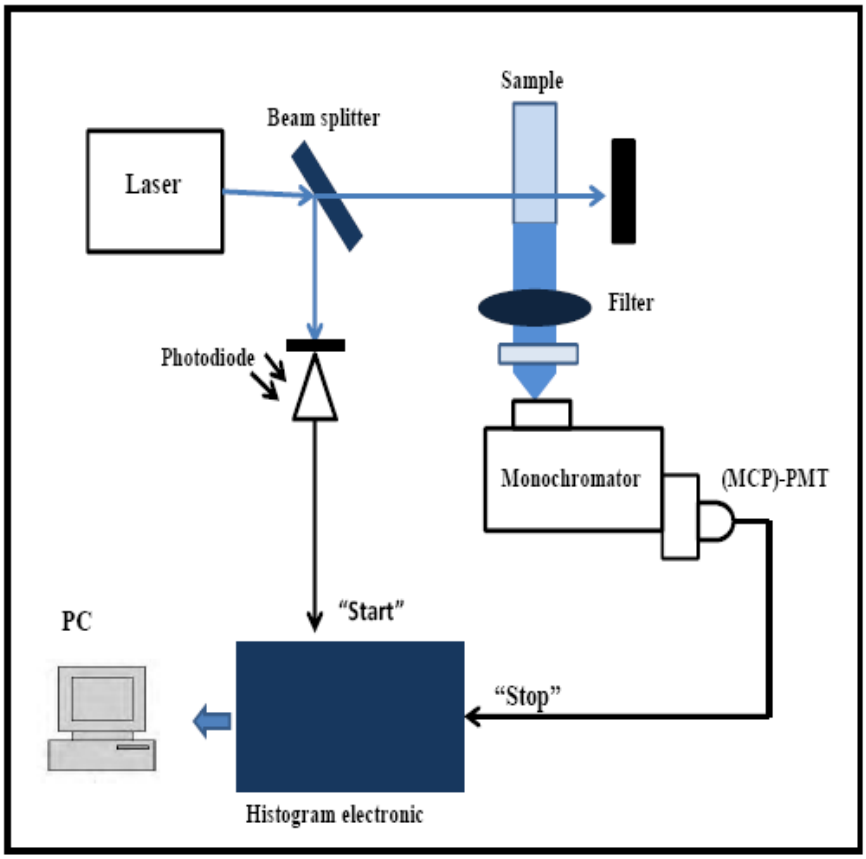

Figure 2.1: Schematic diagram of time-correlated single photon (TCSPC) set up. (MCP)-PMT= Monochromator photomultiplier tube, PC=Personal computer.

ix. Fluorescence lifetimes were measured using a time correlated single photon counting (TCSPC) setup **(Figure 2.1**) (FluoTime 200, Picoquant GmbH) with a diode laser (LDH-P-670 and LDH-P-480 (for QDs) with PDL 800-B, Picoquant GmbH, 670 nm or 480 nm, 20 MHz repetition rate, 44 ps pulse width). Fluorescence was detected under the magic angle with a Peltier cooled photomultiplier tube (PMT) (PMA-C 192-N-M, Picoquant) and integrated electronics (PicoHarp 300E, Picoquant GmbH). A monochromator with a spectral width of about 8 nm was used to select the required emission wavelength band. The response function of the system, which was measured with a scattering Ludox solution (DuPont), had a full width at half-maximum (FWHM) of 300 ps. All luminescence decay curves were measured at the maximum of the emission peak and lifetimes were obtained by deconvolution of the decay curves using the FluoFit Software program (PicoQuant GmbH, Germany). The support plane approach [13] was used to estimate the errors of the decay times.

x. A laser flash photolysis (**Figure 2.2**) system was used to determine the triplet quantum yields and lifetimes. The excitation pulses were produced by a Quanta-Ray Nd:YAG laser (1.5 J/9 ns), pumping a Lambda Physik FL 3002 dye laser (Pyridin 1 in methanol). The analysing beam source was from a Thermo Oriel xenon arc lamp and a photomultiplier tube was used used as a detector. The signals were recorded with a two channel 300 MHz digital oscilloscope (Tektronix TDS 3032C).

xi. Column chromatography was performed on aluminium oxide 90 (0.04 – 0.200 mm).

xii. Thermal gravimetric analysis (TGA) were performed on a Shimadzu DTG-TG 60H with a gas flow of 120 ml/min and operated under nitrogen atmosphere.

xiii. Fluorescence microscope from Zeiss (Axioskop 40, Jena, Germany), 546 nm, was employed.

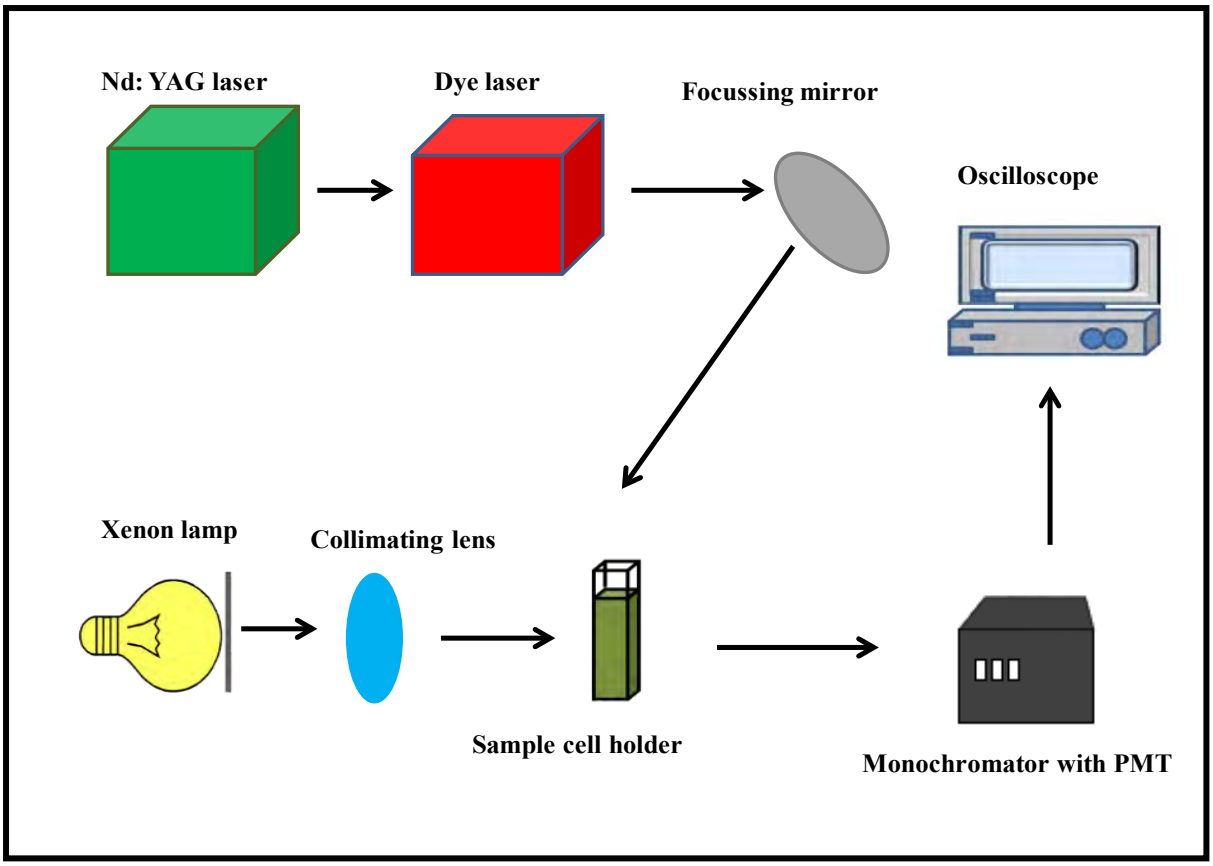

Figure 2.2 Schematic representation of laser flash photolysis set-up. PMT= photomultiplier tube.

2.3 Synthesis

The synthesis of the following QDs have been reported before: L-cysteine-CdTe [137], TGA-CdTe [137], MPA-CdTe [137, 138], MPA-CdTe@ZnS [139], GSH-CdTe@ZnS [84] and TGA-CdSe [138,140].

2.3.1 Synthesis of CdSe@ZnS-GSH QDs

GSH-capped CdSe@ZnS QDs were synthesized via previously described methods [141]with slight modifications. Briefly, 1.3 g (10.1 mmol) of CdO was added to a mixture of 30 mL oleic acid and 50 mL of 1-octadecene in a three-necked flask. The solution was heated to ~260 ºC under reflux and maintained under N_2 atmosphere to obtain a clear solution. The temperature of the solution was then lowered to 230 ºC and a solution of Se powder (0.3 g, 3.8 mmol) and 0.1 M TOPO in 25 mL of 1-octadecene (which was stirred for 24 hrs to obtain homogeneous slurry under N_2 atmosphere) was added to the flask. The size of the core CdSe QDs was controlled by further lowering the temperature of the solution.

Once the desired size of the core CdSe QDs was obtained, Zinc powder (0.40 g, 6.2 mmol), dissolved in 20 mL oleic acid and 30 mL 1-octadecene was added. Sulphur powder, 0.16 g (5.0 mmol) was also dissolved in 20 mL oleic acid and 30 mL 1-octadecene were alternately injected into the TOPO capped CdSe QDs solution to obtain the TOPO-capped CdSe@ZnS QDs. The QDs were then purified by washing with methanol followed by acetone. The TOPO capped CdSe@ZnS QDs are hydrophobic and therefore not suitable for biological applications. Water soluble GSH-capped CdSe@ZnS QDs were obtained via the ligand exchange route. Firstly, GSH-KOH methanolic stock solution was prepared by adding 2 mL (2 g (6.5 mmol)) of GSH separately to 3.0 g (53.4 mmol) of KOH in 40 mL methanol. The purified TOPO-capped CdSe@ZnS QDs were then re-dispersed in chloroform and GSH-KOH methanolic solution was subsequently added followed by the addition of Millipore

water. The solution was allowed to stir for 1 hr. The obtained water-soluble QDs were precipitated out with methanol, washed and centrifuged several times with acetone and dried under vacuum. The extinction coefficients of GSH-CdSe@ZnS QDs (used to determine concentration) were determined using literature methods [142]. The same method was used to estimate the extinction coefficient when GSH-CdSe@ZnS QDs were linked to the phthalocyanines employed in this work.

The syntheses of the following pthalocyanines; $AlPc(COOH)_8$ and $GaPc(COOH)_8$ have been reported before [143,144]. The synthesis of amino (APTES) functionalized iron oxide (Fe_3O_4) magnetic nanoparticles (MNPs) has been described in literature before [99].

2.3.2 Synthesis of $ClInPc(COOH)_8$

Octacarboxypthalocyaninto indium (III) chloride was synthesised according to the methods reported for other octacarboxy phthalocyanines [143,144] as follows: a mixture of benzene-1,2,4,5- tetracarboxylic dianhydride (pyromellitic dianhydride 2.50 g, 11.5 mmol), urea (13.0 g , 0.22 mol), $InCl_3$ (23.5 mmol, 5.19 g) and DBU (0.1 g , 0.7 mmol) as catalyst was heated to 250 °C in a flask until the reaction mixture was fused. The product was washed with water, acetone and 6 M hydrochloric acid. After drying, the product was hydrolyzed in 20% H_2SO_4 for 72 hrs. The products were further purified using column chromatography as explained in literature [143, 144].

Yield: (47%) **IR** (KBr, cm^{-1}): 3432 (OH) 1716 (C=O) 1381, 1273, 1184 (C-O). **^{1}H NMR** (400 MHz, D_2O): 7.82 ppm (s, 8H, Pc-H), 11.56 ppm (s, 8H carboxylic H). **UV-Vis** (0.1 M NaOH): λ max, nm (log ε), 691 (5.1), 351 (5.5) **MS** (m/z) : Calculated 1014 g/mol Found: 1010 (M-4H). Calculated for $C_{40}H_{16}O_{16}N_8InCl$: C 47.34, H 1.58, N 11.04; Found C 47.57, H 1.70, N 12.47

2.3.3. Covalent linking of GSH-CdSe or GSH-CdSe@ZnS to octacarboxyphthalocyanine (Pc) [(ClInPc(COOH)$_8$, ClGaPc(COOH)$_8$ or ClAlPc(COOH)$_8$)].

Pcs [(ClInPc(COOH)$_8$, ClGaPc(COOH)$_8$ or ClAlPc(COOH)$_8$)] were covalently linked to GSH-CdSe or GSH-CdSe@ZnS as follows: Pc (0.7 mmol) was dissolved in 10 ml dilute NaOH, then 2 mL of 1.2 mM EDC was added to activate the carboxylic group (-COOH) of the Pc. The mixture was allowed to stir for 48 hrs at room temperature under argon atmosphere. After this time, a mixture containing 2 mL of 1 mM NHS and GSH-CdSe@ZnS (0.003 g) was added to the activated Pc and the mixture was stirred for 12 hrs to allow conjugation of the Pc to the QDs to take place.

2.3.4. Covalent linking of ClInPc(COOH)$_8$ to Fe_3O_4 magnetic nanoparticles, (Scheme 5.1).

ClInPc(COOH)$_8$ (15 mg, 9.9 x 10^{-6} mol) was dissolved in 10 ml of PBS pH 7.4. EDC (0.23 g, 1.2 mmol) and NHS (0.115 g, 1 mmol) were added and the solution stirred for 3 hrs. The Fe_3O_4 magnetic nanoparticles (5 mg), dissolved in 10 mL of PBS pH 7.4, were added to the activated ClInPc(COOH)$_8$. The mixture was stirred for 12 hrs at room temperature under N_2 gas flow. The product was precipitated with ethanol, washed with ethanol and centrifuged to remove excess reactants. A magnet was employed to remove unreacted Pcs. The conjugate is represented as ClInPc(COOH)$_8$-MNPs.

2.3.5 Covalent linking of GSH-CdSe@ZnS QDs to Fe_3O_4 magnetic nanoparticles

GSH-CdSe@ZnS QDs (10mg) was dissolved 5 ml of PBS at pH 7.4. EDC (0.23 g, 1.2 mmol) and NHS (0.115 g, 1 mmol) were added and the solution stirred for 3 hrs. The Fe_3O_4 magnetic nanoparticles (5 mg), dissolved in 10 mL of PBS pH 7.4, were added to the activated QDs. The mixture was stirred for 12 hrs at room temperature under N_2 gas flow. The product was precipitated and washed with ethanol, and centrifuged to remove excess reactants. A magnet was employed to remove unreacted QDs. The conjugate is represented as QDs-MNPs.

2.3.6 Coating the QDs-MNPs conjugate with silica

The QDs-MNPs were encapsulated with silica; the silica layer is known to protect therapeutic or diagnostic molecules (i.e QDs-MNPs conjugate in this work) from degradation in the physiological environment. The mesoporous silica shell was formed by simultaneous sol-gel polymerization of tetraethoxysilane (TEOS). The QDs-MNPs conjugate was coated with silica using methods that have been described in literature [145]. Briefly, to a mixture of 1.77 ml of Triton-X 100, 1.8 mL of n-hexanol and 7.5 mL of cyclohexane 0.48 ml of QDs-MNPs solution (5 mg in 5 mL of PBS pH 7.4), 0.1 ml of TEOS, 6 ml of NH_4OH were consecutively added. The resulting mixture was stirred for 24 hrs. After this time, 20 mL of acetone was added followed by centrifuging and washing with ethanol. The resulting conjugate is represented as silica coated QDs-MNP.

2.3.7 Synthesis of multi-functional GSH-CdSe@ZnS QDs-magnetic nanoparticles – indium octacarboxyphthalocyanine nanocomposite, (Scheme 5.2)

$ClInPc(COOH)_8$ was attached on the surface of the silica coated-QDs-MNPs conjugate by taking advantage of the $–NH_2$ groups and using them as points of attachment. $ClInPc(COOH)_8$ was covalently linked to silica coated QDs-MNPs as described in **2.3.3** and is represented as $ClInPc(COOH)_8$-QDs-MNPs.

2.4 Cell studies

Human pancreatic carcinoid BON cells were used in this study. The BON cells were grown in a 1:1 mixture of Dulbeco modified eagle medium (DMEM) and Ham's F-12 medium containing 10% FCS and 1 % L-glutamine. The cell lines were kept at 37° C in a humidified atmosphere (5 % CO_2). The culture media was changed every second day and once a week the cells were passaged using 1% Trypsin/EDTA.

2.4.1 Uptake of GSH-CdSe@ZnS QDs

Cells grown on glass cover slips were incubated with QDs at concentrations of 0.2 and 0.4 μM for 4, 8 and 24 hrs. After the incubation period, samples were washed twice with PBS, then fixed with methanol (99%) at -20˚C for 20 min and again washed with PBS. Photographed area contained at least n = 10 cells. Uptake was measured using fluorescence microscope.

2.4.2 Cytotoxicity

The changes in cell numbers induced by QDs were evaluated by crystal violet staining as described in literature [146]. The growth inhibitory effect of the QDs on BON cancerous cells were performed after 48 hrs of continuous incubation with different concentrations of the respective QDs ranging from 0.1 to 5 μM. The cells in 96-well plates were fixed with 1% glutaraldehyde. The cells were then stained with 0.1 % crystal violet in phosphate buffered saline (PBS), the unbound QDs were removed by washing with water.

Bound QDs crystal violet was solubilized with 0.2 % Triton-X-100 in PBS. Light extinction, which increases linearly with the cell number was analysed at 570 nm using an ELISA microplate -reader.

2.4.3 Chicken chorioallantoic membrane assay (*in vivo*)

Embryotoxicity in terms of lethality and vein network degeneration was evaluated by chicken chorioallantoic membrane assay (CAM). Fertilized chicken eggs were incubated in an incubator at 37 ˚C in constant humidity for 15 days. After 7 days of incubation, a window was cut into the shell of each egg, then sealed with a tape and bred in the incubator for the following 4 days. On day 11 a tape was removed and the CAMs were treated with QDs – topically or intravenously. In the case of topical application a small silicone ring (5 mm in diameter) was placed onto the CAM and QDs in PBS or PBS alone were added (100 µl per egg, each day until day 15); in case of intravenous application a superficial CAM vein was injected with 10-15 µl of QDs-NaCl or NaCl using $30^{1}/_{2}$ G needle. Concentration of injected compound was counted based on total blood volume of 11 day-old embryo [147].

2.5 Photophysical studies

2.5.1 Fluorescence quantum yields and lifetimes

The fluorescence quantum yield for the Pcs were determined by a comparative method [129]. AlPcSmix as standard in aqueous media, Φ_F = 0.44 [130] was employed for the Pcs, **Equation 1.1**. For the determination of Φ_F values of QDs and their conjugates, Rhodamine 6G standard dissolved in ethanol, Φ_F = 0.95 [13] was employed. The absorbances of the solutions at the excitation wavelength were about 0.05 to avoid inner filter effects. The fluorescence lifetimes were evaluated from the tri-exponential decay curve of GSH-CdSe and GSH-CdSe@ZnS. A good fitting was judged by weighted residuals and χ^2 values. The calculation of the average fluorescence lifetime for the conjugates and QDs was achieved using the value obtained from the fit.

2.5.2 Triplet quantum yields and lifetimes

The decay kinetics of the triplet absorption of the Pcs were recorded using laser flash photolysis setup, **Figure 2.2**. The absorbance of the sample solutions and that of the standard were adjusted to be nearly 1.5 at their Q band maximum. All samples were introduced into a 1 cm quartz cell and then bubbled with argon for 10 min to remove dissolved oxygen before taking any readings. The triplet quantum yields of the sample phthalocyanines alone and in the presence of QDs were determined using **Equation 1.3.** Using AlPcSmix as standard in water Φ_T^{Std} = 0.44 [130].Triplet lifetimes were determined from kinetic data obtained using ORIGIN Pro software to fit the kinetics decay curves.

Results and Discussion

PUBLICATIONS

The results presented in the following chapters have either been published or submitted for publication. These articles are not referenced in this thesis.

1. Kuzyniak, Weronika; Adegoke, Oluwasesan; Sekhosana, Kutloano; D'Souza, Sarah; Tshangana, **Sesethu Charmaine Tshangana**; Hoffmann, Bjoern; Ermilov, Eugeny A.; Nyokong, Tebello; Hoepfner, Michael, Synthesis and characterization of quantum dots designed for biomedical use, *International Journal of Pharmaceutics* (Amsterdam, Netherlands) (2014), 466(1-2), 382-389.

2. **Charmaine Tshangana**, Tebello Nyokong, Improved triplet state parameters for indium octacarboxy phthalocyanines when conjugated to quantum dots and magnetite nanoparticles. *J.Mol.Structure 1089 (2015)161-169.*

3. **Charmaine Tshangana**, Tebello Nyokong. The photophysical properties of multi-functional quantum dots-magnetic nanoparticles – indium octacarboxy phthalocyanine nanocomposite. *J. Fluorescence, 25 (2015) 199-210.*

4. **Charmaine Tshangana**, Tebello Nyokong, Photophysical properties gallium octacarboxy phthalocyanines conjugated to CdSe@ZnS quantum dots.
   Spectrochim Acta: A, submitted for publication

CHAPTER 3

This chapter presents the results of the characterization and toxicity of quantum dots.

3. Characterization and toxicity of quantum dots

3.1 Characterization

The potential toxicity of seven different types of core and coreshells QDs and with different capping agents **(Figure 3.1)** were evaluated in order to determine which of the QDs were promising candidates for biological or medical use.

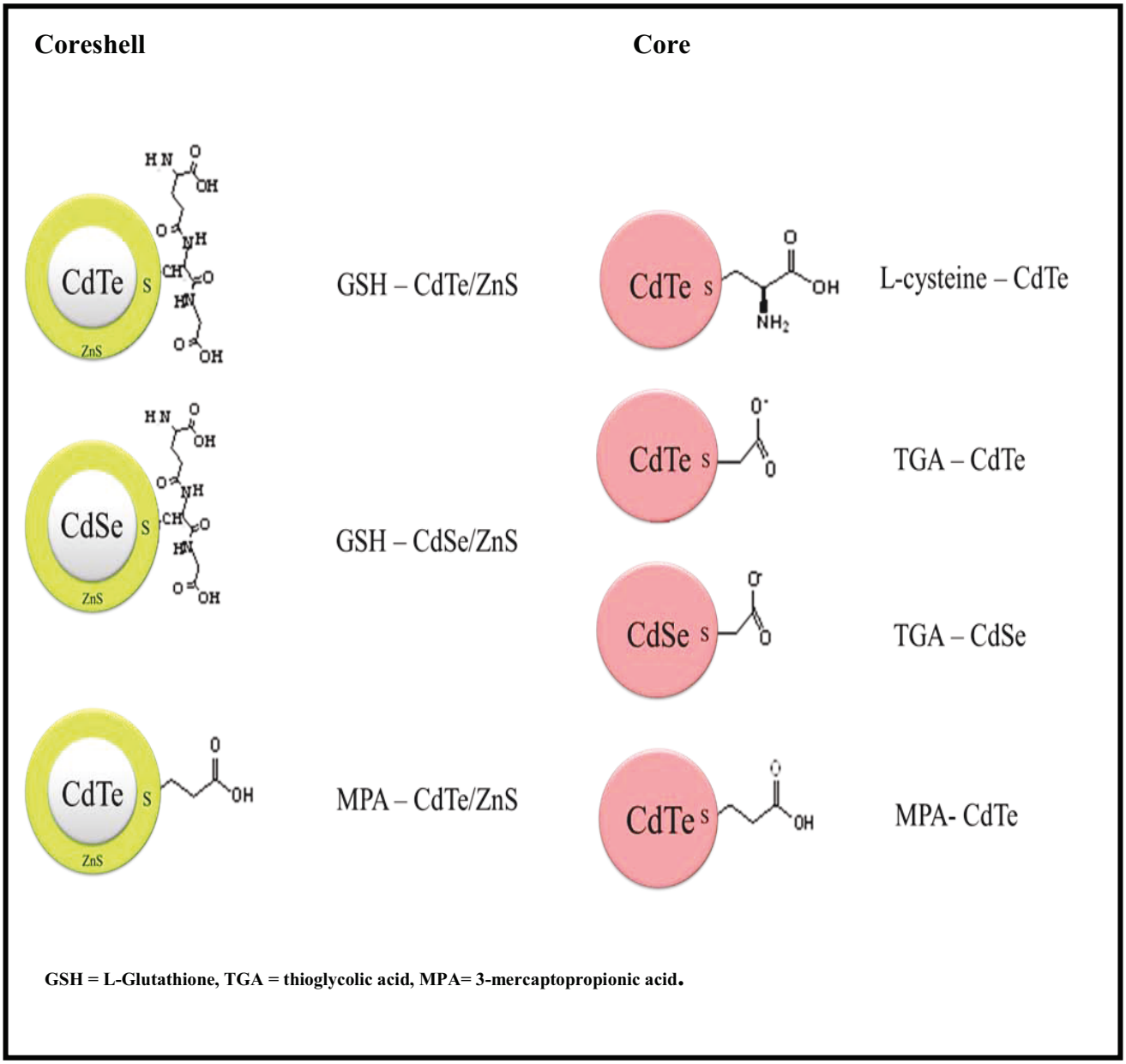

Figure 3.1: Structures and names of quantum dots.

3.1.1 XRD

X-ray diffraction patterns of $_{L}$-cysteine-CdSe and GSH-CdSe@ZnS QDs are shown in **Figure 3.2** as examples. Using XRD data, the sizes of QDs were determined using the Debye-Scherrer equation **(Equation 3.1)** [148].

$$D = \frac{0.9\,\lambda}{B\cos\theta} \qquad (\mathbf{3.1})$$

Where D is the mean diameter of the QDs in nm, λ the wavelength of the X- ray source, θ the angular position of the peak.A typical zinc blende crystal structure with planes at [111], [220], and [311] was obtained for CdSe QDs with peaks at 26.8, 44.0 and 52.1. The peaks for CdSe@ZnS QDs were at 28.6, 47.6 and 56.2. Following the growth of ZnS shells on the core CdSe, the peak position shifted to higher angles and thus, confirmed the formation of CdSe@ZnS core shell QDs. The broadening and shift of the diffraction patterns to higher angles due to the growth upon adding the shell has been reported before and is typical of the formation of the shell over the core [76, 84]. All the QDs showed similar behaviour to that shown in **Figure 3.2**.Using **Eq. (3.1)** the sizes of QDs were calculated and the values are summarized in **Table 3.1**. The size of the QDs obtained ranged between 2.0 and 3.5 nm.

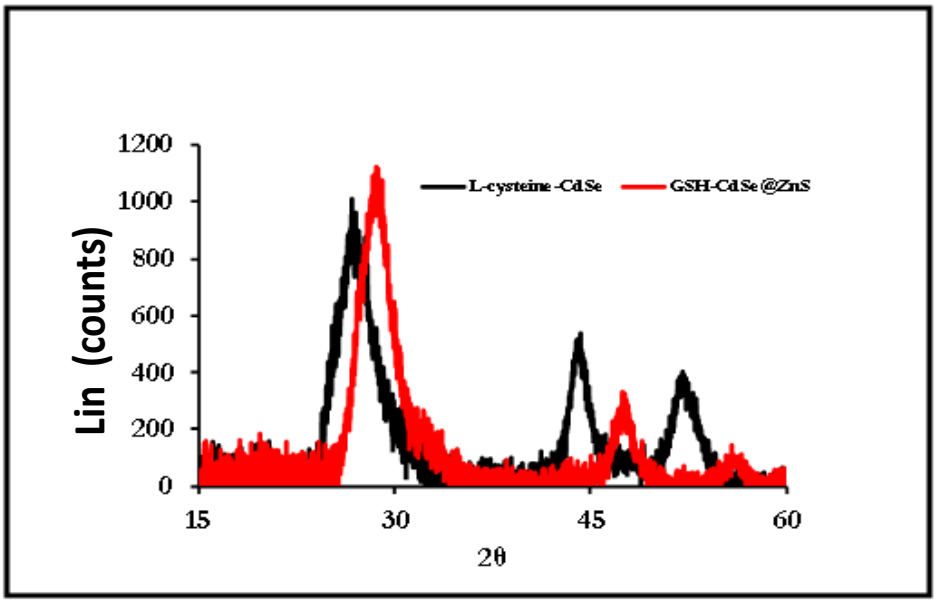

Figure 3.2: XRD spectra of the L-cysteine-CdSe and GSH-CdSe@ZnS QDs.

3.1.2. UV/vis absorption and emission spectroscopy

The absorption and emission spectra of the QDs (GSH-CdSe@ZnS used as an example) in water are shown in **Figure 3.3**. The emission maxima are shown in **Table 3.1**. All QDs exhibited broad absorption and well-resolved emission spectra. The emission maxima ranged from 539 to 633 nm, depending on the size and structure of the QDs as is typical of quantum dots [75-80]. Using Rhodamine 6G in ethanol as reference (Φ_F = 0.95) [13], fluorescence quantum yields of the synthesized QDs were calculated using **Eq. (1.1)** and the values were found to be 0.61, 0.41, 0.72, 0.47, 0.016, 0.14 and 0.44 for GSH-CdSe@ZnS, GSH-

CdTe@ZnS, MPA-CdTe@ZnS, MPA-CdTe, TGA-CdSe, TGA-CdTe and L-cysteine-CdTe, respectively **(Table 3.1).**

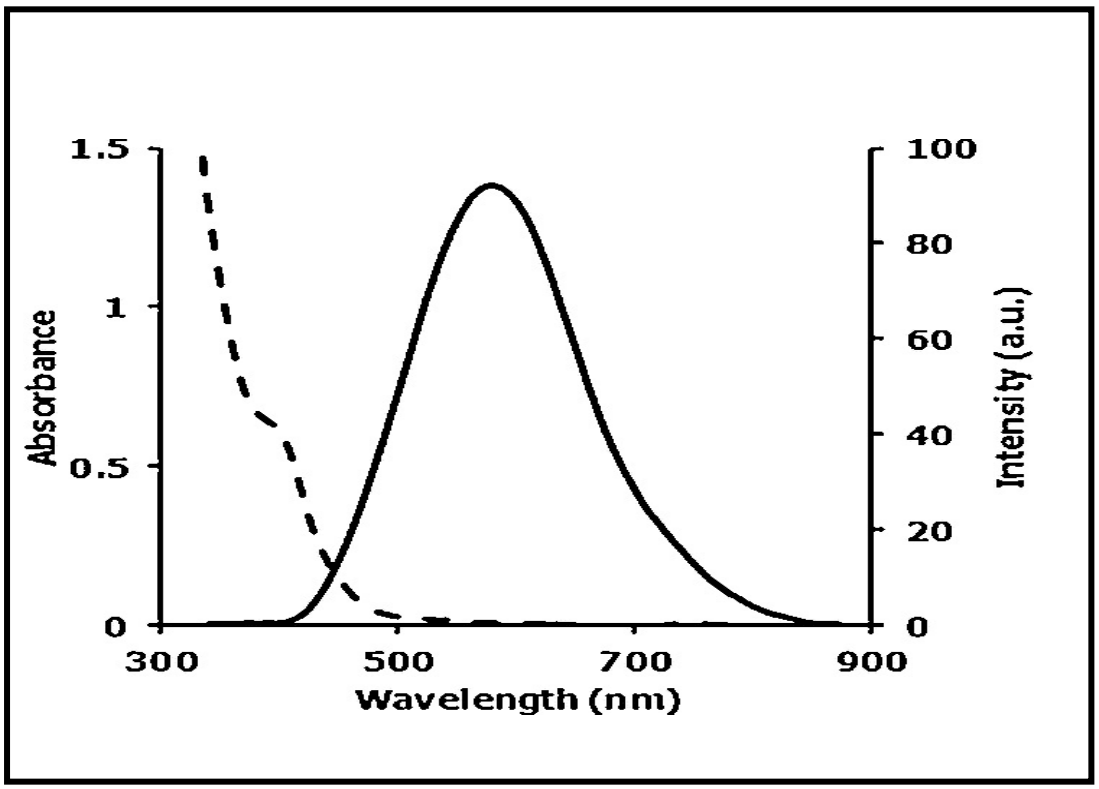

Figure 3.3: UV/vis absorption (dotted line) and fluorescence emission (spectra solid line) of GSH-CdSe@ZnS. Excitation wavelength = 300 nm.

3.1.3 Transmission electron microscopy (TEM) images

TEM was employed to study the morphology of the QDS. **Figure 3.4 (A and B)** shows the TEM images of the coreshell and core, respectively (MPA-CdTe@ZnS and MPA-CdTe used as examples). The coreshell showed some level of aggregation compared to the core alone, thus suggesting that the coreshell influences the surface morphology and size.

Table 3.1: Size, emission maxima and fluorescence quantum yields of different QDs in water.

QDs	Size, nm	λnm	Φ_F
GSH-CdSe@ZnS	2.8	580	0.61
GSH-CdTe@ZnS	3.1	600	0.41
MPA-CdTe@ZnS	3.1	557	0.72
MPA-CdTe	2.7	563	0.47
TGA-CdSe	2.0	539	0.016
TGA-CdTe	3.2	609	0.14
L-cysteine-CdTe	3.5	633	0.44

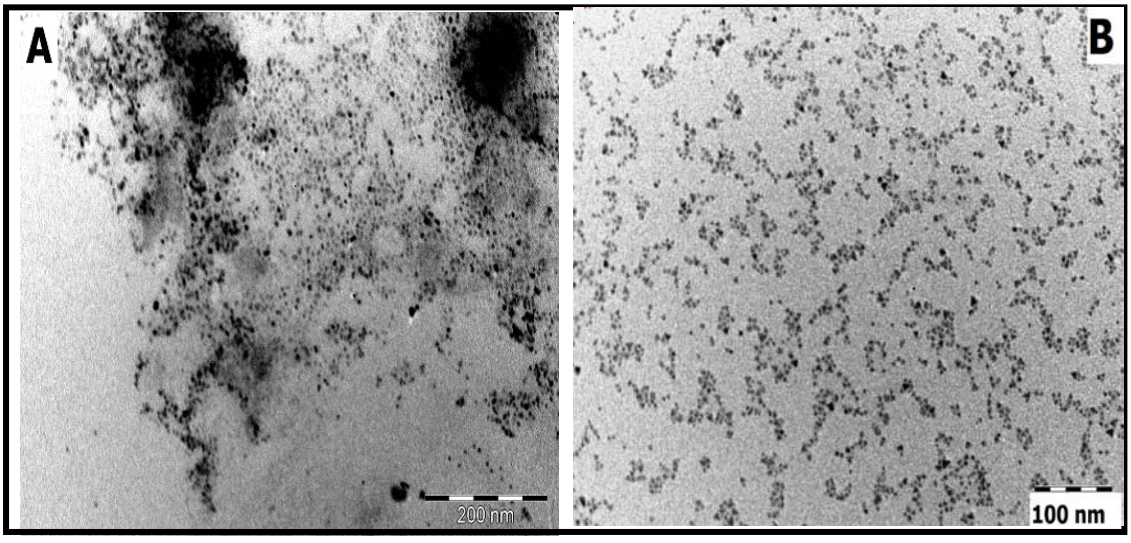

Figure 3.4: TEM images for (A) MPA-CdTe@ZnS and (B) MPA-CdTe.

3.2 Toxicity studies

3.2.1 Growth inhibitory effect of QDs

TGA-CdSe, **Figure 3.5 (b)**, GSH-CdTe@ZnS **Figure 3.5 (c)** and GSH-CdSe@ZnS **Figure 3.5 (a)** inhibited the growth of BON cells dose-dependently. MPA-CdTe@ZnS, **Figure 3.5 (d)** exhibited pronounced growth inhibitory effect, resulting in decreased cell numbers of almost 100% even at low nanomolar concentrations (20 nM). MPA-CdTe, **Figure 3.5 (d)** which was investigated as the core counterpart of MPA-CdTe@ZnS, was less toxic than the ZnS-bearing QD, but still inhibited the growth of BON cells at nanomolar concentrations. The IC_{50} (half maximal inhibitory concentration) value of MPA-CdTe was calculated to be 0.054 μM (**Figure 3.5**). TGA-CdTe and L-cysteine-CdTe QDs were not tested *in vitro* because they precipitated from the medium, which was an unexpected finding as both QDs were water soluble.

(a)

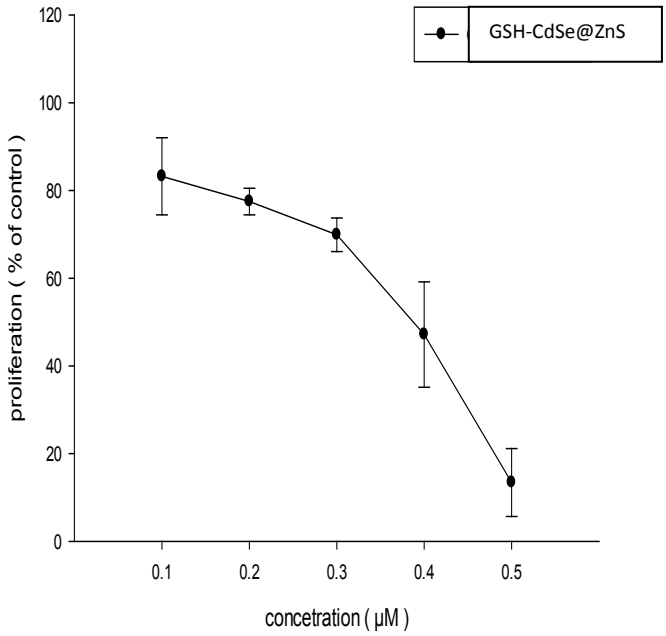
GSH-CdSe@ZnS
proliferation (% of control)
120
100
80
60
40
20
0
0.1
0.2
0.3
0.4
0.5
concetration (μM)

(b)

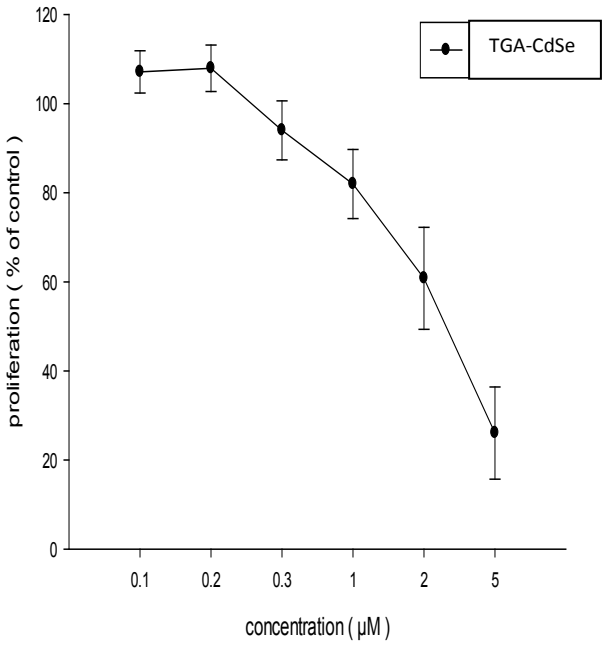
TGA-CdSe
proliferation (% of control)
120
100
80
60
40
20
0
0.1
0.2
0.3
1
2
5
concentration (μM)

(c)

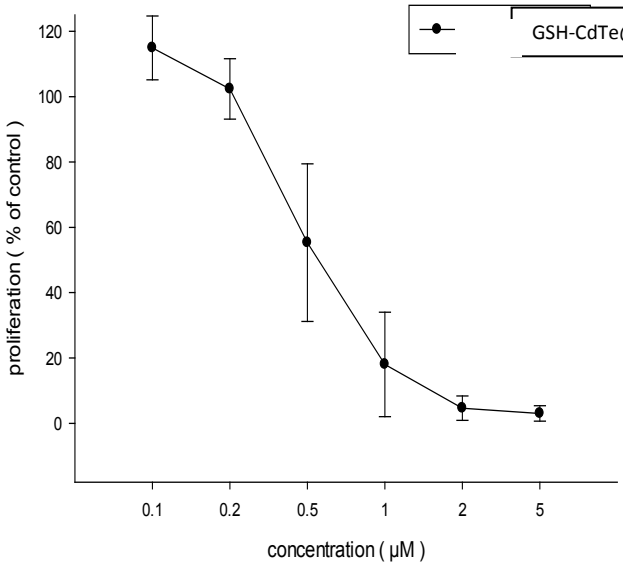
GSH-CdTe@ZnS
proliferation (% of control)
120
100
80
60
40
20
0
0.1
0.2
0.5
1
2
5
concentration (μM)

(d)

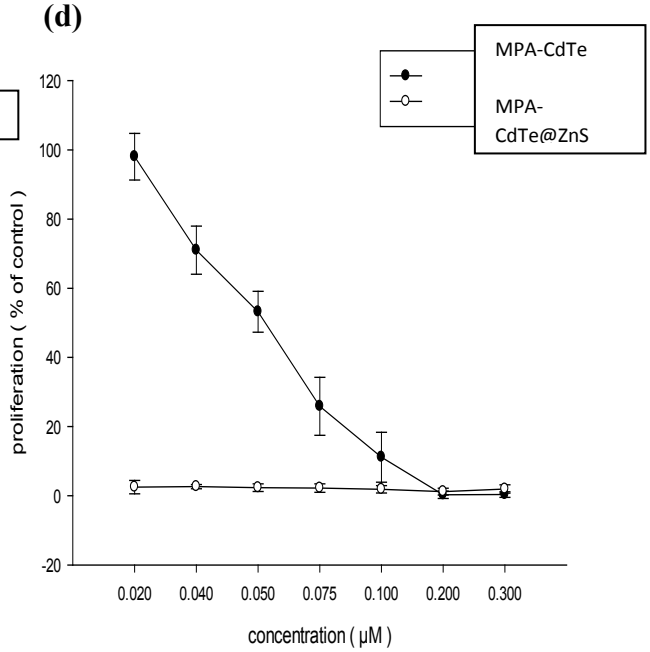
MPA-CdTe
MPA-CdTe@ZnS
proliferation (% of control)
120
100
80
60
40
20
0
-20
0.020
0.040
0.050
0.075
0.100
0.200
0.300
concentration (μM)

QD	IC_{50}
GSH – CdTe@ ZnS	0.7 µM
GSH – CdSe@ZnS	0.38 µM
TGA – CdSe	2.9 µM
MPA - CdTe	0.054 µM
MPA – CdTe@ZnS	n.d. very high dark toxicity

n.d = not determined

Figure 3.5: Determination of IC_{50} values using BON cells. Data are given as percentage of untreated controls, which were set 100% (mean ± S.D. of 3 independent experiments).IC_{50} value determined after 48 h of incubation with the respective QD.

3.2.2 Cytotoxicity of QDs

The cytotoxicity of QDs displaying no embryotoxicity was determined by measuring the release of lactase dehydrogenase (LDH) into the supernatant of BON cells. BON cells were exposed to GSH-CdSe@ZnS QDs (as an example) in concentrations ranging from 0.1 to 5 mM for 6 or 24 hrs. In BON cells treated with 0.1 and 0.2 mM of the QDs, only slight increases in LDH release (<10%) were observed, regardless of the length of incubation, **Figure 3.6**. GSH-CdSe@ZnS at 0.5 mM caused an increase in LDH release of >10% after 6 hrs and >20% after 24 hrs. At 5 mM, the release of LDH into the supernatant increased by more than 30% compared to untreated cells after 6 and 24 hrs.

The results indicated that GSH-CdSe@ZnS did not directly affect cell membrane integrity and did not have immediate cytotoxic effects in BON cells at concentrations below 0.5 mM (**Figure 3.6**). It will also be shown with chick chorioallantoic membrane (CAM) assays that the GSH-CdSe@ZnS was the least toxic *in vitro*.

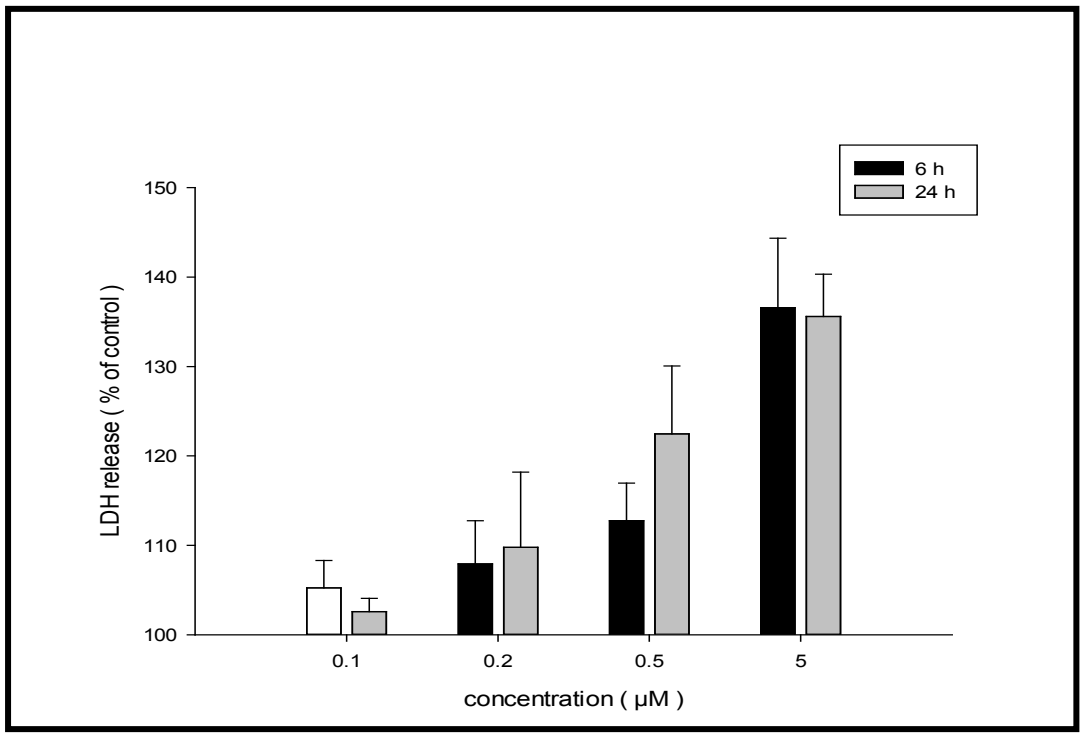

Figure 3.6: Determination of QD-induced cytotoxicity. LDH release into the supernatant of BON cells was determined after 6 and 24 hours of continuous incubation with increasing concentrations of GSH-CdSe@ZnS. Data are given as percentage of untreated controls, which were set 100 % (mean ± standard error of mean (SEM) of 3 independent experiments).

3.2.3 Cellular uptake of QDs

Incubating BON cells with GSH-CdSe@ZnS QDs (0.2 and 0.4 mM) for 4–24 hrs led to a time and dose-dependent intracellular accumulation of QDs (**Figure 3.7**). When administering 0.2 mM of GSH-CdSe@ZnS QDs, a time-dependent increase in intracellular accumulation was observed during the first 4 hrs. Higher concentrations (i.e 0.4 mM) increased the intracellular accumulation within the first 4 hrs, reflecting the dose-dependency of the QD-uptake. Increasing the incubation time to 8 and 24 hrs led to an additional increase in QD-uptake only at the concentration of 0.2 mM, whereas at 0.4 mM a slight loss of intracellular QD fluorescence was observed, (**Figure 3.7)**. Moreover, the distribution patterns changed from an even and diffuse (0.2 mM) to an uneven and more punctuate intracellular fluorescence signal at 0.4 mM. We suggest the drop of fluorescence intensity in combination with the changed intracellular distribution pattern may occur due to an accumulation of the QDs in subcellular compartments (e.g organelles, vacuoles). However, further experiments will have to determine the exact intracellular localization and distribution, since this may be of great importance for the suitability and mode of action of QD-based biomedical applications.

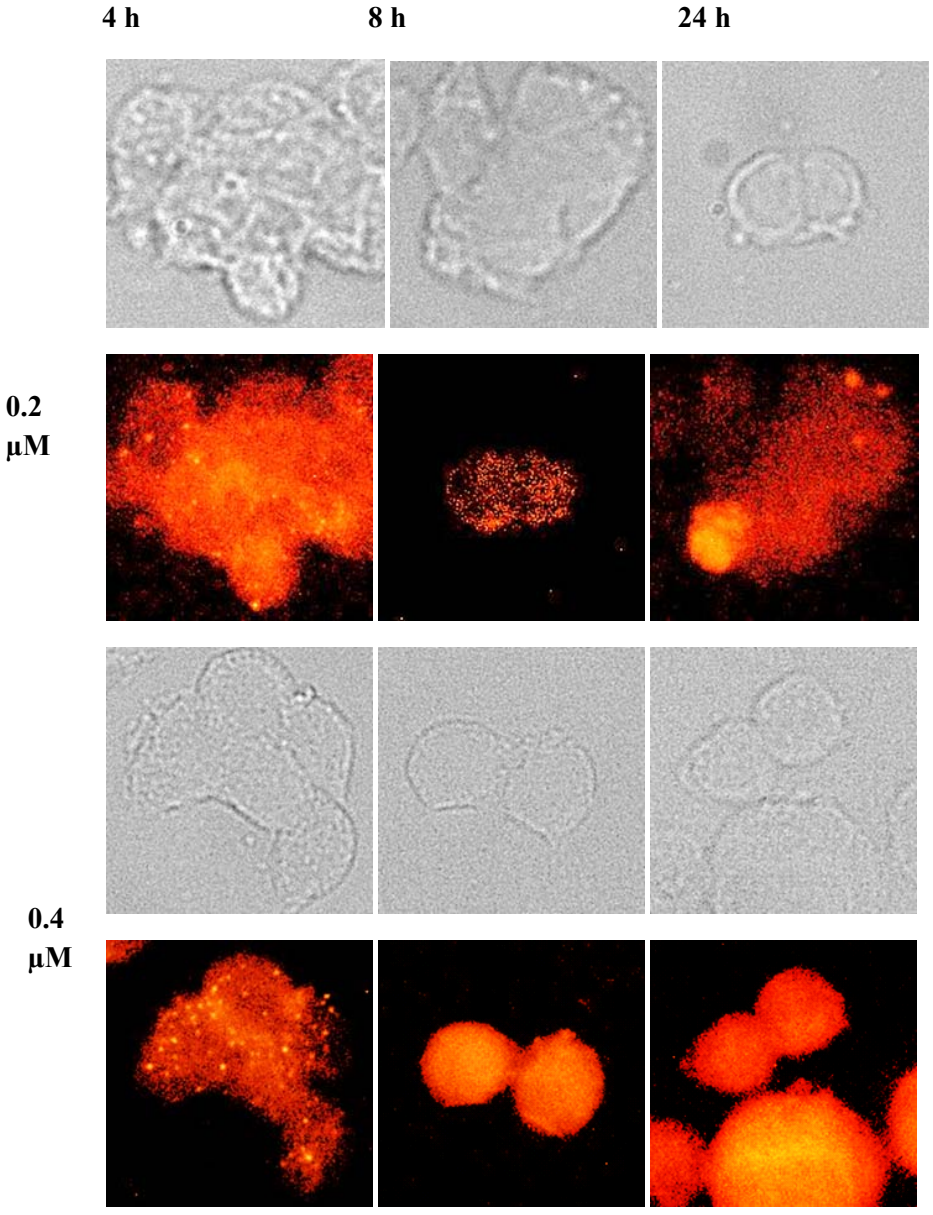

Figure 3.7: Time- and dose-dependent uptake of GSH-CdSe@ZnS QD in BON cells. QD uptake was determined by fluorescence microscopy after 4–24 hours of incubation with 0.2

mM or 0.4 mM GSH-CdSe@ZnS. Representative findings of three independent experiments with n = 10–50 cells per concentration and incubation time. Upper panel: phase-contrast images; lower panel: corresponding fluorescence micrographs.

3.2.4 Embryotoxicity

Evaluation of the toxicity of QDs *in vivo* was determined by performing chick chorioallantoic membrane (CAM) assays. QDs were either injected into the CAM-vein or applied topically to 11-days old fertilized chicken eggs. Initially, the TGA-capped CdSe QDs were investigated. Topical application of the IC_{50} (i.e 2.9 μM) led to death in 40% and 60 % was obtained when applied intravenously, (**Table 3.2**). Next, we evaluated GSH-capped QDs; GSH-CdTe@ZnS QDs applied topically at 1 μM showed no influence on embryo vitality, while administered intravenously at 0.6 μM embryo death in almost 90% was observed. Finally, GSH-CdSe@ZnS QDs neither affected the vascular network and microvessel structure of the developing CAM, nor influence chicken embryo vitality at the IC_{50} of 0.4 μM. These observations were regardless of the mode of application (i.e intravenously or topically). All chicken embryos were sacrificed at the end of the study and examined for developmental defects such as encephalic hernia or cleft beak [149]. However, no such defects were found in GSH-CdSe@ZnS QDs injected embryos (data not shown), further supporting the finding that GSH-CdSe@ZnS QDs do not cause embryotoxicity.

Table 3.2: QDs were applied topically (A) or injected (B) into the CAM-vein of 11-days old fertilized chicken eggs.

(A)

QDs	Concentration	Topical application, % of survival
TGA-CdSe	2.9 μM	60
GSH-CdTe@ZnS	1 μM	1
GSH-CdSe@ZnS	0.4 μM	100

(B)

QDs	Concentration	Injected, % of survival
TGA-CdSe	1 μM	40
GSH-CdTe@ZnS	0.6 μM	11
GSH-CdSe@ZnS	0.4 μM	100

3.2.5 Discussion

Many studies suggest ion leakage from the core of QDs, especially Cd^{2+} [150], which has become a significant problem because the cores of QDs are mostly synthesized from heavy metals. However, stable coating with a shell and capping may effectively prevent ion leakage and additionally protect the core from air oxidation [151]. In our study, we could demonstrate that GSH-CdSe@ZnS QDs were stable structurally and potentially safe for biomedical use as shown in respective *in vitro* and *in vivo* investigations.

Capping of QDs plays an important role in preventing degradation and subsequent release of cytotoxic heavy metal ions. Thus, we examined QDs with the same core and shell but with different cappings. CdTe@ZnS QDs with GSH capping (IC_{50} = 0.7 µM) showed decidedly lower cytotoxicity than those with MPA capping (very high). MPA-CdTe@ZnS QDs killed almost 100% of incubated cells even at low nanomolar concentrations (20 nM), while GSH-capped QDs (GSH-CdTe@ZnS) exhibited comparatively low cytotoxicity in BON cells, even at higher doses.

Our data are somewhat in discordance to findings reported by Lee et al. who observed that MPA-capped CdSe@ZnS QDs did not cause toxicity in living organisms even at concentration 2500 mg/l after 48 hrs of exposure to the systems [152]. As the study of Lee and co-workers employed the so called "daphnia test" to estimate QD toxicity *in vivo*, it is not surprising that the IC_{50} values determined with this method differ from those of the *in vitro* tests on human cells used in our investigation.

Compared to the direct measurement of growth inhibition and cytotoxicity in our study, the daphnia test does not directly measure cytotoxicity or death but uses the treatment-induced loss of mobility of a water-living small crustacean (*Daphnia magna*) as a read-out for the toxicity of a compound. However, the exact reasons for the discrepancy between our findings and those of Lee et al. remain to be elucidated. Nevertheless, in the context of our investigation MPA-capped CdSe-QDs were found to be too toxic to be favourable for biomedical applications and were thus excluded from further *in vivo* examinations. Changes in the core materials of QDs can have an impact on their toxicity. It has been previously been shown that not all of the QD cores were completely coated with a ZnS shell (using the one-pot synthesis also employed in this work) due to the lattice mismatch between core and shell [153]. This mismatch is estimated to be ~16%, which makes these QDs susceptible to degradation. For CdSe and ZnS, the lattice mismatch is ~12% [154], which means less degradation of the QDs will occur. As a result, CdSe@ZnS QDs should be less toxic and more stable than CdTe@ZnS QDs, as observed in this work for GSH- CdTe@ZnS and CdSe@ZnS QDs.

Additionally; we investigated QDs without shell but with TGA capping. As mentioned above, well-matched capping and proper structure of the core are very important. We found that TGA-CdSe exhibited lower cytotoxic potency than GSH-CdSe@ZnS. This is an unexpected finding, since QDs with a shell are supposed to be less toxic than those without shell [151]. It can be speculated that TGA somehow stabilized the structure of the core and prevented oxidation and/or ion leakage. However, such a hypothesis requires further examination and will be addressed in further studies. GSH-CdTe@ZnS and TGA-CdSe QDs showed marked toxicity in vivo which rejected them from further investigations.

Two other QD types (i.e L-cysteine-CdTe and TGA-CdTe) were not soluble in the experimental medium, and thus, excluded from further studies. When QDs become unstable,

they precipitate out of solution. This can be caused by the capping materials or by interactions with medium components (e.g serum, salts and proteins). It has been reported that instability of surface ligands can allow QD cores to degrade or induce air oxidation, which in turn releases cadmium ions to the environment [155].

Biocompatibilities as well as solubility are essential requirements for biological uses of QDs. A number of studies have been published that described QDs to be biocompatible and without impact on embryonic development or vitality [156]. Our *in vivo* study, also found no evidence teratogenic effects after injection with QDs. Particularly, GSH-CdSe@ZnS QDs induced no embryotoxicity, which suggests that this QD in can be safely used in biomedical research in the reported doses (i.e 0.1– 0.4 mM). Moreover, QDs have become widely used probes for *in vitro* and *in vivo* imaging as well as diagnostic agents for tumor monitoring or photodynamic therapy [157]. Here, we have shown that non-toxic concentrations of GSH-CdSe@ZnS QDs of 0.2 mM and 0.4 mM achieve sufficient cellular uptake to obtain distinct fluorescent signals (**Figure 3.7).** This suggests that in addition to their properties as a carrier of photosensitizers for PDT, GSH-CdSe@ZnS QDs may also be interesting for tumor monitoring and diagnosis.

We conclude that suitable capping and encapsulation can remarkably reduce the toxicity of QDs. CdSe QDs with ZnS shell and GSH capping appear to be promising candidates for biological uses and merit further investigations.

CHAPTER 4

This chapter presents the characterization of the phthalocyanine-quantum dot conjugates.

4. Conjugation of Pcs with QDs

4.1 Characterization

4.1.1 ClInPc(COOH)$_8$ alone

Gallium and aluminum octacarboxy phthalocyanines (ClGaPc(COOH)$_8$ and ClAlPc(COOH)$_8$) are known complexes and gave satisfactory UV-Vis , FT-IR, NMR elemental analysis and mass spectroscopy results. However, the synthesis of ClInPc(COOH)$_8$ is presented for the first time in this thesis. The spectroscopic characterization data corresponds to its structure and what has been already reported in literature for other octacarboxy phthalocyanines [143, 144]. The FT-IR data showed characteristic bands such as -OH (~3432 cm^{-1}), -C=O (~1716 cm^{-1}) and –CO (~1184 cm^{-1}) which are agreement with what has been reported [143, 144]. The ^{1}H NMR spectra of the complex showed aromatic ring protons at a region between 7.82-11.56 ppm, integrating for the 8 ring protons and 8 carboxylic acid groups protons to a total of 16 expected protons.

Figure 4.1 shows the characteristic monomeric absorption in the Q band region at 691 nm. The monomeric behavior is evidenced by a single narrow Q band typical of metallated phthalocyanine complexes. The emission spectrum (at λ = 701 nm) was a mirror image of the excitation spectrum (at λ = 691 nm) and the latter was similar to the absorption spectrum (at λ = 691 nm) **(Figure 4.1)**. Satisfactory NMR, mass spectra, elemental analysis and FT-IR data was obtained for the ClInPc(COOH)$_8$ (data not shown). **Table 4.1** shows the Q band maxima of all the Pcs used in this work. The Q band for ClInPc(COOH)$_8$ is more red shifted at 691 nm compared to the rest of the complexes in **Table 4.1** due to the large In central metal atom [158].

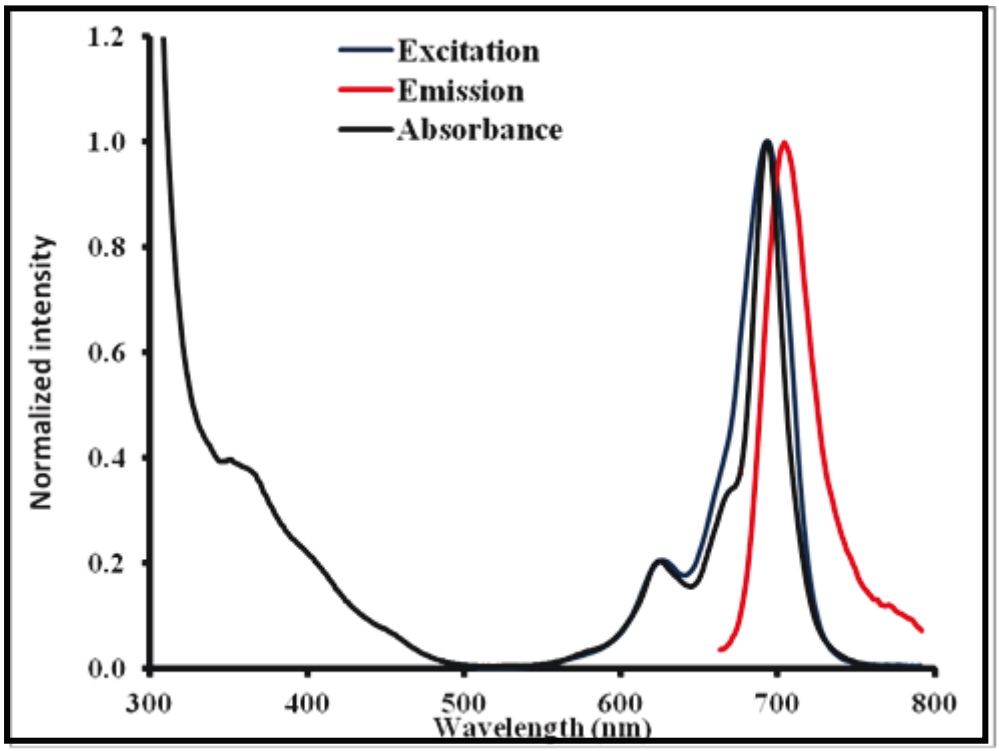

Figure 4.1: Ground state absorption, emission and excitation spectra of $ClInPc(COOH)_8$ in 0.1 M NaOH. Excitation wavelength 665 nm.

Table 4.1: The photophysical and photochemical parameters of $ClGaPc(COOH)_8$, $ClAlPc(COOH)_8$ and $ClInPc(COOH)_8$ and their conjugates in 0.1 M NaOH.

Complex/ Conjugate/	[a] $\lambda_{abs\ (Pc)}$	**Pc:QDs loading**	[a,b] $\Phi_{F(Pc)}$	[a,c] $\Phi_{F(QDs}$	[a] $\Phi_{T(Pc)}$	[a] $\tau_{F(Pc)}$ (± 0.01) (ns)	[d] $\tau_{F(QDs)}$ (± 0.01)	[a] $\tau_{F(QDs, Av)}$	[a] $\tau_{T(Pc)}$ (µs)
$ClGaPc(COOH)_8$-GSH-CdSe$^{(2.3\ nm)\#}$	688 (688)	1:6	0.18 (0.21)	0.23 (0.34)	0.63 (0.58)	4.3 (3.9)	31.5 (47 %) 6.6 (21%) 0.8 (32%)	16.5 (13.0)	118 (72)
$ClGaPc(COOH)_8$-GSH-CdSe@ZnS$^{(3.0\ nm)\#}$	690 (688)	1:3	0.12 (0.21)	0.14 (0.47)	0.70 (0.58)	4.1 (3.9)	33.7 (53%) 4.6 (22%) 0.5 (25%)	19.0 (9.6)	136 (72)
$ClGaPc(COOH)_8$-GSH-CdSe@ZnS$^{(3.5\ nm)\#}$	690 (688)	1:1	0.07 (0.21)	0.11 (0.59)	0.69 (0.58)	4.0 (3.9)	35.2 (43.9%) 6.4 (30%) 0.3 (36.1 %)	17.5 (16.8)	134 (72)
$ClAlPc(COOH)_8$-GSH-CdSe@ZnS$^{(3.5\ nm)\#}$	689 (689)	1:1	0.15 (0.23)	0.18 (0.59)	0.68 (0.53)	3.9 (3.7)	36 (46.3%) 6.9 (15%) 0. 9 (46.8 %)	17.2 (9.6)	144 (83)
$ClInPc(COOH)_8$-GSH-CdSe@ZnS$^{(3.0\ nm)\#}$	693 (691)	1:3	0.09 (0.13)	0.25 (0.47)	0.56 (0.49)	3.3 (3.4)	29.3(29%) 3.7(36%) 0.4 (35%)	18.4 (16.8)	169 (67)

[a] Value in brackets = Pc alone or QDs alone

[b] Excitation at 665 nm

[c] Excitation at 480 nm and for the conjugates, $\Phi_{F(QDs)} = \Phi_{F(QD)}^{conjugate}$

[d] Relative abundance in brackets and excitation of QDs

 # QDs mean diameter

4.1.2 QDs alone

A different batch of QDs of different sizes were synthesized and employed in this chapter, this was not the same batch used in **Chapter 3** and hence re-characterization of the QDs was necessary. Having established in **Chapter 3** that GSH capped CdSe QDs with ZnS shell showed less toxicity, we continued the work presented in this thesis using GSH-CdSe@ZnS QDs, comparing with core GSH-CdSe QDs. One GSH-CdSe and two GSH-CdSe@ZnS QDs were synthesized.

4.1.2.1 XRD

The X-ray diffraction pattern of the core GSH-CdSe and coreshell GSH-CdSe@ZnS obtained is similar to **Figure 3.2.** The sizes for core GSH-CdSe was 2.3 nm and for the two GSH-CdSe@ZnS QDs the sizes were 3.0 nm and 3.5 nm represented as GSH-CdSe$^{(2.3.nm)}$**,** GSH-CdSe@ZnS$^{(3.0nm)}$ and GSH-CdSe@ZnS$^{(3.5nm)}$ respectively, **Table 4.2.**

4.1.2.2 Emission spectra

In **Figure 4.2** the core GSH-CdSe displayed an emission peak at 586 nm and after capping the core with ZnS the emission peak was observed at 629 nm for GSH-CdSe@ZnS$^{(3.0nm)}$, 681 nm for GSH-CdSe@ZnS$^{(3.5nm)}$.

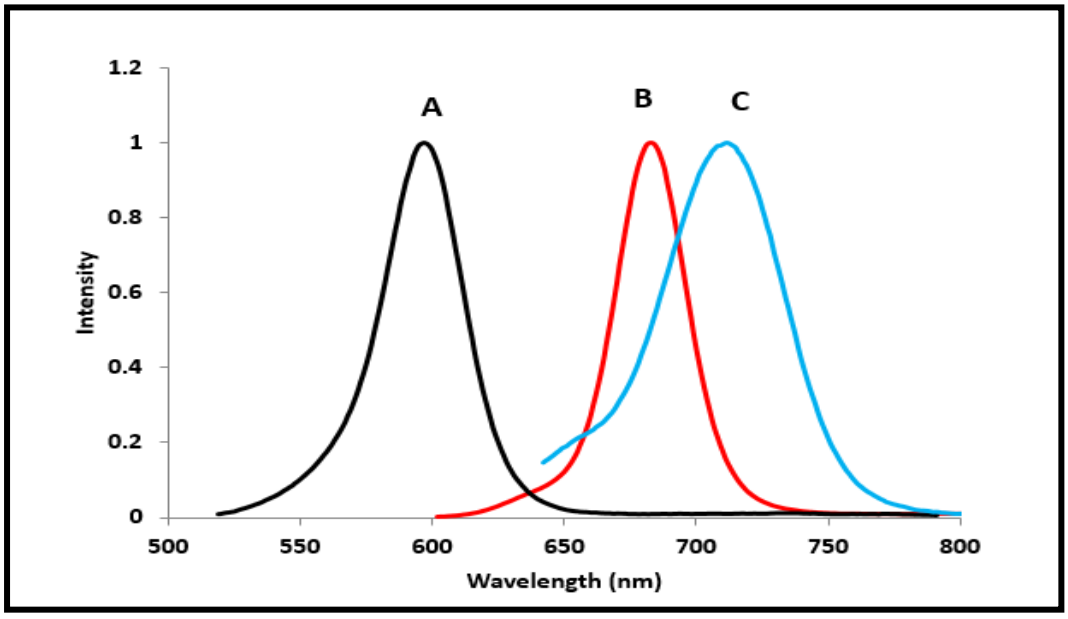

Figure 4.2: Emission spectra of core (a) GSH-CdSe (2.3 nm) core shell (b) GSH-CdSe@ZnS 1 (3.0 nm) and (c) GSH-CdSe@ZnS 2 (3.5 nm). Excitation wavelength = 480 nm.

4.1.2.3 Microscopic data

Transmission electron microscopy (TEM) was used to study the morphology of the core GSH-CdSe and the different sizes of core shell quantum dots GSH-CdSe@ZnS$^{(3.0nm)}$ and GSH-CdSe@ZnS$^{(3.5nm)}$. In **Figure 4.3 (a)** an image of core GSH-CdSe is shown, they are small in size estimated at 2 nm; **Figure 4.3 (b)** shows the increase in size upon the capping with the ZnS shell. The sizes are 3.3 nm and 3.6 nm for the core shell quantum dots GSH-CdSe@ZnS$^{(3.0nm)}$ and GSH-CdSe@ZnS$^{(3.5nm)}$ which is in agreement and not too far off with what was obtained from the XRD patterns for GSH-CdSe@ZnS.

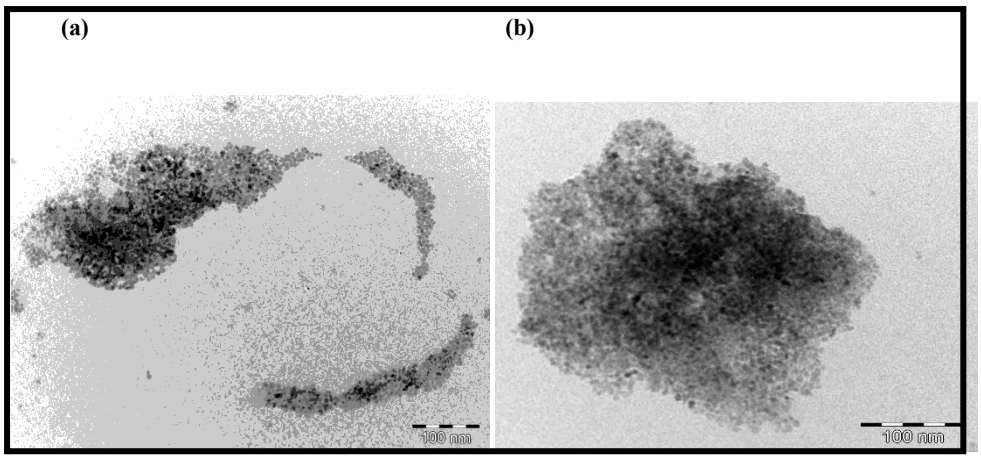

Figure 4.3: TEM images of (a) core GSH-CdSe alone (b)core shell GSH-CdSe@ZnS$^{(3.0\ nm)}$.

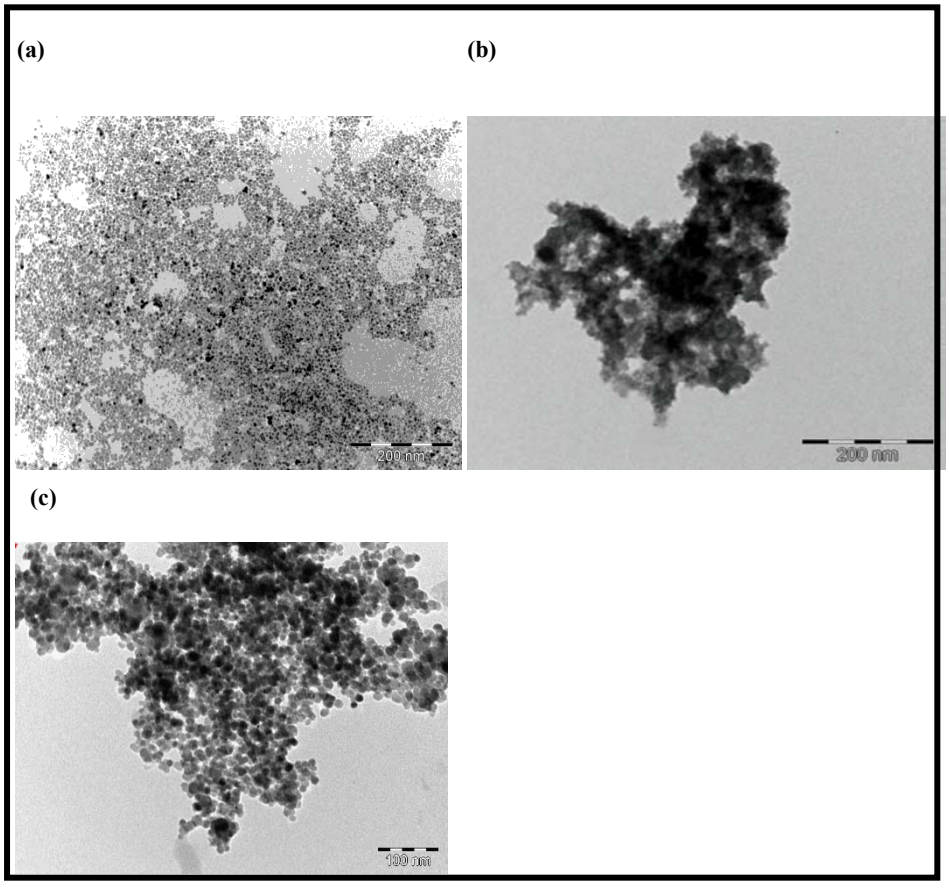

Figure 4.4: TEM images of:(a) GSH-CdSe@ZnS$^{(3.5\ nm)}$ QDs alone (b) CdSe@ZnS $^{(3.5\ nm)}$-ClGaPc(COOH)$_8$ and (c) CdSe@ZnS$^{(3.0\ nm)}$-ClInPc(COOH)$_8$.

Table 4.2: Sizes of various QDs used in this work, excitation wavelength 480 nm.

QDs	Pc conjugated to	λ_{emm}	XRD size	$\Phi_{F(QDs)}$	$\tau_{F(QDs)}$ (± 0.01)	$\tau_{F(QDs),Av}$
GSH-CdSe$^{(2.3\ nm)}$	ClGaPc(COOH)$_8$	586	2. 3 nm	0.34	24.8 (48%) 6.2 (12%) 0.9(40%)	13.0
GSH-CdSe @ZnS$^{(3.0\ nm)}$	ClGaPc(COOH)$_8$	629	3.0 nm	0.47	26.9 (31%) 4.3 (24 %) 0.6(45%)	9.6
	ClInPc(COOH)$_8$	634		0.48	27.9 (24%) 6.8 (31%) 0.6 (45%)	
GSH-CdSe @ZnS$^{(3.5\ nm)}$	ClAlPc(COOH)$_8$	681	3.5 nm	0.59	27.6 (56%) 9.6 (13%) 0.4 (31%)	16.8
	ClAlPc(COOH)$_8$	610		0.43	27.1 (58%) 6.7 (11.3%) 0.6 (30.7%)	16.6

4.1.3 Characterization of conjugates of quantum dots with with Pcs

Schemes 4.1 (A) and (B) show the formation of GSH-CdSe-ClGaPc$(COOH)_8$ andGSH-CdSe@ZnS-ClGaPc$(COOH)_8$ conjugates, respectively, by linking the carboxyl group of the metal octacarboxy phthalocyanine to the amino group on either the GSH capped core or coreshell QDs.**Scheme 4.1 B** shows the linking of GSH-CdSe $^{(3.5\ nm)}$ to ClInPc$(COOH)_8$ and ClAlPc$(COOH)_8$

The conjugates are represented as ClGaPc$(COOH)_8$-GSH-CdSe$^{(2.3\ nm)}$ for the core and ClGaPc$(COOH)_8$-GSH-CdSe@ZnS$^{(3.0\ nm)}$ or ClGaPc$(COOH)_8$-GSH-CdSe@ZnS$^{(3.5\ nm)}$ for the core shell conjugates of different sizes in **Tables 4.2**.

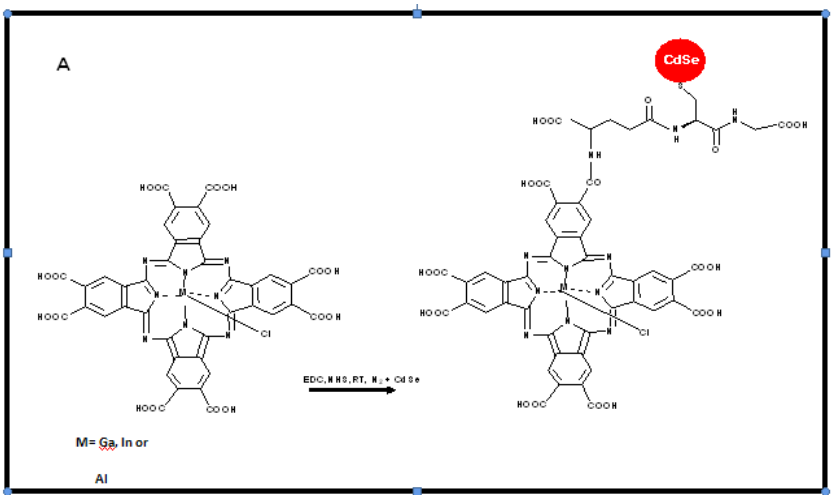

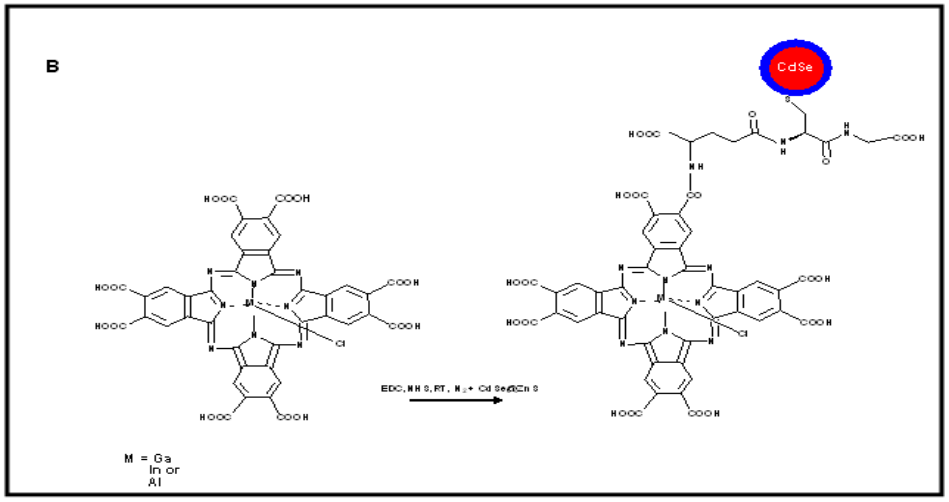

Scheme 4.1: Schematic representation of the conjugation of Pcs ($ClInPc(COOH)_8$, $ClGaPc(COOH)_8$ or $ClAlPc(COOH)_8$) to either **(a)** GSH-CdSe or **(b)** GSH-CdSe@ZnS QDs.

In this work the number of Pcs bonded to QDs was determined following literature method as described in literature [159] however using absorption instead of fluorescence. The ratios obtained were: GSH-CdSe: ClGaPc(COOH)$_8$ (1:6), GSH-CdSe@ZnS$^{(3.0nm)}$:ClGaPc(COOH)$_8$ (1:3) and GSH-CdSe@ZnS$^{(3.5\ nm)}$:ClGaPc(COOH)$_8$ (1:1). We observe a decrease in the number of Pc bonded to the QDs as the size of QDs increased. In **Table 4.2** ClGaPc(COOH)$_8$ were coordinated to GSH-CdSe or GSH-CdSe@ZnS to check the effects of core and coreshells. ClGaPc(COOH)$_8$ was also coordinated to different sizes to check the effects of size.

4.1.3.1 Microscopic data

Upon conjugating the ClGaPc(COOH)$_8$ to the QDs aggregation was observed as seen for the ClGaPc(COOH)$_8$$^{(3.5\ nm)}$-GSH-CdSe@ZnS conjugate in **Figure 4.4 (b)**, thus making estimation of individual particle size impossible**.** The same tendency to aggregate upon conjugation with ClGaPc(COOH)$_8$ was observed for all the conjugates (TEM images of the other two conjugates not shown). **Figure 4.4 (c)** shows the CdSe@ZnS$^{(3.0\ nm)}$-ClInPc(COOH)$_8$ conjugate. The particle size of the conjugate increased to 9 nm, an increase from QDs alone at 3.0 nm. This is probably due to the aggregation of the Pc in the presence of QDs also discussed above for ClGaPc(COOH)$_8$.

4.1.3.2 FT-IR Spectra

FT-IR was employed to further characterize the complexes and to also confirm the formation of the amide bond. With the GSH-CdSe QDs **(Figure 4.5 (b)** we observe a COO- stretching band at 1667 cm^{-1} and the corresponding –OH band is found at 3300 cm^{-1}. In **Figure 4.5 (c)** a C=O vibration of the $ClGaPc(COOH)_8$ is observed at 1653 cm^{-1}. Formation of characteristic amide bands at 1648 cm^{-1} and 3256 cm^{-1} confirm the success of the linkage **Figure 4.5 (a)**. Such bands were absent for the QDs alone **Figure 4.5 (b)** or for the $ClGaPc(COOH)_8$ alone in **Figure 4.5 (a).** It is known that a shift in FT-IR band confirms structural change [159], as was observed in this work. Similar changes were observed for all the other conjugates and for $ClInPc(COOH)_8$ and $ClAlPc(COOH)_8$ (spectra not shown).

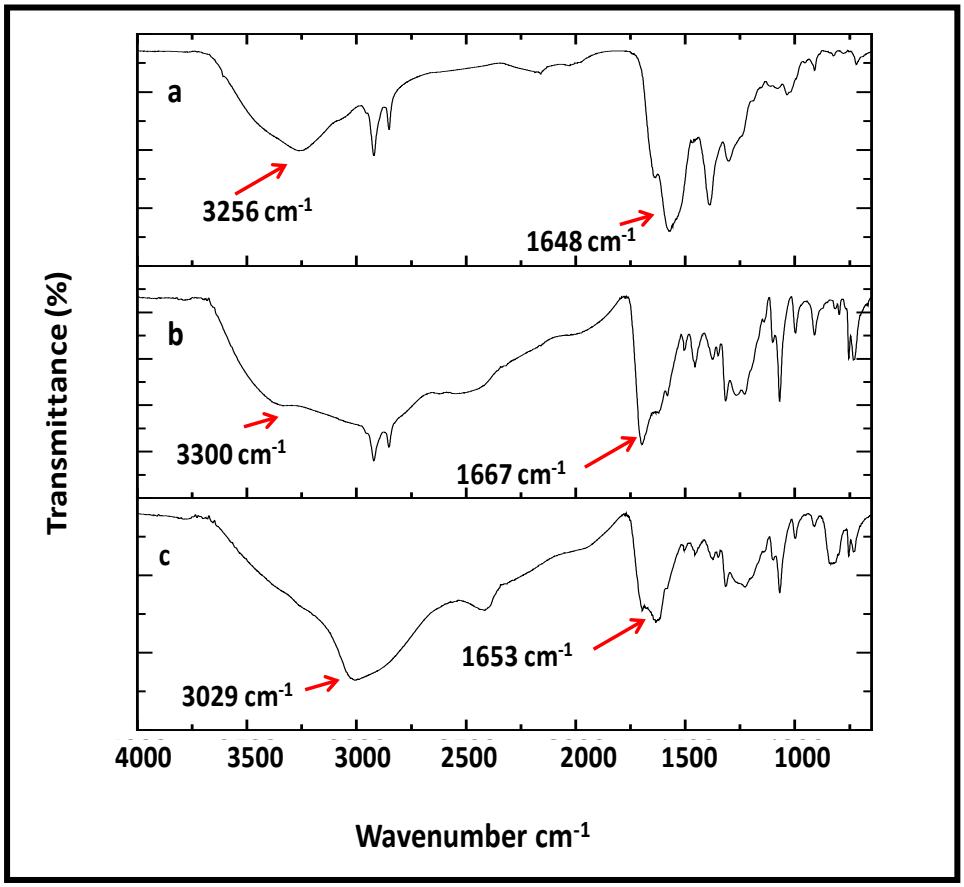

Figure 4.5: FT-IR spectra of (a)ClGaPc(COOH)$_8$-GSH-CdSe$^{(2.3\ nm)}$ conjugate, (b) GSH-CdSe$^{(2.3\ nm)}$ and (c) ClGaPc(COOH)$_8$.

4.1.3.3 Thermogravimetric analysis (TGA)

TGA thermograms for ClInPc(COOH)$_8$ before conjugation and after conjugation with QDs are shown in **Figure 4.6**. Curve (ii) shows that the ClInPc(COOH)$_8$ decomposes faster than QDs conjugates, but is still fairly stable as it only loses 12 % of the weight percentage. Conjugating QDs (curve (i)) to the ClInPc(COOH)$_8$ improved the stability with the weight loss being 1.2 % for the Pc-QDs conjugate. The stability of the conjugates is as a result of thermally stable QDs. This confirms that the addition of QDs enhances the stability of the complex.

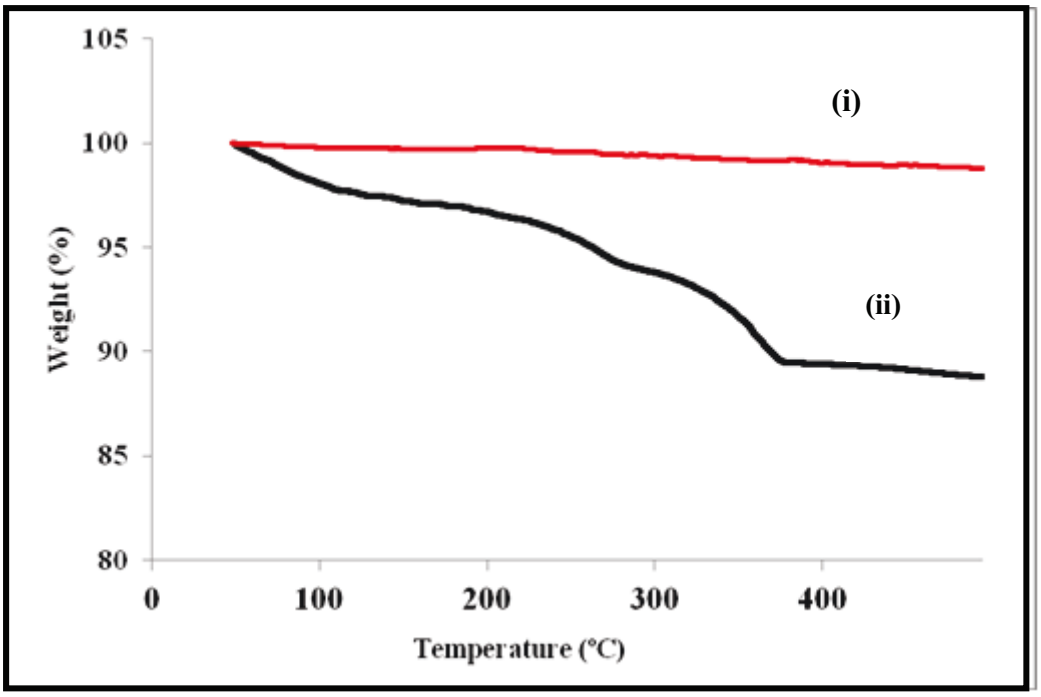

Figure 4.6: TGA curves of the (i) Pc-QDs(ClInPc(COOH)$_8$-QDs) conjugate and (ii) the Pc alone (ClInPc(COOH)$_8$).

4.1.3.4 UV/vis absorption spectra of conjugates

The absorption spectrum of $ClGaPc(COOH)_8$ in NaOH (0.1 M), **Figure 4.7 A(c)** shows a Q-band absorption at 688 nm, (**Table 4.1)**. No change in the Q-band maximum was observed when core GSH-CdSe QDs were introduced **Figure 4.7 A(a)**. The addition of QDs resulted in an increased absorption from around the 600 nm region, due to QDs absorption. A small 2 nm shift of the Q band from 688 nm to 690 nm upon the introduction of the both core shell QDs was observed (**Table 4.1**). The small shift is attributed to the change in environment when the QDs were introduced. For $ClInPc(COOH)_8$ and conjugates when QDs are introduced, the Q-band of Pc shifts from 691 nm to 693 nm, **Table 4.1, Figure 4.7 B**. No shift in Q band of $ClAlPc(COOH)_8$ was observed when QDs were introduced.

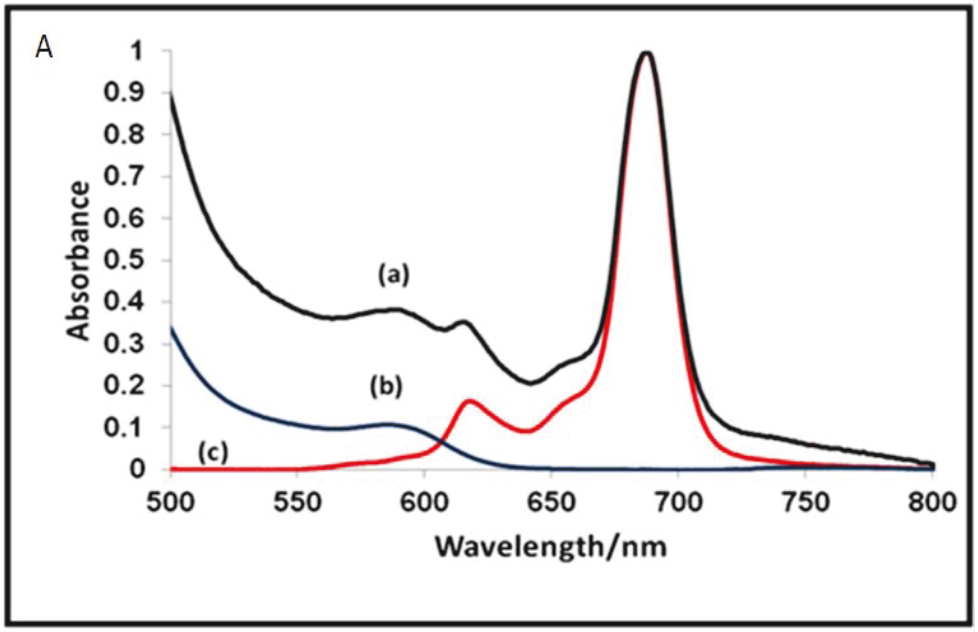

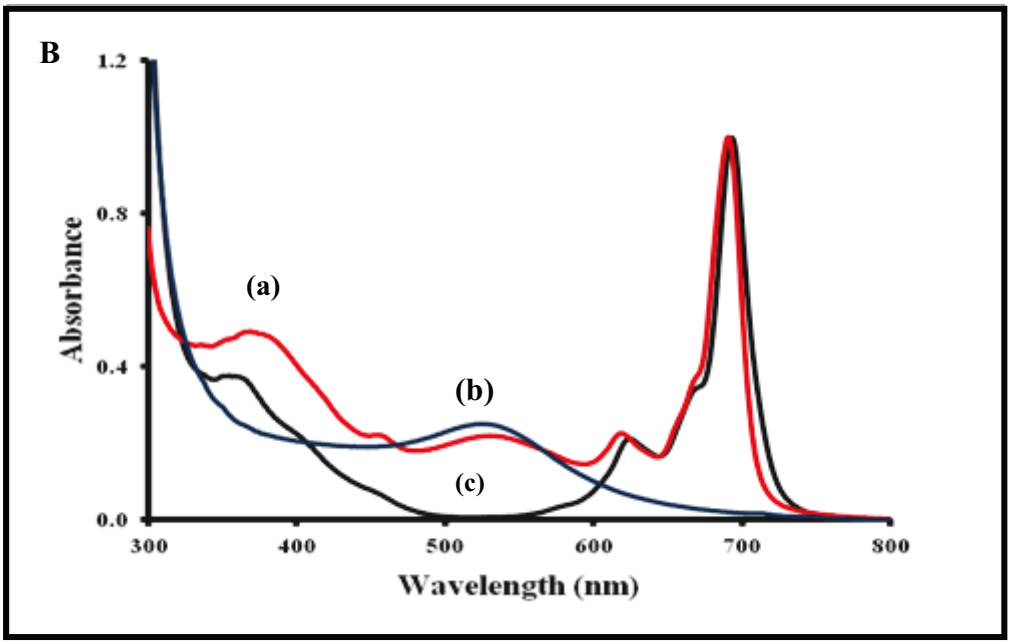

Figure 4.7: (A) Ground state absorption spectra of (a) $ClGaPc(COOH)_8$-GSH-CdSe conjugate, (b) GSH-CdSe alone and (c) $ClGaPc(COOH)_8$ alone. **(B)** (a) $ClGaPc(COOH)_8$-GSH-CdSe@$ZnS^{(3.0nm)}$, (b) GSH-CdSe@$ZnS^{(3.0nm)}$ and (c) $ClGaPc(COOH)_8$ alone, in 0.1 M NaOH.

4.2 Photophysical behaviour

4.2.1 Fluorescence quantum yield (Φ_F) and lifetimes (τ_F)

The fluorescence quantum yields of the QDs increase with an increase in the size of the quantum dots (**Table 4.2**).We have reported an increase in Φ_F with increase in QDs size, depending on the capping agent [137**].** The shell is also expected to protect the core hence resulting in improved Φ_F values.

When linking QDs to $ClGaPc(COOH)_8$ the fluorescence quantum yield $\Phi_{F(pc)}$ of $ClGaPc(COOH)_8$ decreased from 0.21 (for Pc alone) to 0.18, 0.12 and 0.07 (for $ClGaPc(COOH)_8$-GSH-CdSe and $ClGaPc(COOH)_8$-CdSe@$ZnS^{(3.0nm)}$ and $ClGaPc(COOH)_8$-CdSe@$ZnS^{(3.5nm)}$ conjugates respectively), when the excitation wavelength is where Pc absorbs and there is minimal absorption by the QDs (**Table 4.1**). The decrease in fluorescence quantum yield is as a result of the heavy atom effect of the QDs which enhances intersystem crossing (ISC) to the triplet state. For $ClInPc(COOH)_8$ Φ_F decreases from 0.13 to 0.09 and for $ClAlPc(COOH)_8$ from 0.23 to 0.15. The largest decrease in Φ_F values when exciting where Pcs absorb, is observed for the larger QDs which have more heavy atoms hence a more enhanced ISC. The fluorescence quantum yield of QDs in the conjugate (InPc-QDs), from Φ_F = 0.48 for QDs alone to Φ_F = 0.25 for the conjugate, **Table 4.1.** When excited where QDs absorb and Pcs do not, a decrease in the fluorescence quantum yields of the QDs $\Phi_{F(QDs)}$ is observed in **Table 4.1.** The decrease is due to FRET and other processes which deactivate the excited states of the QDs [160-162].

The fluorescence quantum yield of the ClInPc(COOH)$_8$ alone is low, compared to the other Pcs due to the enhancement of intersystem crossing by the presence of the heavier indium atom. Enhanced ISC results in increased triplet quantum yields as will be discussed below. For QDs alone, it has been reported in literature [163] that increase or decrease in Φ_F values of QDs in the presence of Pcs depended on size, capping agents and hence most likely on the surface defects.

Fitting of the luminescence decay curves for the QDs and the Pc-QDs conjugates (when excited where QDs absorb) resulted in three lifetimes ($\tau_{F(QDs)}$) as is typical of QDs [158,159,162], **Figure 4.8**. For the same reason given for the Φ_F values, the core shell showed longer lifetimes compared to core (see averaged lifetimes, **Table 4.1**). There is an increase in the average lifetimes ($\tau_{F(QDs)}$) in the presence of the Pc. A single lifetime ($\tau_{F(Pc)}$) was obtained when exciting where the Pc absorb, for all Pcs and their QDs conjugates, **Table 4.1**. There is a slight increase in $\tau_{F(Pc)}$ in the presence of QDs, except for ClInPc(COOH)$_8$. The increase could be due to partial protection of the Pc by the QDs.

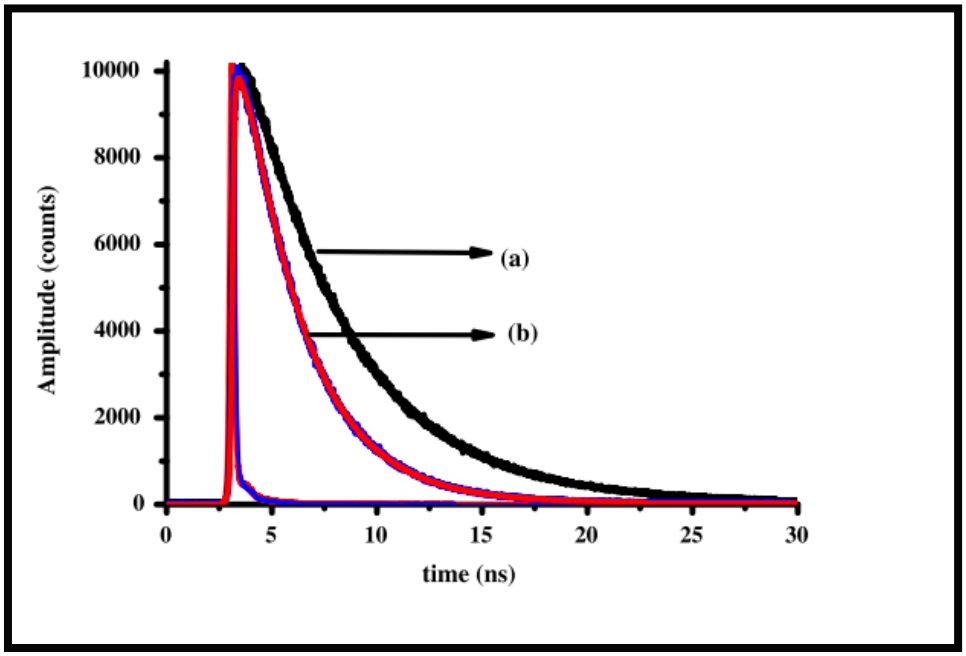

Figure 4.8: Fluorescence decay curve of (a) GSH-CdSe@ZnS QDs and (b) GSH-CdSe@ZnS QDs-ClGaPc(COOH)$_8$ conjugate in 0.1 M NaOH.

4.2.2 Triplet Quantum yields (Φ_T) and lifetimes (τ_T)

Typical triplet decay curve for the ClGaPc(COOH)$_8$ alone is shown in **Figure 4.9** obeyed first order kinetics. We expect the $\Phi_{T(Pc)}$ values of the Pcs to increase in the presence of the QDs as a result of the heavy atom effect which will encourage ISC, as is observed in **Table 4.1**.The Φ_T of the conjugates are higher than for Pcs alone. An increase in triplet lifetimes of Pcs in the presence of QDs is also observed in **Table 4.1**. We have observed the increase in triplet lifetimes of phthalocyanines in the presence of QDs in literature before [78]. The increase in the triplet lifetimes could be attributed to the protection of the Pcs by the nanoparticles.

The $\Phi_{T(Pc)}$ and $\tau_{T(Pc)}$ values for ClGaPc(COOH)$_8$-GSH-CdSe@ZnS$^{(3.0nm)}$ and ClGaPc(COOH)$_8$-GSH-CdSe@ZnS$^{(3.5nm)}$ are similar, showing that the size of the core shell does not have much influence on the triplet state parameters.

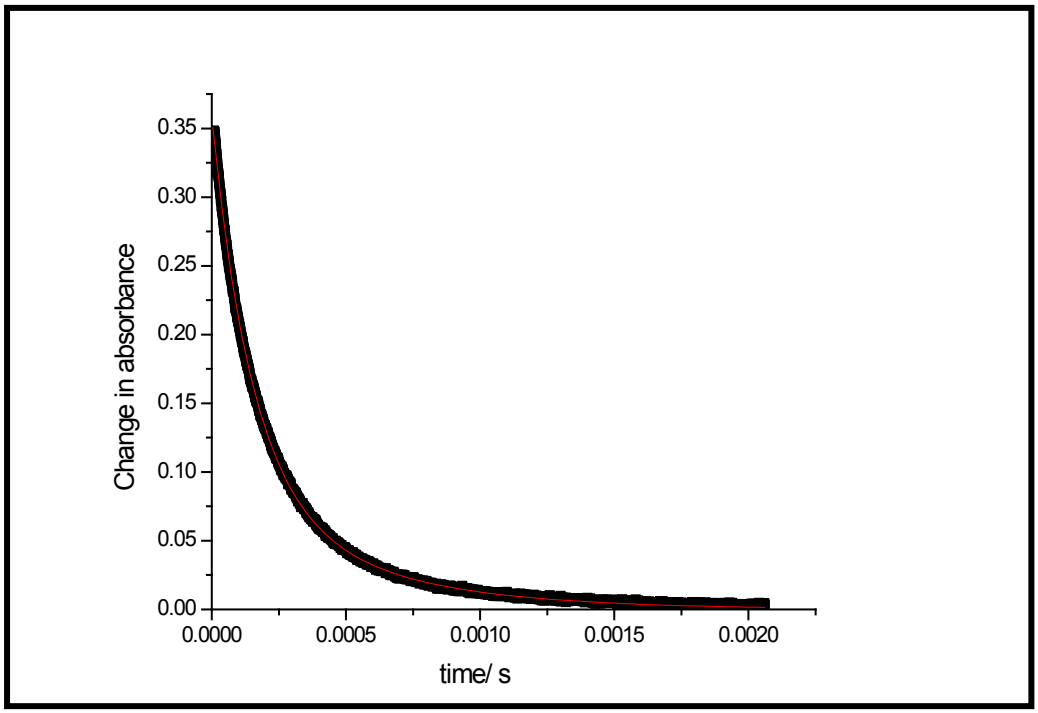

Figure 4.9: Triplet Decay profile of ClGaPc(COOH)$_8$ in 0.1 M NaOH.

4.3 Förster Resonance Energy Transfer (FRET) studies

A good spectral overlap between the fluorescence emissions of the various QDs with the absorption spectrum of Pc is an important requirement in FRET studies, and the overlap is observed in **Figure 4.10**.

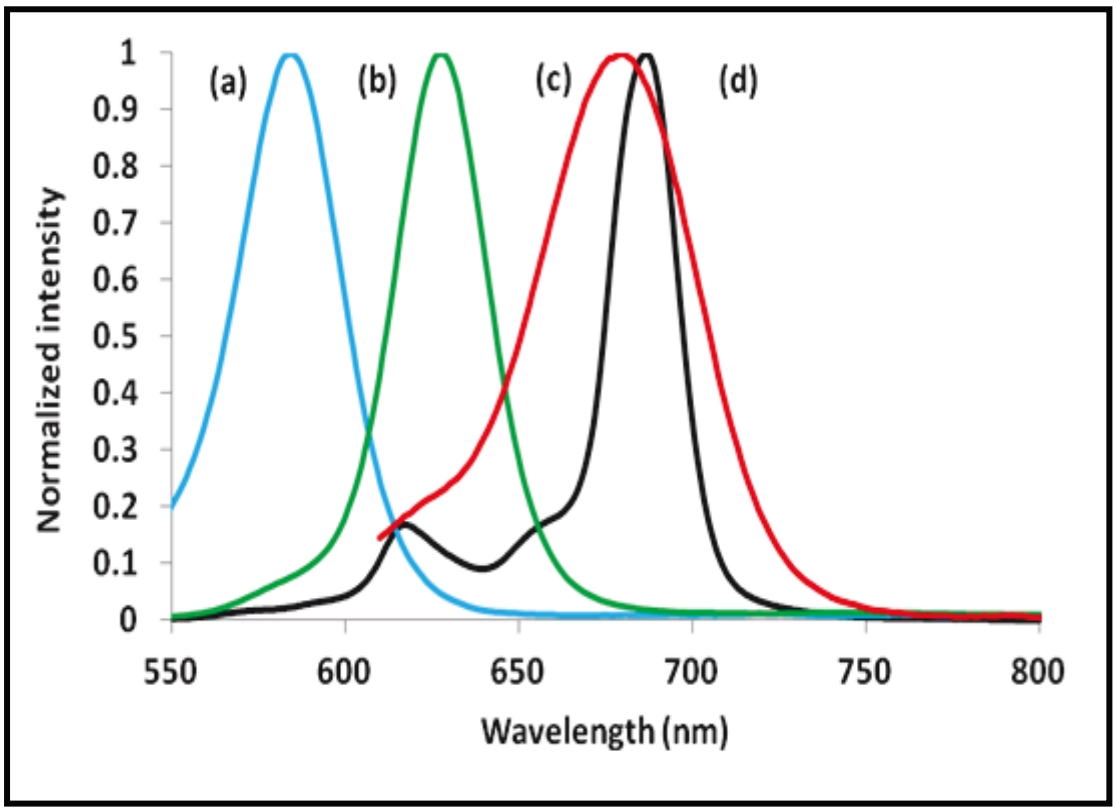

Figure 4.10: Emission spectra of core (a) GSH-CdSe, (b) GSH-CdSe@ZnS$^{(3.0nm)}$ and (c) GSH-CdSe@ZnS$^{(3.5nm)}$ and (d) absorption spectra of ClGaPc(COOH)$_8$ in 0.1 M NaOH.

For all the conjugates, the excitation was carried at 520 nm where QDs absorb but the phthalocyanine does not absorb. FRET between ClInPc(COOH)$_8$ and the various sized QDs was verified by a decrease in the photoemmision of the donor (the various QDs).

The largest overlap is observed for the larger core shell QDs. A drastic decrease in the emission intensity of the QDs in the conjugates is observed. Weak stimulated emission peaks was observed in **Figure 4.11** for the ClInPc(COOH)$_8$-QDs, a similar trend was observed for all the conjugates. The weakness in stimulated emission may either be due to weak fluorescence by Pc containing Ga or In central metal or the fact that the decrease in QDs fluorescence is not only due to FRET since there are other processes which deactivate the excited states of the QDs in addition to FRET [162].

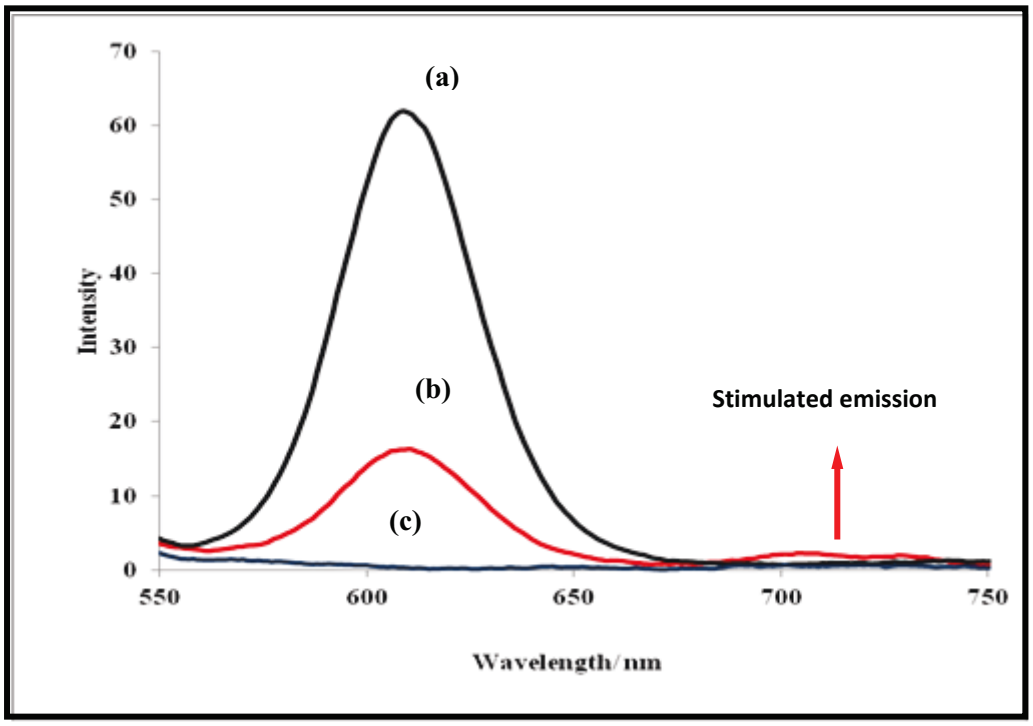

Figure 4.11: Fluorescence emission spectra of (a)GSH-CdSe@ZnS QDs alone (ii)ClInPc(COOH)$_8$-GSH-CdSe@ZnS, (iii) ClInPc (COOH)$_8$ alone in 0.1 M NaOH.

Table 4.2: Forster Resonance Energy Transfer (FRET) parameters of the conjugates in NaOH (0.1 M).

Compound	J (x 10^{-13})	R_0 (x 10^{-10})	r (x 10^{-10})	*Eff*
ClGaPc(COOH)$_8$-GSH-CdSe	5.89	48.2	42.4	0.76
ClGaPc(COOH)$_8$-GSH-CdSe@ZnS (3.0 nm)	6.54	44.3	40.9	0.86
ClGaPc(COOH)$_8$-GSH-CdSe@ZnS (3.5 nm)	6.64	43.8	41.2	0.78
ClAlPc(COOH)$_8$-GSH-CdSe@ZnS (3.5 nm)	6.34	44.6	42.1	0.75
ClInPc(COOH)$_8$-GSH-CdSe@ZnS (3.0 nm)	6.56	45.4	41.0	0.79

FRET parameters were estimated from the decrease in the QDs emission and are summarized in **Table 4.2.** The J values obtained in this work were relatively high and were of the order 10^{-13}. For porphyrin-based complexes, J values are generally of the order of 10^{-14} cm^6 [163], showing a good overlap for the conjugate in this work. The value of r was less than the values of R_0 for the conjugates; hence the *Eff* values are all greater than 50% for all conjugates. As expected, the J values were large for the larger QDs conjugates, however we noted that $ClGaPc(COOH)_8$-GSH-CdSe@$ZnS^{(3.0\ nm)}$ showed the highest *Eff* value of 0.86. This corresponds to the small value of r suggesting that the$ClGaPc(COOH)_8$ is in closest proximity to the donor (GSH-CdSe@$ZnS^{(3.0nm)}$) compared to the other conjugates and thus there should be an ease of energy transfer (*Eff*) between the excited GSH-CdSe@$ZnS^{(3.0nm)}$ and the $ClGaPc(COOH)_8$.

4.4 Photodynamic therapy application

4.4.1 PDT on human carcinoid BON cells

As proof of concept, we conjugated an aluminum octacarboxyphthalocyanine to the GSH-CdSe@ZnS QDs and applied PDT and imaging on human pancreatic carcinoid BON cells. Aluminum was the choice of central metal for the octacarboxyphthalocyanine in this specific part of the study. This was selected as there are number aluminum pthalocyanine derivatives currently undergoing clinical trials [164-168], however none of those aluminum pthalocyanines currently in clinical trials are conjugated to QDs, hence it was the aim of this work.

The effects of GSH-CdSe@ZnS$^{(3.5nm)}$-ClAlPc(COOH)$_8$ conjugate on the growth of human pancreatic carcinoid BON cells were studied by crystal violet staining as described in section 2.4.2 [146]. One of the requirements of an excellent or an ideal photosensitizer is that it should not exhibit any dark toxicity, meaning it should only destroy cancerous cells when exposed to a light of specific wavelength.

In **Figure 4.12** the concentration of the conjugates used were; 4 μM, 3 μM, 2 μM, 1 μM and 0.5 μM at 10 J/cm^2. No dark toxicity in the cells was observed, as made evident by the cells continuous growth in the medium when placed in the dark. A dosage dependant cell death (**Figure 4.12**) trend was also observed on irradiation, meaning the drugs were more efficient at higher concentrations, resulting in an increased cell death at higher concentration of the conjugate compared to the lower concentrations. At the highest concentration (4 μM) the conjugates were effective in killing only 36.9 % of the cells, while killing only 19.5 % at the lowest concentration (0.5 μM).

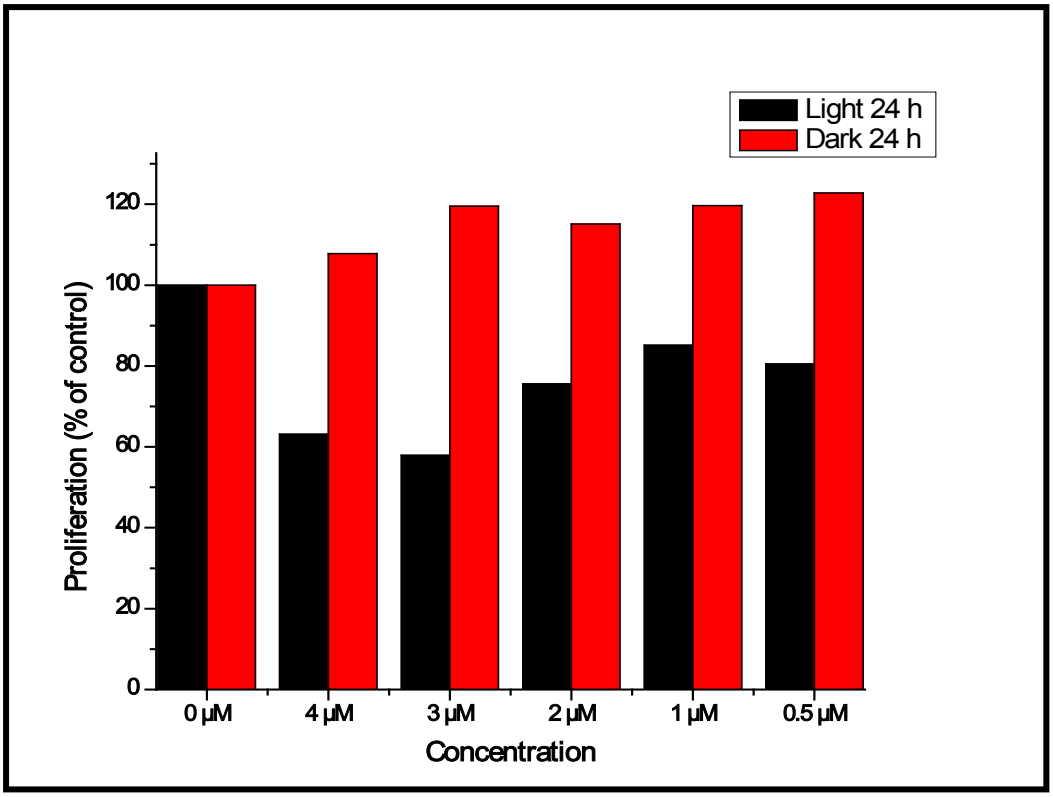

Figure 4.12: Effect of GSH-CdSe@ZnS$^{(3.5nm)}$-ClAlPc(COOH)$_8$ conjugate on the cell survival of BON cells 24 hours after illumination at 10 J/cm^2.

To increase the effectiveness of the conjugates, we increased our concentration range to; 10 µM, 5 µM, 4 µM, 2 µM and 1 µM and also increased the energy to 20 J/cm^2. The cells were monitored for 24, 48 and 72 hrs after irradiating with light. Upon increasing the energy and the concentration (**Figure 4.13 A**), it was observed after 24 hrs that at the highest concentration (10 µM) the conjugates were effective in killing 77.9 % of the cells, **Figure 4.13 A.**

However, the conjugates became toxic as they also managed to kill off 80.3% of the cells in the dark. At the second highest concentration (5 μM) 66.5 % of the cells were killed, we still observed dark toxicity with 13.9% of the cells killed in the dark **Figure 4.13 A**, From 4 μM and at lower concentrations (2 μM and 1 μM) no dark toxicity was observed and 70 % of the cells were killed at 4 μM and 60% and 50% at 2 μM and 1 μM respectively. A dosage dependent trend was also observed after 24 hrs of irradiation.

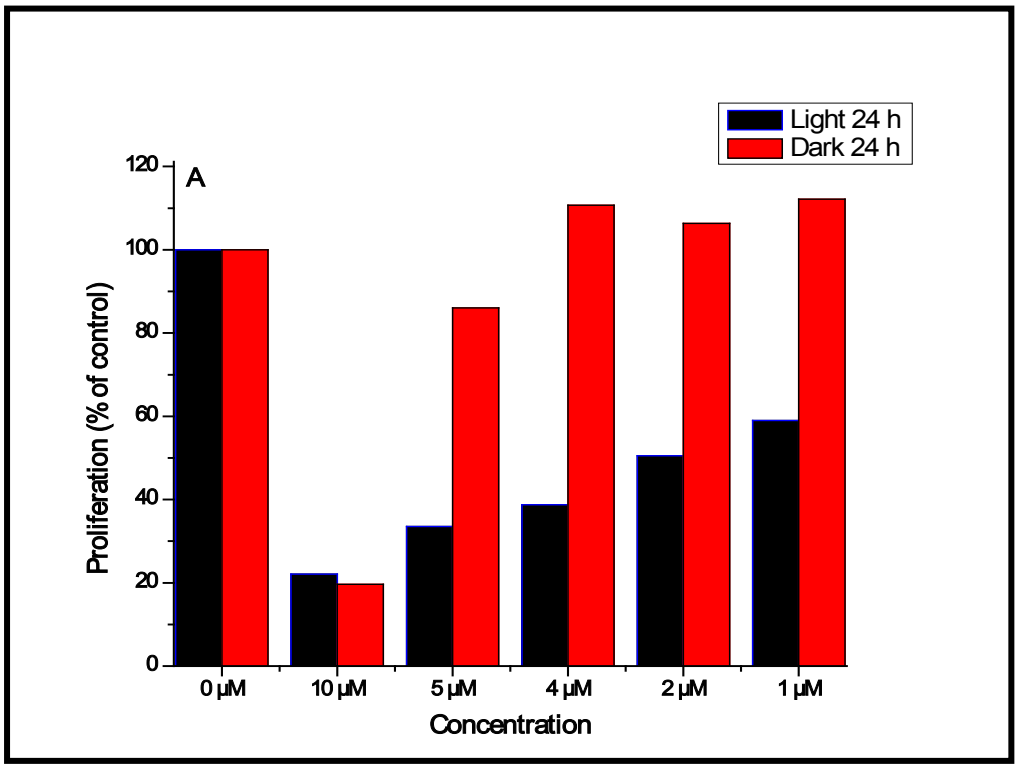
A
Light 24 h
Dark 24 h
Proliferation (% of control)
120
100
80
60
40
20
0
0 µM
10 µM
5 µM
4 µM
2 µM
1 µM
Concentration

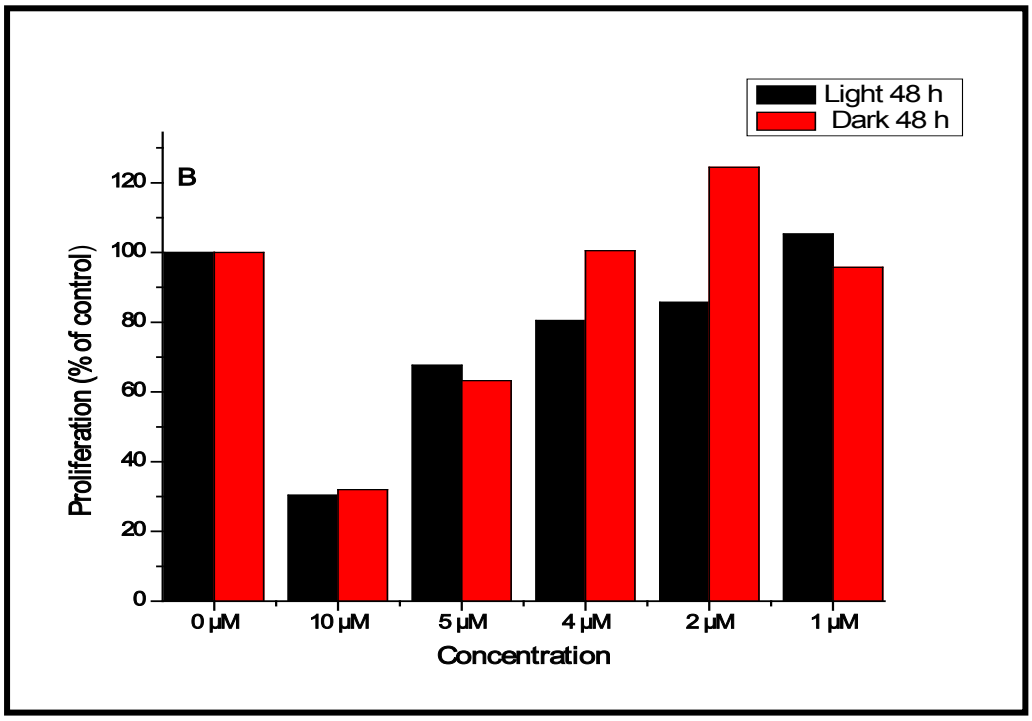
B
Light 48 h
Dark 48 h
Proliferation (% of control)
120
100
80
60
40
20
0
0 µM
10 µM
5 µM
4 µM
2 µM
1 µM
Concentration

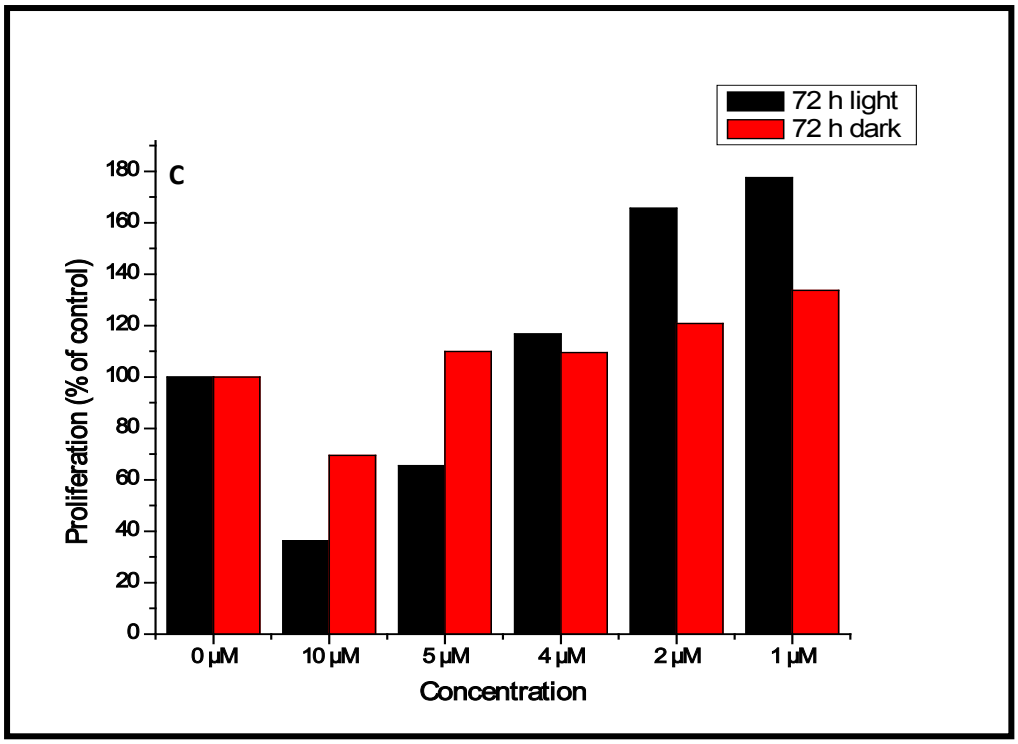

Figure 4.13: Effect of GSH-CdSe@ZnS$^{(3.5nm)}$-ClAlPc(COOH)$_8$ conjugation cell survival of BON cells at (A) 24 hrs, (B) 48 hrs and (C) 72 hours after illumination at 20 J/cm^2.

After 48 hrs of illumination **(Figure 4.13 B)** we noted a tendency of the cells starting to re-grow. At the highest concentration at 10 µM the cells did not grow back however the compounds were still toxic in the dark. At 5 µM, the second highest concentration there was a reduction in cell death with 32% and 40 % of the cells in the light and dark respectively. While at 4 µM the conjugates were effective in killing 60 % of the cells in the light and no dark toxicity observed, **Figure 4.13 B**. After 72 hrs (**Figure 4.13 C**) all the cells had re-grown except at 10 µM concentration, which remains toxic.

As seen from the above results the cancerous cells start growing back after a few days, we propose the following explanation; QDs by themselves are able to photo-produce free radicals under a high-dose irradiation, resulting in a slight cell damaging. Although a large

percentage of the cells were killed, it is known that the cancerous cells multiply at faster rates than ordinary cells, so the few remaining cells had multiplied after a few days. Alternatively the capping agent used for our QDs (GSH) is a known antioxidant which could be the result of cells re-growing after a few days (as it will hinder the production of the radicals responsible for cell death). Another possible reason could be instability of QDs in the medium or surface irregularities.

4.4.2 Fluorescence imaging

To determine the effectiveness of our QDs in imaging applications we employed a fluorescence microscope, we used two different concentrations 2 μM and 4 μM. **Figure 4.14 A** is the control (a) shows our cells under normal light and (b) shows the fluorescence, we do not expect to see any fluorescence in our control as we do not have any QDs that fluoresce**.** **Figure 4.14 B and C** show fluorescence images when using 2 μM and 4 μM of QDs, we are able to see the fluorescence and the images are much clearer at the highest concentration. The fluorescence property of the QDs will allow use in PDT and imaging applications.

(A)

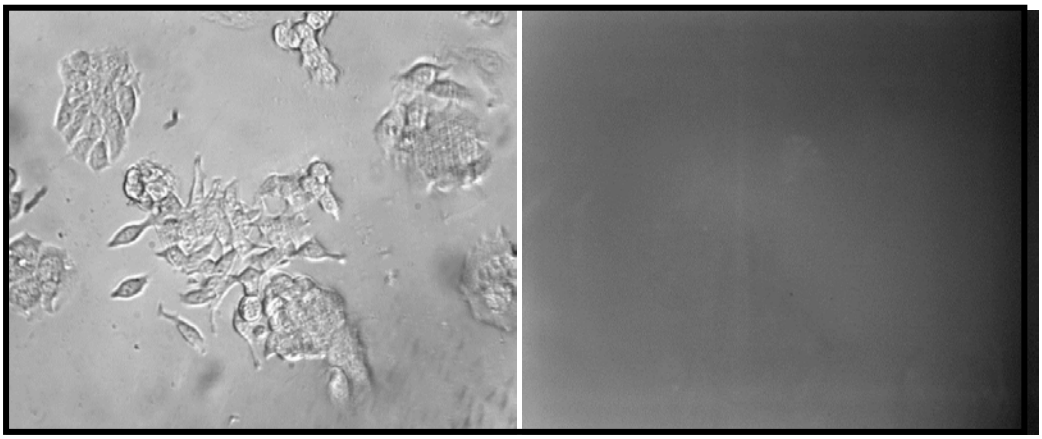

(B)

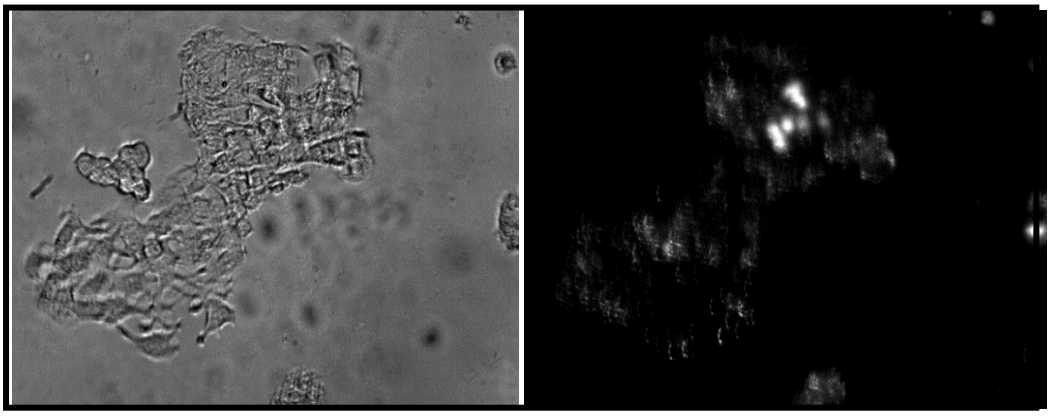

(C)

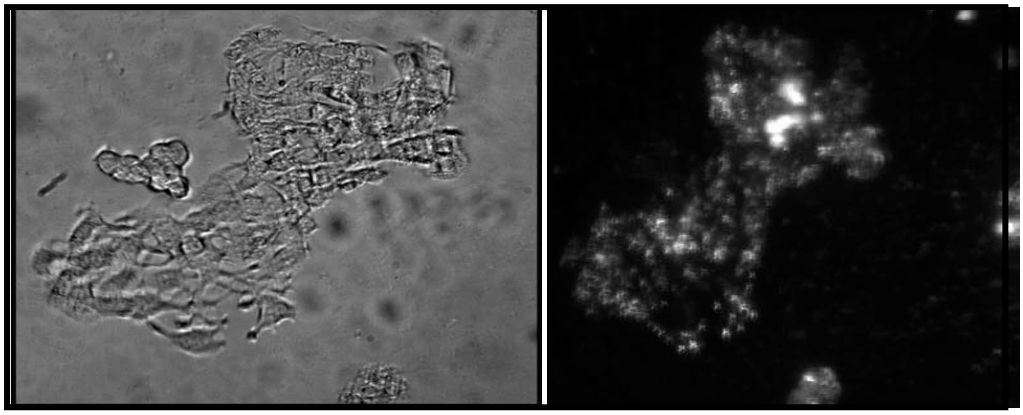

Figure 4.14: Human carcinoid BON cells under normal light and under fluorescence of (A) control, (B) 2 μM QDs and (C) 4 μM QDs.

CHAPTER 5

This chapter provides results on quantum dots-magnetic nanoparticles – phthalocyanine conjugates

5.1 Characterization of ClInPc(COOH)$_8$-MNPs conjugate

5.1.1 Uv/vis spectra

Scheme 5.1 shows the conjugation of amino functionalized Fe_3O_4 magnetic nanoparticles to ClInPc(COOH)$_8$. **Figure 5.1** compares the absorption spectrum of (a) ClInPc(COOH)$_8$ with that of (b) amino functionalized Fe_3O_4 magnetic nanoparticles and (c) ClInPc(COOH)$_8$ - Fe_3O_4 MNPs conjugate in 0.1 M NaOH. Amino functionalized Fe_3O_4 magnetic nanoparticles show a broad absorption at ~380 nm. ClInPc(COOH)$_8$ absorbs at 691 nm upon introducing the amino functionalized Fe_3O_4 magnetic nanoparticles, no change in the Q-band position is observed and is still at 691 nm **Table 5.1**.

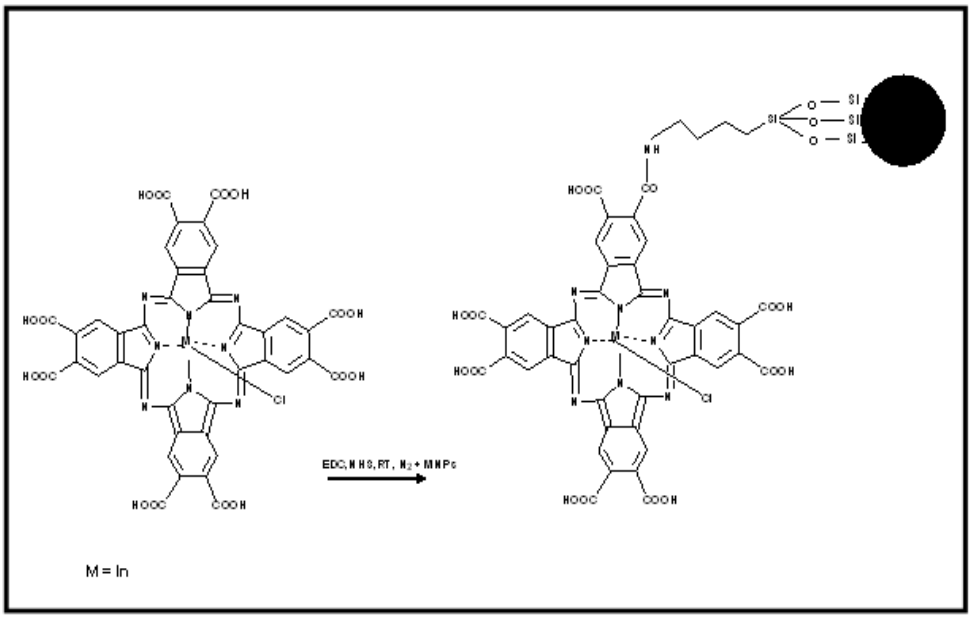

Scheme 5.1: Schematic representation of the conjugation of ClInPc(COOH)$_8$ to magnetic nanoparticles.

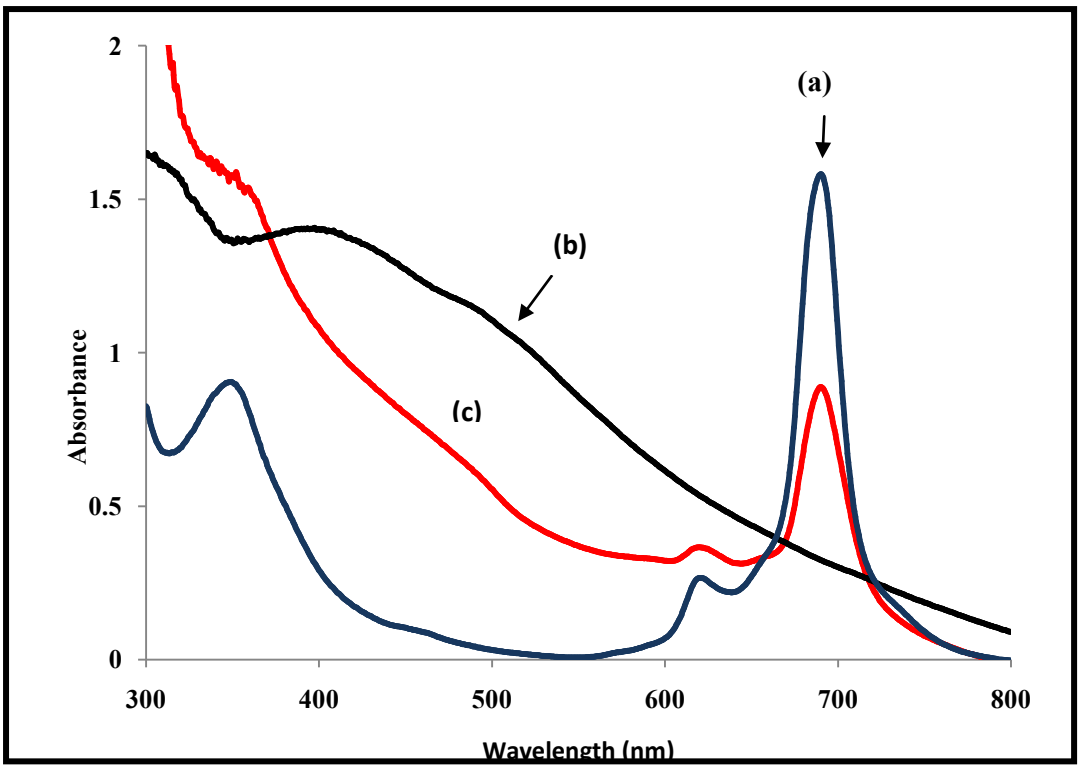

Figure 5.1: Ground state absorption spectra of (a) $ClInPc(COOH)_8$alone (b) amino functionalized Fe_3O_4 magnetic nanoparticles alone, (c) $ClInPc(COOH)_8$-amino functionalized Fe_3O_4 magnetic nanoparticles conjugate in 0.1 M NaOH.

Table 5.1: The photophysical and photochemical parameters of ClInPc(COOH)$_{8,}$ GSH-CdSe@ZnS $^{(3.5\ nm)}$ and ClInPc(COOH)$_8$-silica coated QDs-MNPs.

Complex	$\lambda_{abs(Pc)}$	$^{a}\Phi_{F(Pc)}$	$^{b}\Phi_{F(QDs)}$	$^{a}\Phi_{T(Pc)}$	$^{a}\tau_{F(Pc)}$ (± 0.01) (ns)	$^{c}\tau_{F(QDs)}$ (av) (ns)	$^{a}\tau_{T(Pc)}$ (µs)
ClInPc(COOH)$_8$ or QDs alone	691	0.13	0.47	0.49	3.4	8.1	67
ClInPc(COOH)$_8$-QDs-MNPs	693	0.06	0.33	0.66	3.6	8.9	139
ClInPc(COOH)$_8$-MNPs	691	0.10	-	0.61	3.7	-	146
ClInPc(COOH)$_8$-QDs	693	0.09	0.25	0.56	3.3	9.2	168

[a] Excitation at 665 nm and values are for excitation of the Pc.
[b] Excitation at 480 nm for the QDs and conjugates ($\Phi_{F(QDs)}$) and ($\Phi_{F(conjugates)}$) respectively.

5.1.2 FT-IR

FT-IR was employed to further characterize the complexes and to also confirm the formation of the amide bond. Characteristic peaks of primary amino group (-NH_2) are observed at 1559 cm^{-1} and 1482 cm^{-1} for the amino functionalized Fe_3O_4 magnetic nanoparticles, in **Figure 5.2 (i).** The peak at 1034 cm^{-1} is assigned to Si-O-Si and Fe-O-Si bonding stretch [134], **Figure 5.2 (i**). Upon conjugating MNPs to the Pc in **Figure 5.2 (ii**) there is an emergence of a broad –NH- stretch at 3283 cm^{-1} and the peak that is assigned to the amide group (-NHCO-) at 1631 cm^{-1}. This confirms successful covalent linkage of the amino functionalized Fe_3O_4 magnetic nanoparticles to the $ClInPc(COOH)_8$.

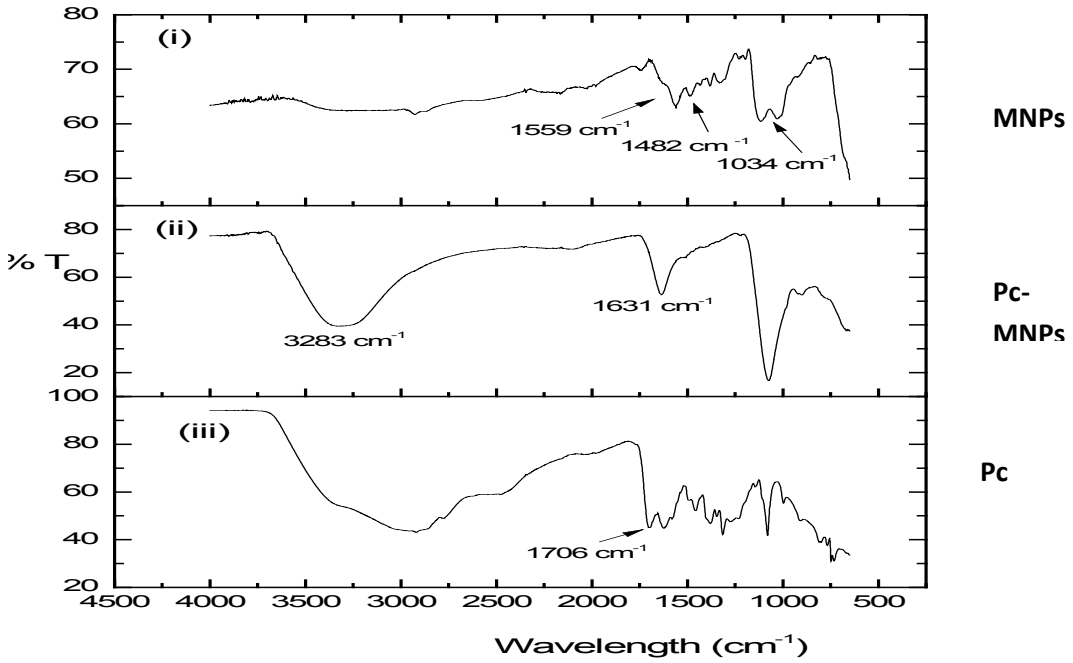

Figure 5.2: FT-IR spectra of (i) Amino functionalized Fe_3O_4 magnetic nanoparticles, (ii) $ClInPc(COOH)_8$-Amino functionalized Fe_3O_4 magnetic nanoparticles conjugate (iii) $ClInPc(COOH)_8$.

5.1.3 Microscopic data

TEM was used to study the morphology of MNPs before and after conjugation to ClInPc(COOH)$_8$. **Figure 5.3 (a)** show images of MNPs alone, the MNPs size was determined as 19 nm, spherical in nature. Upon conjugation to form ClInPc(COOH)$_8$–MNPs in **Figure 5.3 (b)** the size of the conjugate increased and became aggregated making it impossible to measure individual particle sizes.

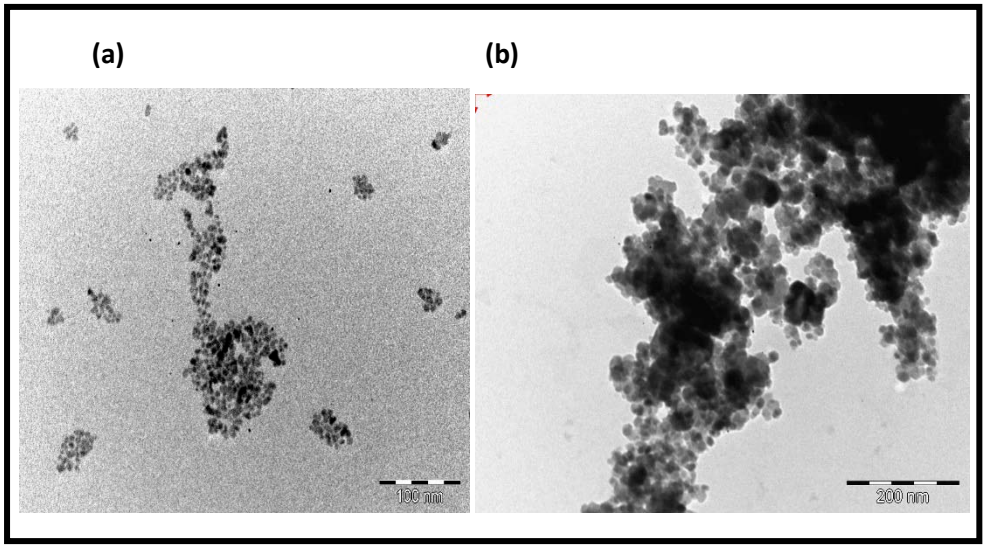

Figure 5.3: TEM images of (a) amino functionalized Fe_3O_4 magnetic nanoparticles alone (b) ClInPc(COOH)$_8$-amino functionalized Fe_3O_4 magnetic nanoparticles conjugate.

5.1.4 Thermogravimetric analysis (TGA)

Figure 5.4 shows TGA thermograms for ClInPc(COOH)$_8$ before and after conjugation with MNPs. **Curve (ii)** shows the Pc alone. As stated in section 4.1.3.3 the Pc decomposes but is still fairly stable.

Conjugating MNPs to the Pc **(curve (i))** improved the stability, with the weight loss being 0.6 % for the Pc-MNPs conjugate. This suggests that the conjugate would be ideal in hyperthermia applications.

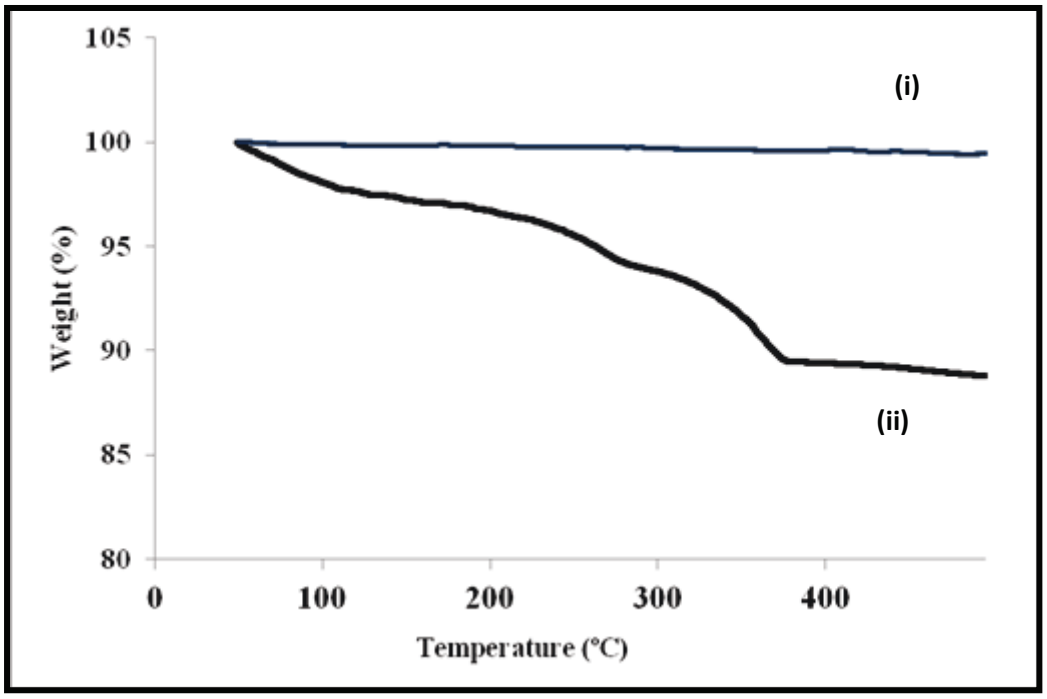

Figure 5.4: TGA curves of the (i) CdSe@ZnS-ClInPc(COOH)$_8$ conjugate and (ii) ClInPc(COOH)$_8$ alone.

5.1.5 Photophysical behavior

5.1.5.1 Fluorescence quantum yield and lifetimes

A single lifetime was obtained for both the ClInPc(COOH)$_8$ and the ClInPc(COOH)$_8$–MNPs conjugate. When linking MNPs to ClInPc(COOH)$_8$ the fluorescence quantum yields of ClInPc(COOH)$_8$ decreased from 0.13 (for Pc alone) to 0.09 (Pc-QDs conjugate) and 0.10 (for Pc-MNPs conjugate) as seen in **(Table 5.1)**. The decrease is as a result of the heavy atom effect of the nanoparticles. The paramagnetic nature of MNPs will also reduce the fluorescence quantum yields [164]. Comparing QDs with MNPs conjugates, shows only small differences in the Φ_F values, hence suggesting that the nature of the nanoparticle does not play a significant role.

5.1.5.2 Triplet Quantum yields (Φ_T) and lifetimes (τ_T)

The increased $\Phi_{T(Pc)}$ value corresponds to lower value of ($\Phi_{F(Pc)}$) of the ClInPc(COOH)$_8$-MNPs conjugate. An increase in $\Phi_{T(pc)}$ (**Table 5.1)** in the presence of MNPs is attributed to the heavy atom effects of the MNPs as was the case with QDs in Chapter 4. The increase in the Φ_T values was larger for ClInPc(COOH)$_8$-MNPs compared to ClInPc(COOH)$_8$–QDs, this could be related to the size of MNPs (19 nm) relative to QDs size (3.0 nm), even though the latter has heavier atoms. The defects on the nanoparticles will also affect their properties.

The increase in Φ_T is advantageous as it means the combining QDs and MNPs with phthalocyanines will increase the triplet state population of the phthalocyanine, therefore resulting in higher photosensitizing ability [169]. Triplet lifetimes increased for $ClInPc(COOH)_8$ in the presence of QDs or MNPs. It was previously reported in literature that conjugating MNPs to ZnPc increased the triplet lifetime [99].

Increase in the triplet yields and lifetimes for Pcs in the presence of QDs [76,77] and other nanoparticles [170] has been documented before. The increase in the triplet lifetimes could be attributed to the protection of the Pcs by the nanoparticles, as stated in section 4.2.2. The longer triplet lifetime for $ClInPc(COOH)_8$–QDs corresponds to the smaller Φ_T value.

5.1.5.3 General conclusions

Conjugates of Fe_3O_4 magnetic nanoparticles (MNPs) with indium octacarboxy phthalocyanine ($ClInPc(COOH)_8$) showed a decrease in the fluorescence lifetimes of $InPc(COOH)_8$ due to MNPs. The triplet quantum yields increased from $\Phi_T = 0.49$ for $InPc(COOH)_8$ alone to $\Phi_T = 0.61$ for Pc-MNPs. The lifetimes also became longer for the conjugates compared to Pc alone. Both conjugates were extremely thermally stable. The fact both the triplet yields and lifetimes increase suggest that these conjugates are suitable candidates for PDT and as bi-functional anticancer agents for cancer treatment and thermal stability will also be suitable in hyperthermia applications.

5.2 Investigating photophysical properties of multi-functional quantum dots-magnetic nanoparticles–indium octacarboxyphthalocyanine nanocomposite

This part of the work presents the development of a possible multifunctional hybrid nanoparticle made of $_{L}$-glutathione capped quantum dots (GSH-CdSe@ZnS$^{(3.5nm)}$), amino functionalized Fe_3O_4 magnetic nanoparticles and indium octacarboxyphthalocyanine ($ClInPc(COOH)_8$). We investigate the photophysical properties of the individual components and the hybrid nanoparticle, in addition we study the energy transfer (Förster Resonance Energy Transfer (FRET)) in the complex. GSH-CdSe@ZnS QDs of size 3.5 nm was employed.

Scheme 5.2 shows the schematic representation of the covalent linkage of the ($ClInPc(COOH)_8$ (Pc) to the silica coated QDs-MNPs. The QDs were first conjugated to MNPs as described in section 2.3.5**,** the resulting complex was coated with silica as described in literature [145], by simultaneous sol-gel polymerization of tetraethoxysilane (TEOS). $ClInPc(COOH)_8$ was attached on the surface of the silica coated-QDs-MNPs conjugate by taking advantage of the $–NH_2$ groups and using them as points of attachment. The multifunctional nanocomposite is represented as $ClInPc(COOH)_8$-QDs-MNPs.

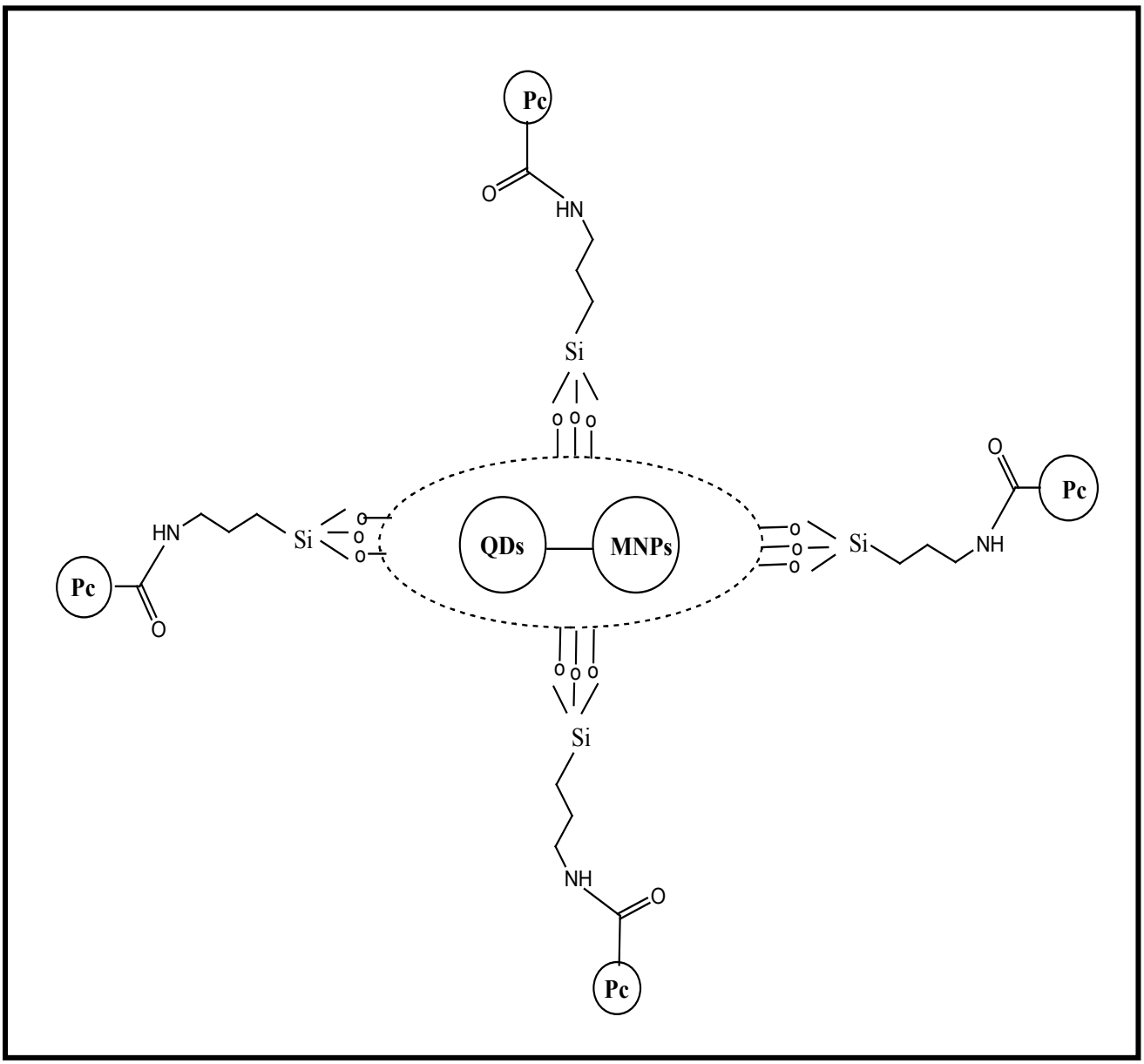
Pc
O
HN
Si
O O O
HN
Si
O
O
O
Pc
O
QDs
MNPs
O
O
O
Si
NH
Pc
Pc
O
Si
O O O
NH
O
Pc

Scheme 5.2: Schematic representation of the covalent linkage of the ($ClInPc(COOH)_8$ (Pc) to the silica coated QDs-MNPs.

5.2.1 Characterization of the nanocomposites

5.2.1.1 UV-Vis spectra

Figure 5.5 shows the UV-Vis spectra of the (a) amino functionalized Fe_3O_4 magnetic nanoparticles, (b) GSH-CdSe@ZnS QDs and (c) the silica coated QDs-MNPs conjugate. The amino functionalized Fe_3O_4 magnetic nanoparticles show a broad absorption at ~385 nm which is typical of magnetic nanoparticles. Upon conjugating the two (QDs and MNPs) an enhanced absorption is noted in the regions where the two absorb.

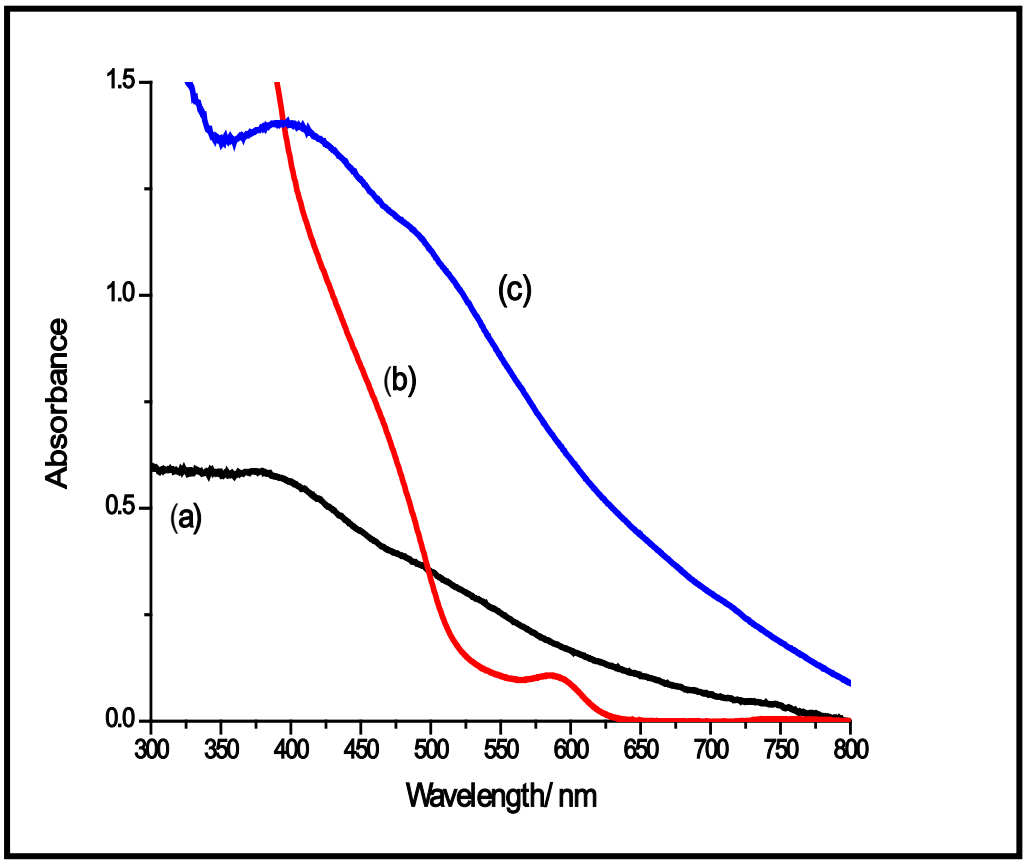

Figure 5.5: Ground state absorption spectra of (a) amino functionalized Fe_3O_4 magnetic nanoparticles (MNPs) (b) GSH-CdSe@ZnS (QDs) and (c) silica coated QDs-MNPs complex

Figure 5.6 compares the ground state absorption spectra of $ClInPc(COOH)_8$ and $ClInPc(COOH)_8$-QDs-MNPs. Upon conjugation there is slight shift in the Q-band maxima, a 3 nm shift from 691 nm (Pc alone) to 693 nm (conjugate), **Table 5.1** there is also an enhanced absorption below 600 nm region due to the absorption of QDs and MNPs. This indicates successful linkage of the $ClInPc(COOH)_8$ to the silica coated QDs-MNPs complex. There were also no significant Q band shifts for $ClInPc(COOH)_8$ in the presence of QDs or MNPs alone, **Table 5.1.**

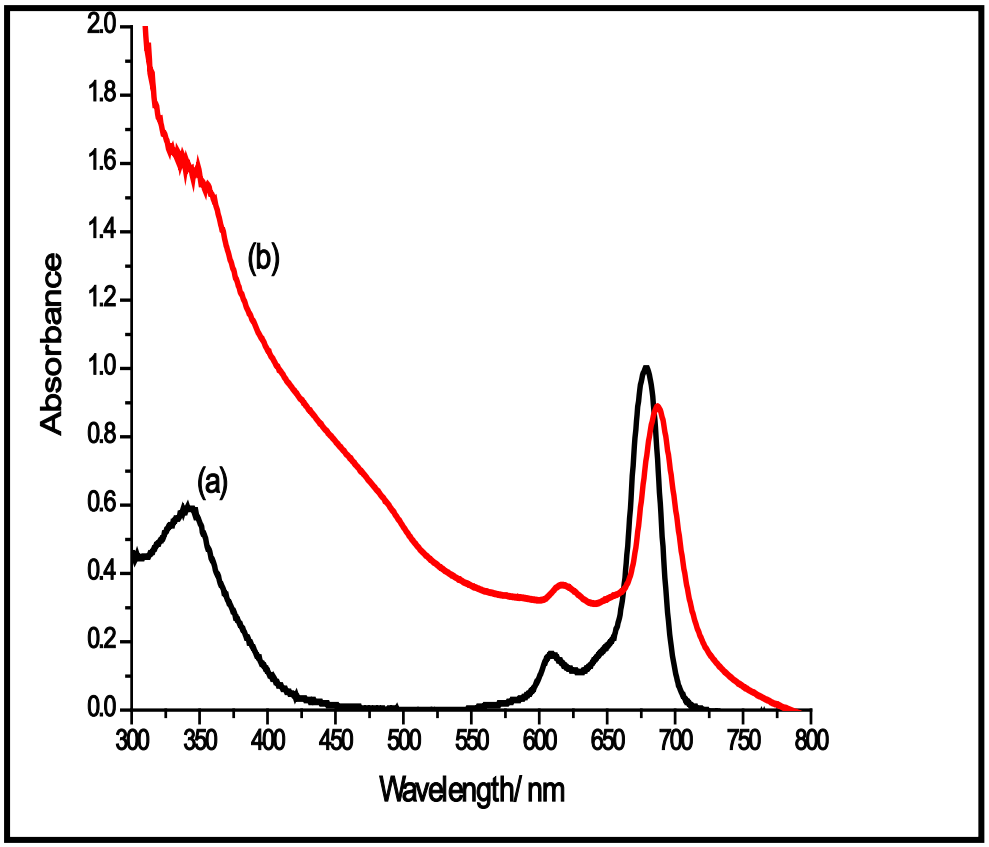

Figure 5.6: Ground state absorption spectra of (a) ClInPc$(COOH)_8$ and (b) ClInPc$(COOH)_8$ -silica coated QDs-MNPs complex

5.2.1.2 TEM images

Using TEM, the size of MNPs was determined as 22 nm and they were spherical in nature as seen in **Figure 5.7.** TEM images of QDs-MNPs the particles showed aggregation making the determination of the individual particle size impossible, **Figure 5.7c**. The aggregation of the ClInPc$(COOH)_8$-QDs-MNPs conjugate is seen in **Figure 5.7d**, hence we were unable to determine individual particle sizes using TEM. Using XRD the sizes of the QDs-MNPs-Pc

conjugate was determined to be 82 nm which is not very different from what has been observed in literature for silica coated Fe_3O_4−QDs conjugates reported to be ~100 nm[171].

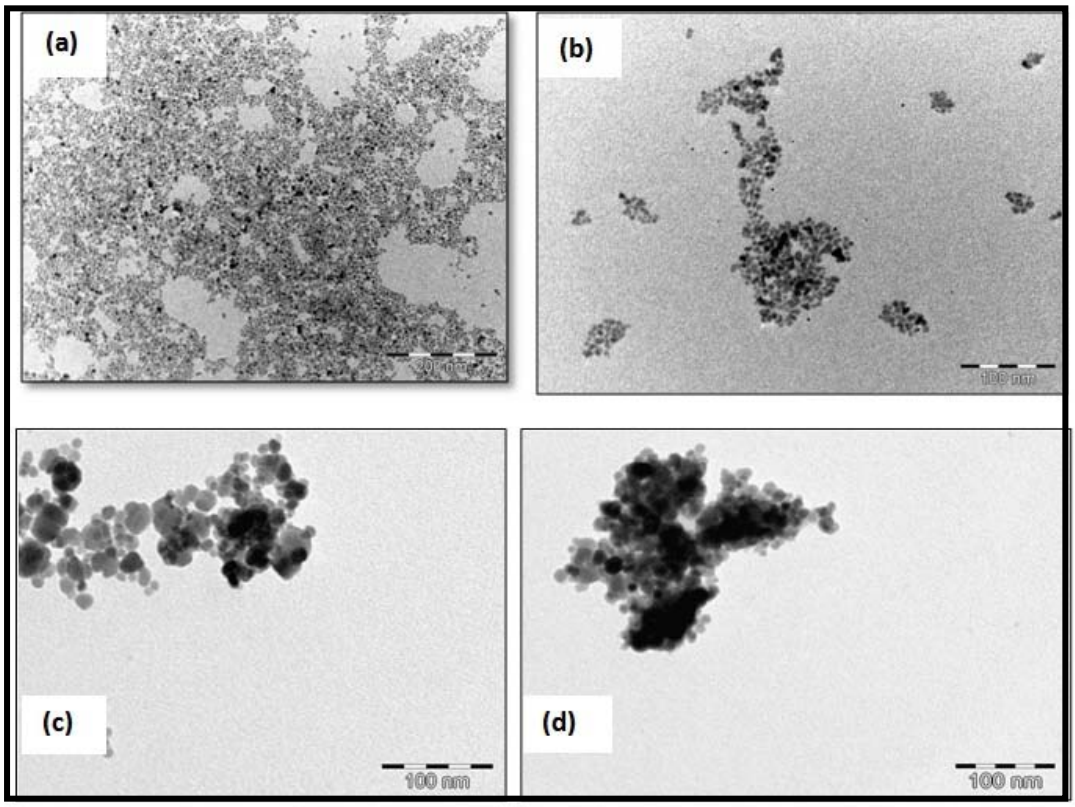

Figure 5.7: TEM images of (a) GSH-CdSe@ZnS (QDs), (b) amino functionalized Fe_3O_4 magnetic nanoparticles (MNPs), (c) silica coated QDs-MNPs conjugate and (d) $ClInPc(COOH)_8$-QDs-MNPs conjugate.

5.2.1.3 FTIR Spectra

In **Figure 5.8 A** (a) for the QDs we observe a COO- stretching band at 1591 cm^{-1} and the corresponding –OH band is found around the 3400 cm^{-1} region. Characteristic peaks of primary amino group ($-NH_2$) are observed at 1559 cm^{-1} and 1550 cm^{-1} for the amino functionalized Fe_3O_4 magnetic nanoparticles, in **Figure 5.8 A (b)**. The peak at 1034 cm^{-1} is assigned to Si-O-Si and Fe-O-Si bonding stretch [134]. Successful chemical linkage of MNPs

to QDs is confirmed by **in Figure 5.8 A (c),** as is judged by the formation of bands corresponding to primary and secondary amide at 1738 cm^{-1} and 1481 cm^{-1}, the encapsulation with the silica was confirmed by the band at 1135 cm^{-1} which is attributed to the Si-O peak. In **Figure 5.8 B** we compare the FT-IR of; (a) $ClInPc(COOH)_8$, (b) silica coated QD-MNPs conjugate and (c) $ClInPc(COOH)_8$-silica coated QDs-MNPs conjugate. In **Figure 5.8 B (a)** for $ClInPc(COOH)_8$ the C=O vibration of the $ClInPc(COOH)_8$ is observed at 1664 cm^{-1}, a broad peak near 3250 cm^{-1} corresponds to O-H of the carboxyl groups. The latter broadens upon conjugation with the silica coated QDs-MNPs complex, **(Figure 5.8 B(c))**. A peak at 1653 cm^{-1} corresponds to the amide bond and confirms the success of the conjugation. The peaks at 971 and 1091 cm^{-1} are attributed to the presence of silica **(Figure 5.8 B(c)).**

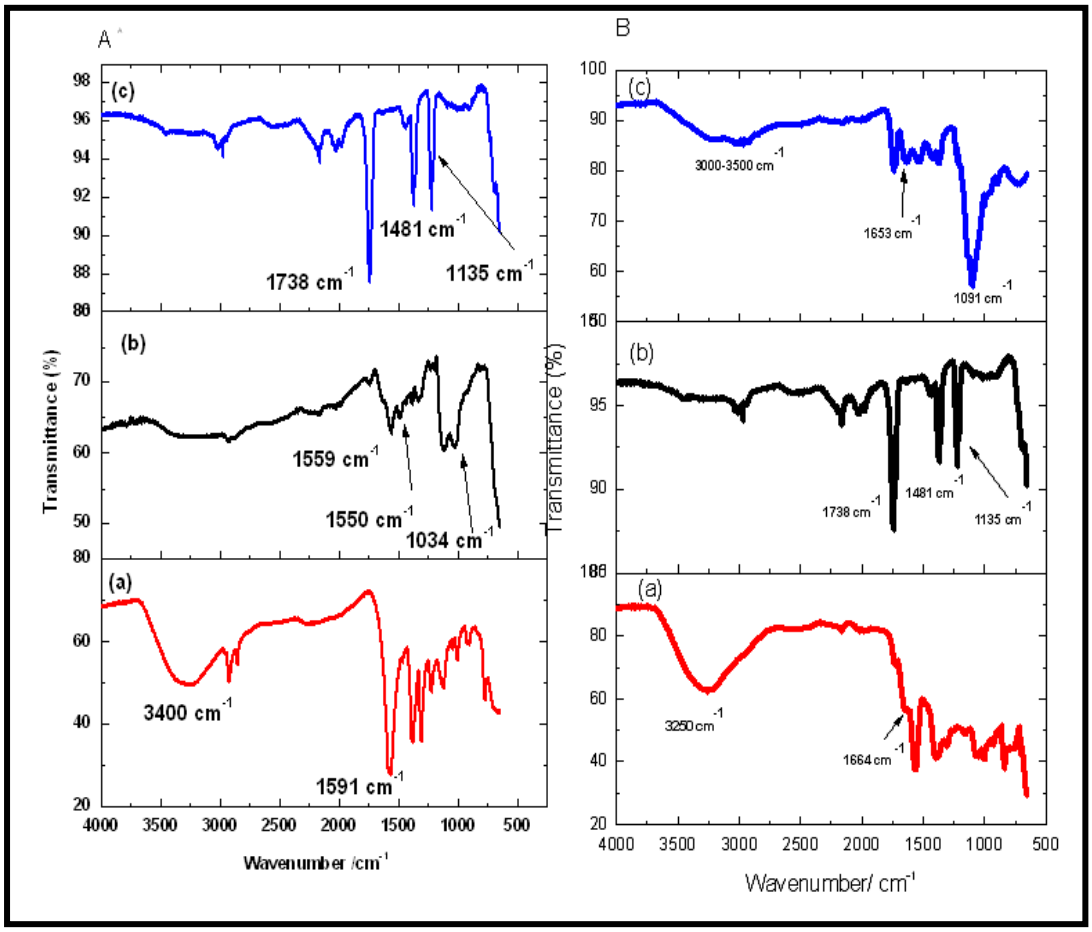

Figure 5.8: FT-IR spectra of: (A) (a) GSH-CdSe@ZnS QDs, (b) Amino functionalized Fe_3O_4 magnetic nanoparticles (MNPs) and (c) silica coated QDs-MNPs, (B) (a) $ClInPc(COOH)_8$, (b) silica coated QDs-MNPs and (c) $ClInPc(COOH)_8$silica coated QDs-MNPs.

5.2.2 Photophysical parameters

5.2.2.1 Fluorescence quantum yields

When linking the silica coated QDs-MNPs complex to ClInPc(COOH)$_8$ we observed a decrease in the fluorescence quantum yield ($\Phi_{F(Pc)}$)of ClInPc(COOH)$_8$ (when exciting where Pc absorbs and there is minimal absorption by the QDs). The fluorescence quantum yield decreased from 0.13 (for Pc alone) to 0.06 (ClInPc(COOH)$_8$-QDs-MNPs conjugate) (**Table 5.1**). The decrease is as a result of the heavy atom effect of the nanoparticles (QDs and MNPs). The paramagnetic nature of MNPs has also been reported to reduce the fluorescence quantum yields. There is also a decrease in fluorescence ($\Phi_{F(Pc)}$) for ClInPc(COOH)$_8$ when linked individually to MNPs or QDs, **Table 5.1,** as discussed already**.**We also excited where QDs absorb and Pcs do not. We observed a decrease in the fluorescence quantum yield of QDs in the conjugate (ClInPc(COOH)$_8$-QDs-MNPs), from $\Phi_{F(QDs)}$= 0.47 for QDs alone to $\Phi_{F(conjugate\ )}$ = 0.33 for the conjugate (**Table 5.1**). FRET and other processes which deactivate the excited states of the QDs have been reported to decrease the fluorescence quantum yield [162]. Interestingly when QDs alone are linked to ClInPc(COOH)$_8$, without MNPs, there is a larger quenching of their fluorescence, **Table 5.1**, suggesting that the presence of MNPs reduces the surface defects of QDs which result in reduced fluorescence.

5.2.2.2 Triplet Quantum yields (Φ_T) and lifetimes (τ_T)

The Φ_T of the ClInPc(COOH)$_8$-QDs-MNPs conjugate (Φ_T =0.66) was higher than for ClInPc(COOH)$_8$ alone at Φ_T = 0.49, **Table 5.1**. An increase in Φ_T in the presence of QDs and MNPs is attributed to the combined heavy atom effect of the MNPs and QDs, thus encouraging ISC. The increase in Φ_T suggests that 3-in one complex (ClInPc(COOH)$_8$-QDs-

MNPs) will increase the triplet state population of the phthalocyanine, therefore resulting in enhanced photosensitizing ability. The triplet state quantum yields and lifetimes for $ClInPc(COOH)_8$ increased in all cases in the presence of MNPs, QDs or QDs-MNPs. The largest increase in triplet lifetimes is observed for conjugate of QDs alone, **Table 5.1**. The increase triplet lifetimes suggest that the MNPs, QDs or QDs-MNPs protect the $ClInPc(COOH)_8$ against the environment.

5.2.3 Förster Resonance energy Transfer (FRET) studies

We also investigated energy transfer between the silica coated QDs-MNPs conjugate and the Pc, (**Figure 5.9**)

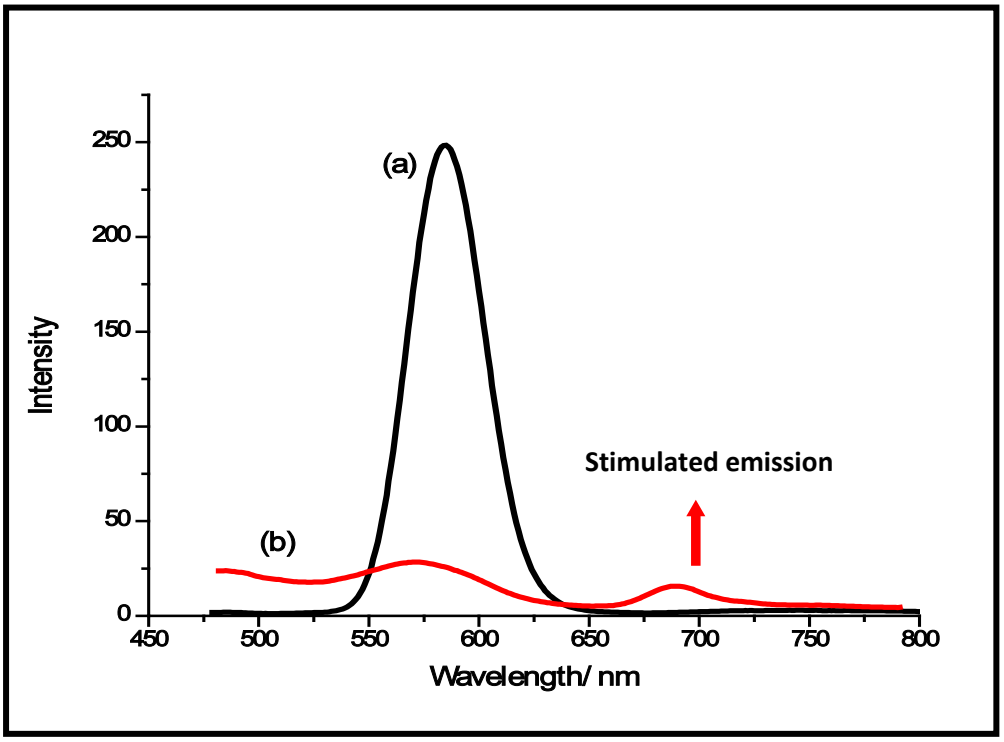

Figure 5.9: Fluorescence emission spectra of (a) GSH-CdSe@ZnS QDs alone (b) ClInPc(COOH)$_8$-QDs-MNPs conjugate.

FRET occurrence is made evident by the decrease in the photoemission of the donor accompanied by an increase in the acceptors fluorescence. For the ClInPc(COOH)$_8$-QDs-MNPs conjugate, excitation was carried at 520 nm where QDs absorb but the phthalocyanine does not absorb. A stimulated emission peak was observed where the Pc emits at around 698 nm, which suggests a transfer of energy from the QDs to ClInPc(COOH)$_8$ **(Figure 5.9)**.

As stated above, there are other processes which deactivate the excited states of the QDs in addition to FRET, hence a weak stimulated emission peak is observed in **Figure 5.9**, and the calculated FRET efficiencies (*Eff*) are estimates. The *Eff* values was found to be 0.79 for

ClInPc(COOH)$_8$-QDs-MNPs corresponding to R_0 (63.3Å) being greater that r (47.8Å). For ClInPc(COOH)$_8$-QDs alone, the *Eff* values was found to be 0.79 corresponding to R_0 (45.4Å) being greater than r (41.0Å). The J values obtained in this work were 6.56 x 10^{-14} cm^6 for both the ClInPc(COOH)$_8$-QDs alone and for ClInPc(COOH)$_8$-QDs-MNPs. Thus the value is not different from when QDs alone without MNPs.

5.4.3 General conclusions

The multi-functional nanocomposite showed improved photophysical properties and we were able to demonstrate a transfer of energy in the complex. FRET efficiencies of ~ 79 % were obtained for energy transfer between the QDs (when alone or linked to MNPs and Pc). Both quantum triplet yields and lifetimes of ClInPc(COOH)$_8$ increase in the nanocomposite, with a decrease in fluorescence lifetime. These improved photophysical parameters makes this 3-in-one complex a suitable candidate as a multifunctional drug in PDT applications.

CHAPTER 6

Thesis Conclusion

6.1 Thesis Conclusions

Of the seven different types of quantum dots without shell (L-cysteine-CdTe, TGA-CdTe, MPA-CdTe, TGA-CdSe) and with the shell (GSH-CdSe@ZnS, GSH-CdTe@ZnS) screened, GSH-CdSe@ZnS was determined as the least toxic of the batch. The GSH-CdSe@ZnS QDs displayed the lowest growth inhibitory potential and no embryotoxicity. GSH-CdSe@ZnS QDs were chemically coordinated to $ClAlPc(COOH)_8$, $ClGaPc(COOH)_8$ and $ClInPc(COOH)_8$. Characterization techniques, including UV/Vis, FT-IR, XRD and TEM confirmed successful coordination of the various Pcs to the QDs, while TGA showed improved thermal stability of the conjugates. The conjugates showed improved photophysical properties. Amino functionalized magnetic nanoparticles (Fe_3O_4) were also conjugated to indium octacarboxy phthalocyanine. The conjugate enhanced the photophysical behaviour and as a result could be used as a potential bi-functional anti-cancer agent (hyperthermia and photodynamic therapy applications). The three-in-one multifunctional nanocomposite developed showed great photophysical behaviour. Finally the application of GSH-CdSe@ZnS- $ClAlPc(COOH)_8$ showed a dosage dependant cell death.

6.2 Future work

To test the effectiveness of the newly synthesized multifunctional nanocomposite *in vivo* and *in vitro*. Synthesize a new batch of quantum dots employing two shells that will protect the core from leaching and employ different capping agents such as L-cystiene and evaluate the toxicity of the new QDs. Further conjugate the new QDs to Pcs with various central metals and apply the conjugates in Photodynamic therapy applications.

References

References

1. G. Gali, A. Pudzer, A. J. Willamson, J. C Grossman and L. Pizzagali, *Nanotech.***1** (2002) 470.
2. E. Bailey and S. M. Nie, *J. Am. Chem. Soc*. **125** (2003) 7100.
3. A. L. Efros, *Sov. Phys. Semicond.* **16** (1982) 772.
4. A. I. Ekimov and A. A. Onushchenko, *Sov. Phys. Semicond.* **16** (1982) 775.
5. A. P. Alivisatos, *J. Phys. Chem.***100** (1996) 13226.
6. M. Zhou and I. Ghosh, *Biopolymers.***88** (2007)325.
7. H. Arya, Z. Kaul, R. Wadwha, K. Taira, T. Hirano and S.C. Kaul,*BiochemBiophys Res Commun.* **329** (2005) 1173.
8. P. Alivisatos, *Nature Biotechnology.* **22** (2004) 47.
9. W. Schroter, In Handbook of semiconductor technology, Electronic structure and properties of semiconductors, Wiley VCH, Weinheim, (2000).
10. P. Alivisatos, *Science*.**271** (1996) 933.
11. M. Bruchez Jr, M. Moronne, P. Gin, S. Weiss and A. P. Alivisatos, *Science*. **281** (1998) 2013.
12. http://www.concepts.aero/system/files/quantumdots .jpg
13. J. R. Lakowiecz. Principles of fluorescence spectroscopy, 2nd edition, Kluwer Academic/Plenum Publishers, New York (1999).
14. S. Dayal, A. Lou and J. Samia, *Appl. Phys. B*. **84** (2006) 309.
15. S. Moenoand T. Nyokong, *Polyhedron.* **27** (2008) 1953.
16. S. Moenoand T. Nyokong, *J. Photochem. Photobiol. A: Chem*. **201** (2009) 228.
17. A. O. Orlova, V. G. Maslov, A.V. Baranov, I. Gounko and S. Byrne, *Optics and Spectroscopy*. **105** (2008) 726.

18. P. Juzenas. W. Chen, Y-P. Sun, M .A. N. Coelho, R. Generalov, N. Generalov and I. L Christensen, *Adv. Drug Deliv. Rev*. **60** (2008) 1600.

19. C.B. Murray, D.J. Norris, M.G. Bawendi, *J. Am. Chem. Soc.* **115**(1993) 8706.

20. M. Green and E. Howman, *ChemCommun (Camb)*. **3** (2005) 121.

21. A. M. Iga, J. H. P. Robertson, M. C. Winslet and A. M. Seifalian, *J. Biomed Biotechnol*. **20** (2007) 76087.

22. T. Jamieson, R. Bakhshi, D. Petrova, R. Pocock, M. Imani and A. M Seifalian, *Biomaterials.***28** (2007) 4717.

23. A. G. Kidane, G. Burriesci, M. Edirisinghe, H. Ghanbari, P. Bonhoeffer and A. M. Seifalian, *ActaBiomater.***22** (2009) 2409.

24. S. Ceo, W. K. Woo, M. Bawendi and V. Bulovic, *Nature.* **420** (2002) 800.

25. A. P. Alivisatos, W. Gu and C. Larabell, *Annu Rev Biomed Eng*.**7** (2005) 55.

26. C. Kirchner, T. Liedl, S. Kudera, T. Pellegrina, A. Munoz, H. E. Gaub, S. Stolzle, N. Fertig and W. J Parak, *NanoLett*. **5** (2005) 331.

27. J. Lovric, H. S. Bazzi, Y. Cuie, G. R. Fortin, F. M. Winnik and D. Maysinger, *J. Mol. Med (Berl).* **83** (2005) 377.

28. A. H. A. Shiohara, K. Hanaki, K. Suzuki and K. Yamamoto, *Microbiol. Immunol.* **48** (2004)669.

29. R. Hardman, *Environ Health Perspect.* **114** (2006)165.

30. W. H. Chan, N. H. Shiao and P. Lu, *Toxicol let.* **167** (2006) 191.

31. J. K. Jaiswal, H. Mattoussi, J. M. Mauro and S. M. Simon, *Nat Biotechnol.* **21** (2003)47.

32. F. Q. Chen,*NanoLett.* **4** (2004)1827.

33. A. F. K. Hoshina, T. Oku, M. Suga, Y. F. Sakaki and M. Yasuhara, *NanoLett*. **4** (2004) 63.

34. T. S. J. Zhang, D. Geroin, L. Ding, P. A Cooke, J. W Gray, A. P Alivisatos and F. F Chen, *Nano Lett*.**6** (2006) 800.

35. J. B. Delehanty, H. MautoussiI and L Medintz, *Anal. Bioanal. Chem*.**393** (2009) 1091.

36. S. J. Cho, M. Jain, B. Roder, S. Hackbarth and F. M. Winnik, *Langmuir*.**23** (2007) 1974.

37. M. X. T. Tang, J. Zeng, H. Wang, C. Li, S. Yin, D. Yan, H. Deng, J. Chen, D and Y. Ruan, *Environ. Health. Perspect.* **116** (2008) 915.

38. L. N. D. Wang, L. Selvarasah, M. R. Dokmeci and R. I. Carrier, *J. Nanobiotechnology*. **6** (2008) 11.

39. J. Lovric, S. J. Cho, F. M. Winnik and D. Maysinger, *Chem. Biol.**12*** (2005) 1227.

40. Y. Su, H. Lu, L. Sai, Q. Li, L. Wang, P. Shen, P. Huang and C. Fan, *Biomaterials*. **30** (2009)19.

41. J. P. Zimmer, S. W. Kim, S. Ohnishi, E. Tanaka, J. V. Frangioni and M. G. Bawendi, *J. Am. Chem. Soc*.**128** (2006) 2526.

42. H. C. Fischer, K. S. Pang and W. C. Chan, *Adv. Funct. Mater*.**16** (2006) 1299.

43. M. L. Schipper, Z. Cheng, S. W Lee, L. A Bentolia, G. Iyer, J. Rao, X. Chen and S. Weiss, *J. Nucl. Med*.**48** (2009) 1511.

44. J. D. Woodward, S. Dai, J. S. Wall, T. Richey and J. A. Avenall. *Nanotechnology.***18** (2007) 175103.

45. R. K. Gilchrist, R. Medal, W. D. Shorey, R. C. Hanselman and J. C. Parrot, *Ann. Surg*. **146** (1957) 596.

46. A. R. Simioni, M. M. A. Rodrigues, F. L. Primo, P. C. Morais and A. C. Tedesco, *J. Nanosci. Nanotechnol*. **11** (2011) 360.

47. R. Kubin and A. Fletcher, *J. Lumin*. **27** (1982) 455.

48. L. Qi and X. Gao, *Expert Opin. Drug. Deliv*. **5** (2008) 263.

49. Y. Wang and L. Chen, *Nanomedicine.***7** (2011) 385.

50. R. D Tilley, *J. Chem.***5** (2008) 146.

51. D. Bera, L. Qian, T. K Tseng and P. Holloway, *Material*s. **3** (2010) 2265.

52. S. Zhu, J. Zhang, C. Qiao, S. Tang, Y. Li, W. Yuan, B. Li, F. Tian F. Liu, H. Sun and B. Yang, *Chem. Commum.***47** (2011) 6858.

53. G. P. C. Drummen, *Int. J. Mol. Sci.* **11** (2010) 154.

54. K. L Wang, D. Cha, J. Lui and C. Chen, Proc. IEEE **95** (2007) 1866.

55. R. S. Akhtar, S. Latham, D. Fuccio and K. A Roth, *Methods MolBiol* .**374**(2008) 11.

56. X. Gao, Y. Cui, R. M Levenson, L. W. Chung and S. Nie, Nat. *Biotechnol.* **22** (2004)969.

57. http://www.trial.com/curetalk/files/diseases/photodynamictherapy.jpg

58. R. Bonnet in: *Chemical Aspects of Photodynamic therapy,* Gordon and Breach Science Publishers, Amsterdam (2000).

59. M. Triesscheijn, P. Baas, P. Schellens and F. A. Stewart, *Oncologist.* **11** (2006) 1034.

60. I. Okura in: *Photosensitization of Porphyrins and Phthalocyanines*, Gordon and Breach publishers, Germany (2001).

61. E. A. Lukyanets, *J PorphyrPhthalocya.***3** (1999) 424.

62. A. C.Samia, X. B Chen and C. Burda, *J. Am. Chem. Soc.***7** (2003) 15736.

63. E. Yaghini, A. M. Seifallian and A. J. Marcobert, *Nanomedicine (Lond*). **4** (2006) 353.

64. J. Turro, In Modern Molecular Photochemistry. The Benjamin Cummings Publishing Co, Inc, New York (1978).

65. P. Kalab and J. Soderholm, *Methods.***51** (2010) 220.

66. D. Stepensky, *Biochem. Biophys. Res. Commum*. **359** (2007) 752.

67. P. Chawla, G. Sharm and S. P. Lochab, N. Singh, *Bull. Mater. Sci*. **33** (2010) 535.

68. E. Raquel and C. Juan, *Photochem. Photobiol. Sci*. **8** (2009) 56.

69. N. E .Triggs and J. J. Valentini, *J. Phys. Chem*. **96** (1992) 6922.

70. J. C. B. Huarac, M. S. Tomar, S. P. Singh, O. Perales-Perez, L. Rivera and S. Pena, *Nanotec*.**3** (2010) 405.

71. D. A. Tekdas, M. Durmus, H. Yanik and V. Ahsen, *Spectrochim, Acta, Part A*. **93** (2012) 313.

72. M. Idowu and T. Nyokong, *J. Lumin.* **129** (2009) 356.

73. A. Erdogmus, S. Moeno, C. Liwinski and T. Nyokong, *J. Photochem. Photobiol. A*. **210** (2010) 200.

74. J. Ma, J. Y Chen, M. Idowu and T.Nyokong, *J. Phys. Chem. B*. **112** (2008) 4465.

75. J. Britton, E. Antunes and T. Nyokong ,*J. Photochem. Photobiol. A. Chem*. **210** (2010) 1.

76. K. E. Sekhosana, E. Antunes, S. Khene, S. D'Souza and T. Nyokong, *J. Lumin.***136** (2013) 255.

77. S. D'Souza, E. Antunes, C. Liwinski and T. Nyokong, *J. Photochem. Photobiol. A*: **220** (2011) 11.

78. S. Moeno, E. Antunes, S. Khene, C. Liwintski and T. Nyokong, *Dalton Trans*. **39** (2010) 3460.

79. S. D'Souza, E. Antunes and T. Nyokong, *Inorg. Chim. Acta*. **367** (2011) 173.

80. W. Chidawanyika, C. Litwinski, E. Antunes and T. Nyokong. *J. Photochem. Photobiol A. Chem*. **212** (2012) 56.

81. S. Khene and T. Nyokong, *Microchem. Journal.***99** (2011) 478.

82. N. Masilela and T. Nyokong, *J. Photochem. Photobiol. A: Chem*. **247** (2012) 82.

83. O. Adegoke and T. Nyokong, *Synthetic Met.***188** (2014) 35.

84. O. Adegoke and T. Nyokong, *J. Lumin.* **134** (2014) 446.

85. C. R. Vestal, Z. J. Zhang, *Int. J. Nanotech.***1** (2004) 240.

86. G. H. Kwei, R. B. von Dreele, A. Williams, J. A Goldstone, A. C. Lawson and W. K Warburton, *J Mol. Struct.* **223** (1990) 383.

87. Y. Chen and B-A. Chen, *Chinese J. Cancer.* **29** (1) (2012) 118.

88. X. Peng, H. Chen, J. Huang, H. Mao and D. M. Shin. Biomedical Engineering-From Theory to Applications. **9** (2010).

89. L. E Sousa-Herves, R. Rigger, Fernandez and E. Megia, *Nanosystems. Pharm Res.***29** (2012) 1.

90. D. Dobson. *Nanomedicine*. **1** (2006) 31.

91. H. Iida, K. Takanayagi, T. Nakanishi and T. Osaka, *J. of Colloid and Interface Science.* **314** (2007) 274.

92. A. K Gupta and M. Gupta, *Biomaterials.***26** (2005) 3995.

93. C. Alexiou and R. Jurgons in: *Magnetism in Medicine,* Ed. W. Andra, H. Nowak, Wiley-VCH, Weinheim, (2007).

94. D. K. Chatterjee, L. S. Fong and Y. Zhang, *Advanced Drug Delivery Reviews.* **60** (2008) 1627.

95. G. Baldi, G. Lorenzi and C. Ravagli, *Processing and Application of Ceramics*.**3** (2009) 103.

96. B. Thiesen, A. Jordan, *Int. J. Hyperthemia.***24** (2008) 467.

97. N. K. Prasad, K. Rathinasamy, D. Panda and D. Bahadur, *J. Mat. Chem.***17** (2007) 5013.

98. W. Lu, Y. Shen, A. Xie and W. Zhang, *J. Magn.Magn. Mat.* **322** (2010) 1828.

99. P. Modisha, E. Antunes, J. Mack and T. Nyokong, *Int. J. NanoSci.***12** (2013) 1350010.

100. K. Ozawa, K. Ishii, Phys. *Chem.Chem. Phys*.**11** (2009) 1019.

101. A. Rezaifard, M. Jafarpour, A. Naeimi, *Green Chem*.**14** (2012) 3386.

102. E. Van Lier and J. D. Spikest, Photosensitising compounds: their Chemistry, biology and clinical use, Wiley and Sons Ltd. (1989).

103. C. Jain, *Res. J.Chem.Sci.***1** (2011) 1.

104. L. R. Milgrom, The colours of Life, an introduction to the chemistry of porphyrins and related compounds, Oxford University Press Inc., New York, (1997).

105. H. S.Nawla and J. S Shirk in *Phthalocyanines: Properties and Applications*, eds. C. C. Leznoff and A. B. P Lever, vo1 4 (1991).

106. M. J. Stillman and T. Nyokong, In *Phthalocyanines: Properties and Applications*, eds. C.C. Leznoff and A.B.P. Lever, VCH publishers, New York, Vol. 1133, Chp.3. (1989).

107. T. Nyokong, Z. Gasyna and M.J. Stillman, *Inorg. Chem.* **26** (1987) 548.

108. A. Gilbert and J. Baggot, *Essentials of molecular photochemistry,* library of congress USA, (1995).

109. J. Fu, X. Y. Li, D. K P, Ng and C. Wu, *Langmuir*. **18** (2002) 3843.

110. B. Simic-Glavaski in *Phthalocyanine: Properties and Applications*, eds. A.P.B. Lever and C.C. Leznoff, VCH Publishers, New York, 1993, Vol. 3

111. A.W. Snow and W.R. Barger in *Phthalocyanines: Properties and Applications* eds.A.P.B. Lever and C.C. Leznoff, VCH Publishers, New York, 1989, Vol.**1**.

112. C.J. Murphy and J. L. Coffer, *Appl. Spectros.* **56** (2002) 16

113. M. Sailor M and J. Park, *Adv. Mater*. **24** (2012) 3779.

114. J. Kim, S. Park S, J Lee, S Jin S, J. Lee, I. Lee I and I. Yang. *Angew. Chem. Int. Ed.***46** (2006) 7754.

115. J. Park, G. von Maltzahn, E. Ruoslahti, S. Bhatia and M. Sailor M. *AngewChemInt Ed.* **47** (2008) 7287.

116. X. Huang , I. H. El-Sayed , W. Qian and M. A. El-Sayed , *J. Am. Chem. Soc.***128**(2006) 2115 .

117. Y. Piao, A. Burns, J. Kim, U. Wiesner and T. Hyeon, *Adv. Funct. Mater.* **18** (2008) 3745.

118. A. Bromley, Theranostics: the influence of diagnostics on pharmaceutical therapy, P. J. B. Publications, Richmond, GB (2000).

119. R. Weissleder, A. Bogdanov, E. A. Neuwelt and M. Papisov, *Adv. Drug Deliv. Rev.* ***16 (***2006) 321.

120. J. H. Lee, Y. M. Huh, Y. Jun, J. Seo, J. Jang , H. T. Song, S. Kim, E. J. Cho, H. G. Yoon, J. S. Suh and J. Cheon, *Nat. Med.* **13**(2007) 95.

121. J. H. Park, G. v. Maltzahn, L. Zhang, M. P. Schwartz, E. Ruoslahti, S. N. Bhatia and M. J. Sailor, *Adv. Mater.***20**(2008) 1630.

122. M. E. Akerman, W. C. W. Chan, P. Laakkonen, S. N. Bhatia and E. Ruoslahti, *Proc. Natl Acad. Sci. USA*. **99**(2002) 12617.

123. X. Ding, R. Singh, A. Burke, H. Hatcher, J. Olson, R. A. Kraft, M. Schmid, D. Carroll, J. D. Bourland, S. Akman, F. M. Torti and S. V. Torti, *Nanomedicine*. **6**(2011) 1341.

124. A. A. Bhirde, V. Patel, J. Gavard, G. Zhang, A. A. Sousa, A. Masedunskas, R. D. Leapman, R. Weigert, J. S. Gutkind and J. F. Rusling , *ACS Nano*. **3**(2009) 307.

125. F. Yang , C. Jin , D. Yang , Y. Jiang , J. Li , Y. Di , J. Hu , C. Wang , Q. Ni and D. Fu, *Eur. J. Cancer*. **47**(2011) 1873.

126. C. Wang, J. Chen, T. Talavage and J. Irudayaraj, *Angew. Chem. Int. Ed.* **48**(2009) 2759.

127. A. Lowery, A. M. Goblin, E. S. Day, N. Halas and J. West.*Int. J.Nanomedicine.* Jun **1**(2006) 149

128. M. Idowu, T. Nyokong. *Int J Nanoscience.***11(**2) (2012) 1250018.

129. S. Fery-Forgues and D. Lavabre, *J. Chem. Ed*. **76** (1999) 1260.

130. A. Ongisupe and T. Nyokong. *J. Photochem. Photobiol. Sci*. **4** (2005) 510.

131. A. Gilbert and J. Baggot, Essentials of molecular photochemistry, library of congress, USA (1995).

132. C. Schweitzer and R. Schmidt, *Chem. Rev*. **103** (2003) 1685.

133. A. A. Frimer, *The Spectrum.* **13** (2000) 9.

134. H. Du, R. Fuh, J. Li, L. Corkan and J. Lindsey. *PhotochemPhotobiol*. **68** (1998) 141.

135. M. Ambroz, A. Beeby, A. McRobert, M. Simpson, M. Svensen and R. Phillips, *J Photochem. Photobiol. B. Biol.***9** (1991) 87.

136. D. D. Perrin, W. L. F. Armarego, *Purification of Laboratory Chemicals,* 2nd edn.Pergamon: Oxford, (1989).

137. M. Idowu, J-Y. Chen and T. Nyokong, *New J. Chem.* **32**(2008) 290.

138. C. Dong, H. Qian, N. Fang and J. Ren, *J. Phys. Chem. B*. **110** (2006) 11069.

139. Y. F. Liu and J. Yu,*J. Colloid. Interface Sci*. **351** (2010) 1.

140. J. Peng, S. Liu, L. Wang and Y. He, *J. Colloid. Interface. Sci.* **338** (2009) 578.

141. W. Dong, H-B. Shen, X-H. Liu, M-J. Li and L-S. Li, *Spectrochim. Acta, Part A*, **78** (2011) 537.

142. W. Y William, L. Qu, W. Guo and X. Peng, *Chem. Mater*. **15** (2003) 2854.

143. K. Sakamoto and E. Ohno, *Prog. Org. Coat.***31** (1997) 139.

144. N. Masilela and T. Nyokong, *Dyes and Pigments.* **84** (2010) 242.

145. R. Bagwe, C. Yang, L. Hilliard L and W. Tan, *Langmuir.***20** (2004) 8336.

146. B. Nitzsche, C. Gloesenkamp, M. Schrader, M. Ocker, R. Preissner, M. Lein, M. Zakrzewicz, B. Hoffmann and M. Höpfner, *Br. J. Cancer.***103** (2010) 18.

147. T. Decker and M. L. Lohmann-Matthes, J. *Immunol. Methods*. **115** (1988) 61.

148. S. Sapra and D. D. Sarma,*Pramana.***65** (2005) 565.

149. M. Peterka and I. Klepácek, *ReprodToxicol*. 1**5** (2001) 111.

150. A. M. Derfus, W.C.W. Chan and S. N. Bhatia, *NanoLett*. **4** (2004) 11.

151. Y. Su, Y. He, H. Lu, L. Sai, Q. Li, W. Li, L. Wang, P. Shen and Q. Huang, *Biomaterials*. **30** (2009) 19.

152. J. Lee, K. Ji, J. Kim, C. Park, K. H. Lim, T.H. Yoon and K. Choi, *Environ Toxicol*. **25** (2010) 593.

153. S. Ithurria, P. Guyot-Sionnest, B. Mahler and B. Dubertret, *Phys Rev Lett.* **99** (2007) 5.

154. K .T. Yong, W.C. Law, I. Roy, Z. Jing, H. Huang, M. T. Swihart and P.N. Prasad, *J Biophotonics*. **4** (2011) 9.

155. J. D. Smith, G. W. Fisher, A. S. Waggoner and P. G. Campbell, *Microvascular research*.**73** (2007) 75.

156. X. Gao, Y. Cui, R. M. Levenson, L.W.K Chung and S. Nie, *Nat Biotechnol*. **22** (2004) 969.

157. L. Li, J-F. Zhao, N. Won, H. Jin, S. Kim and J-Y. Chen, *Nano Lett*.**7** (2012) 386.

158. T. Nyokong: in *Structure and bonding*. Ed. D. M. P Mingos. Vol**135**pg 45.

159. X. Cai, Y. Zhang, X. Zhang and J. Jiang, *J. Molec. Struc. Theochem*.**801** (2006) 71.

160. S. Kilina and S. Ivanov. *J. Amer. Chem.Soc*. **131** (2009) 7717.

161. X. W. Sun, J. Chen, J. L. Song, D. W. Zhao, W. Q. Deng and W. Lei, *Optics Express.***18** (2010) 1296.

162. C. L. Takanishi, E. A. Bykova, W. Cheng and J. Zheng, *Brain Res*.**1091** (2006) 132.

163. E.I. Zenkevich, T. Blaudeck, A. Milekhin and C von Borczyskowski, *Int. J.Spectr* (2012) 1-14 ID 971791.

164. T. S. Lagoda, M. A. Kaplan, I. Krivosheev, L. P. Zhavoronkov and M. B. Bokova, *Vopr. Onkol.***46** (2000) 327

165. M. V. Budzinskaia, V.G. Likhvantseva, S. A. Shevxchik, V. B. Loshchenov, S. G. Kuz'min and G. N. Vorozhtsov, *Vestn. Oftalmol.***12** (2005) 17.

166. V.G. Likhvantseva, E. A. Osipova, M. A. Petrenko, O. I. Merzliakova, S. G. Kuz'min and G. N. Vorozhtsov, *Vestn. Oftalmol*. **124** (2008) 38.

167. O. I. Apolikhin, *Soc. Photo-Opt. Instrum*. **8** (2007) 45.

168. A. Shiohara, A. Hoshino, K. Hanaki, K. Suzuki, K. Yamamoto, *MicrobiolImmunol* **48** (2004) 669.

169. X. Wang, L. Qu, J. Zhang, X. Peng and M. Xiao, *Nano. Lett*. **3** (2003) 1103.

170. A. Fashina, E. Antunes and T. Nyokong, *New J. Chem*. **37** (2013) 2800.